Dissecting the Gravitational Lens B1608+656: Implications for the Hubble Constant

Thesis by

Sherry H. Suyu

In Partial Fulfillment of the Requirements

for the Degree of

Doctor of Philosophy

California Institute of Technology

Pasadena, California

2008

(Defended June 14, 2007)

Acknowledgements

I would like to thank my collaborators Chris Fassnacht, Leon Koopmans, John McKean, and Tommaso Treu for their help and support throughout my PhD. A special thanks to my collaborator and mentor, Phil Marshall, for always being so generous with his time and knowledge and so patient and encouraging. I feel fortunate to have seized Roger Blandford as my advisor shortly before he relocated to Stanford University. Roger has not only taught me science, but has also shown me proper scientific etiquette. The amount of care and support he gives his students, both scientifically and personally, is impressive. I thank Kip Thorne for being my official advisor at Caltech and for helping me while Roger was away.

I would like to acknowledge the Kavli Institute for Particle Astrophysics and Cosmology and the Kavli Institute for Theoretical Physics for hosting me during parts of my graduate studies. I am grateful to Maruša Bradač, Liz Blandford, and Roger Blandford for their kind hospitality when I visited Stanford. I thank the Natural Sciences and Engineering Research Council of Canada for the Postgraduate Scholarships.

Cheers to my awesome friends who have made grad school, believe it or not, fun: Donde Anderson, JoAnn Boyd, Mike Boyle, Cynthia Chiang, Jinseong Heo, Isabel Hsiao, Ilya Mandel, Peng Oh, Etienne Racine, Paige Randall, and Jeanette Tsai.

At last, my biggest thanks to my wonderful loving parents and brother who have always believed in me.

Abstract

Strong gravitational lens systems provide a tool for probing galaxy mass distributions (independent of their light profiles) and for measuring cosmological parameters. In a strong lens system, the background source intensity distribution is multiply imaged. If the source intensity is time varying, then the multiple images of the variable source are delayed in time relative to each other due to the different light travel time along the multiple light paths. One can use lens systems to measure the Hubble constant by obtaining the relative time delays between the multiple images and modeling the lens potential. B1608+656 is a quadruply imaged gravitational lens system with a spatially extended source intensity distribution and two interacting galaxy lenses. This system is unique in that the three relative time delays between the four images were measured accurately with errors of only a few percent, and it thus provides an opportunity to measure the Hubble constant with high precision. The extended source intensity distribution in B1608+656 provides additional constraints on the lens potential, though simultaneous determination of the source intensity and lens potential distribution is needed. The presence of dust and interacting galaxy lenses further complicate this system. We present a comprehensive analysis in a Bayesian framework that takes into account the extended source intensity distribution, interacting galaxy lenses, and the presence of dust for reconstructing the lens potential. Using the deep *HST* ACS observations on B1608+656, the resulting statistical uncertainty on H_0 associated with the lens modeling is limited by the uncertainty in the best time delay measurement ($\sim$3%). The dominant systematic error on H_0 is due to the effects of the environment on B1608+656 (mass-sheet degeneracy). By using the measured velocity dispersion of the lens galaxies and considering the mass structures along the

line of sight to B1608+656, we place constraints on the external convergence associated with galaxy groups and mass structure along the line of sight. The resulting Hubble constant from B1608+656 is $H_0 = 72 \pm 2$ (stat.) ± 4 (syst.) km s^{-1} Mpc^{-1}.

Contents

List of Figures

List of Tables

Chapter 1

Introduction: Brief History of Hubble Constant Measurements

Ever since Edwin Hubble discovered the expansion of the Universe in 1929 (Hubble 1929), one of the key parameters in cosmology has been the Hubble constant (H_0, measured in units of km s^{-1} Mpc^{-1}) that sets the age and size of our Universe. Following the notation in Dodelson (2003), the Hubble constant is the present value of the Hubble rate that is defined by

$$H(t) \equiv \frac{da/dt}{a}, \tag{1.1}$$

where $a(t)$ is the cosmic scale factor. The evolution of the cosmic scale factor is given by the Friedmann equation

$$H^2(t) = \frac{8\pi G}{3}\left[\rho(t) + \frac{\rho_{\rm cr} - \rho_0}{a^2(t)}\right], \tag{1.2}$$

where G is Newton's constant, $\rho(t)$ is the energy density in the universe with ρ_0 as the present value, and $\rho_{\rm cr}$ is the critical density defined by

$$\rho_{\rm cr} = \frac{3H_0^2}{8\pi G}. \tag{1.3}$$

Since the Universe is expanding, galaxies are receding from us. Therefore, the wavelength of light ($\lambda_{\rm emit}$) emitted from the galaxies is shifted to longer wavelengths ($\lambda_{\rm obs}$)

when observed. We define the redshift z as

$$1 + z \equiv \frac{\lambda_{\rm obs}}{\lambda_{\rm emit}} = \frac{1}{a}. \tag{1.4}$$

For low redshifts ($z \ll 1$), Doppler formula applies and $z \simeq \frac{v}{c}$. Hubble's law states that at low redshifts ($z \ll 1$), galaxies at a distance d are receding from us at a velocity

$$v = H_0 d. \tag{1.5}$$

However, galaxies also have peculiar velocities due to density fluctuations in the Universe. To have negligible peculiar velocities for measuring H_0 via equation (1.5), one should measure velocities out to $\sim$20,000 km s^{-1} or distances out to $\sim$300 Mpc. Measuring velocities (redshifts) is relatively easy, but measuring distances is challenging because the intrinsic brightness of astrophysical objects is generally unknown. One way astronomers try to solve this problem is by finding classes of objects where the intrinsic brightness of such an object is correlated with an observable. These classes of objects are generally referred to as "standard candles" and can be stellar objects or galaxies. However, no single type of standard candle can provide distance measures on all distance scales (e.g., stellar objects can only measure distances to nearby galaxies before they are too faint to be seen in more distant galaxies). This leads to a distance ladder where methods for intermediate to far distance measurements are calibrated using methods for nearby distance measurements. Recall that to get H_0 from equation (1.5), one needs to get to large distances so as to be in the Hubble flow where peculiar velocities are small. Alternatively, one can bypass the distance ladder by employing techniques that give a one-step distance measurement to distant objects. Strong gravitational lensing is one of these methods that is independent of the distance ladder.

We give a brief history and description of methods to obtain H_0. From 1927 to 1962, measurements of H_0 steadily decreased from $\sim$500 to $\sim$75 (e.g., Hubble 1929; Behr 1951; Holmberg 1958; Sérsic 1960; Sandage 1962). These values were based on extragalactic distance determinations using brightest stars, size of HII regions, and

mean luminosity of bright galaxies that relied mostly on Cepheid variables. Between 1962 and 1975, it was found that earlier distance measurements of local galaxies were too low due to the brightest spirals of luminosity class I (which were used as standard candles) being brighter than expected. This lowered the value of H_0 to ~ 55 (Sandage & Tammann 1975). Since 1975, tremendous efforts were made to measure H_0 using various methods, and the results oscillated between 55 and 100. All methods rely on some form of distance measure, which can be from individual objects, global galaxy properties, or gravitational effects. Below we give a brief description for some of the known distance indicators and their resulting output H_0 where applicable.

Single Objects as Distance Indicators

- *Cepheids.* These variable stars have their periods related to their intrinsic luminosities (P-L relation). The Cepheids' distances have mostly been used to calibrate distances to secondary distance indicators such as the Tully-Fisher relation (see below). However, it has been realized that the Cepheids' P-L relation is not universal, which has complicated the determination of Cepheid distances. For instance, the P-L relation in the Galaxy differs from that in the LMC (e.g., Tammann, Sandage, & Reindl 2003; Sandage, Tammann, & Reindl 2004), which may be due to dependence on metallicity (e.g., Sakai et al. 2004).

- *RR Lyr stars.* Like Cepheids, these variable stars have P-L relations that make them distance indicators. However, the P-L relations are also dependent on metallicity. The distances from RR Lyr stars are so far confined to the Local Group. For a recent review, see Sandage & Tammann (2006).

- *Size of HII regions.* The sizes of the largest HII regions in late-type galaxies were used as distance indicators (e.g., Sandage 1962). However, it has been discovered that the size of the HII region depends on the size of the parent galaxy, which makes this method no longer competitive.

- *Globular clusters (GCs).* Globular clusters have bell-shaped luminosity func-

tions (LF), and the peak of the luminosity was proposed to be a standard candle (van den Bergh et al. 1985) (for review see Tammann & Sandage 1999). One of the most recent measurement by Kavelaars et al. (2000) gave $H_0 = 69 \pm 9$. However, the formation of GCs may not be a unique process.

- *Planetary nebulae (PNe).* A planetary nebula is a glowing shell of gas that is formed around a white dwarf progenitor. The method of using brightest planetary nebulae as distance indicators was proposed by Ford & Jenner (1978). Recently, Ciardullo et al. (2002) obtained $H_0 = 78 \pm 7$ using this method. However, the method seems to depend on the population size (Bottinelli et al. 1991; Tammann 1993), chemical composition, age (Mendez et al. 1993), and dynamics (Sambhus et al. 2006).

- *Tip of the red-giant branch (TRGB).* The tip of the red-giant branch corresponds to the brightest red giants. Da Costa & Armandroff (1990) showed that the TRGBs in globular clusters have constant absolute I-magnitude, independent of metallicity. TRGBs are calibrated using GCs and RR Lyrae stars so they are independent of the Cepheids distance indicators. Some recent (within 5 years) applications of the method are done by Karachentsev et al. (2003) and Sakai et al. (2004).

- *Type Ia Supernovae (SN).* Type Ia SN have characteristic light curves where the width of the curve is related to the abolute magnitude of the SN. This makes them ideal standard candles because SN are bright and are thus accessible out to large distances. Nonetheless, they still depend on the distance ladder as SN distances are usually calibrated using Cepheid distances. Recent measurements of H_0 using this method give $H_0 = 73 \pm 4$ (statistical) ± 5 (systematic) (Riess et al. 2005) and $H_0 = 62.3 \pm 1.3$ (random) ± 5.0 (systematic) (Sandage et al. 2006).

Galaxies as Distance Indicators

- *Luminosity class (LC) of spiral galaxies.* Spiral galaxies can be used as a distance indicator based on the correlation between the luminosity and the shape of the spiral structures. Using this method, Sandage (1999) obtained $H_0 = 55 \pm 3$. The error associated with the value is the random error internal to the method and does not include the error on the distance moduli of calibrating galaxies or systematic error of the Cepheid PL zero point. Systematic errors for methods that depend on distance ladders can often be comparable, if not greater, than random errors. These systematic errors can therefore significantly bias the results if not included properly.

- *Brightest cluster galaxies (BCG).* This distance indicator assumes that the BCGs in clusters have the same luminosity. The last paper using this method results in $H_0 = 54.2 \pm 5.4$ (Sandage & Hardy 1973; Tammann 2006).

- *Surface brightness fluctuations (SBF).* The method applies to distant galaxies where individual stars are not resolvable. Galaxies that are further away have smaller statistical surface brightness fluctuations because the number of stars in a pixel increases with the distance to the galaxy. Tammann (2006) concluded that the SBF was able to measure relative distances within 13%, but was not to be used for H_0.

- *Fundamental Plane (FP) method.* Velocity dispersions of E/S0 galaxies are correlated to their luminosities (Minkowski 1962; Faber & Jackson 1976). More generally, observations indicate that these galaxies lie on a "fundamental plane" in the velocity dispersion, effective radius, and luminosity space. The FP can be described by a $D_n - \sigma$ relation (Dressler et al. 1987) (where D_n is a suitably normalized diameter) or a velocity dispersion-mean surface brightness relation (Djorgovski & Davis 1987). Calibrating the distances from the FP method with respect to the Virgo cluster gives $H_0 = 57.0 \pm 4.4$ (Federspiel 1999) and with respect to the Coma cluster gives $H_0 = 57.0 \pm 4.4$ (Jorgensen et al. 1996;

Tammann 2006).

- *Tully-Fisher relation (TF).* A spiral galaxy's rotation velocity as measured by the width of 21 cm line is related to the luminosity of the galaxy. This relation was used for distance measurements by Tully & Fisher (1977), and thus the relation is known as the Tully-Fisher relation for a spiral galaxy's luminosity and rotation velocity. Calibrating the distances from TF method with respect to the Fornax cluster, $H_0 = 65.6 \pm 4.1$ (Giovanelli et al. 1997; Dale et al. 1999; Tammann 2006).

Hubble Space Telescope (*HST*) Key Project (KP)

This program used Cepheids to measure distances to nearby galaxies with a zero point in the Large Magellanic Cloud (LMC). Universal P-L relations were adopted, but were corrected for environment effects (e.g., reddening and metallicity dependence). These Cepheid distances then serve as calibrators for secondary distance indicators that include Type Ia supernovae, Tully-Fisher, surface brightness fluctuations, Type II supernovae, and the fundamental plane. All secondary methods gave H_0 in the range of $70-72$, except for the fundamental plane which gave 82 (all with $\sim$10% error). Combining all measurements from secondary distance indicators, Freedman et al. (2001) obtained $H_0 = 72 \pm 2$ (stat.) ± 7 (syst.). Dominant sources of error are from uncertainties in the distance to LMC, photometric calibration of *HST* Wide Field and Planetary Camera 2, metallicity correction of Cepheid P-L relation, and cosmic scatter in the velocity field.

Astrophysical Phenomena with Distance Measures

- *Sunyaev-Zel'dovich (SZ) effect.* The SZ effect is a distortion in the cosmic microwave background (CMB) due to some CMB photons being Compton scattered by electrons in the hot gas of rich clusters of galaxies. This results in an excess of photons in higher frequencies and a deficit of photons in lower frequencies. The distortion allows one to determine the electron density in the gas,

which together with X-ray flux observations (Bremsstrahlung radiation emitted by the electrons scattering off protons), permits one to determine the angular diameter distance to the cluster (e.g., Birkinshaw 1999). Bonamente et al. (2006) determined the distance to 38 clusters, selected to be orientation-unbiased, using Chandra X-ray data, Owens Valley Radio Observatory/Berkeley-Illinois-Maryland Association interferometric arrays SZ data and various spherical cluster models to derive $H_0 = 77 \pm 4$ (stat.) ± 10 (syst.). Using only relaxed clusters, Schmidt et al. (2004) obtained $H_0 = 69 \pm 8$ (stat.) and claimed that systematic errors were unimportant.

- *Maser distances.* Some active galactic nuclei (AGN) show strong sources of water maser emission (in the radio frequency) in the accretion disks around the central supermassive black holes. By measuring the positions, velocities, and accelerations of these masers and by modeling the accretion disk, one can determine the distance to the maser-host galaxy (e.g., Lo 2005). There are currently 63 known AGNs containing masers, but only a few has masers bright enough for distance determination.[1] Most of the sample are discovered by the Water Maser Cosmology Project whose goal is to determine H_0 to a few percent accuracy. The galaxy NGC 4258 is the first galaxy to which this method has been applied to obtain a maser distance (Herrnstein et al. 1999). Recently, Macri et al. (2006) used the maser distance of NGC 4258, four well-observed Type Ia SNe and their new calibration of Cepheid distance scale to obtain $H_0 = 74 \pm 3$ (random) ± 6 (syst.).

- *Cosmic Microwave Background (CMB).* The Wilkinson Microwave Anisotropy Probe (WMAP)'s three year temperature and polarization data gives $H_0 = 73 \pm 3$ if one assumes that the universe is flat and that dark energy is described by a cosmological constant with $w = -1$. If $w > -1$ then H_0 decreases, and if flatness assumption relaxed, H_0 can increase or decrease. Combining CMB with the baryon acoustic oscillations in large-scale structure observations, Eisenstein

[1] Water Maser Cosmology Project.

et al. (2005) obtained $H_0 = 69.2 \pm 2.1$, assuming flatness and $w = -1$. If flatness or $w = -1$ assumptions relaxed, then H_0 decreases and has much lower precision.

- *Gravitational lensing.* Strong gravitational lensing occurs when a background source object (e.g., star, galaxy) is being multiply imaged by a gravitational lens (e.g., star, galaxy, cluster of galaxies). If the source in such a system is time varying, then the multiple images of the variable source are delayed in time relative to each other due to the different light travel time along the multiple light paths. By measuring the time delay between the multiple images and modeling the mass distribution of the gravitational lens, one can determine the value of H_0 (from ratios of angular diameter distances) (Refsdal 1964). Recently, Saha et al. (2006) performed a simultaneous analysis of 10 lens systems that have time delay measurements to obtain $H_0 = 72^{+8}_{-11}$. Oguri (2007) measures $H_0 = 68 \pm 6$ (stat.) ± 8 (syst.) using a statistical approach by combining data from 16 published time delay quasars. In this thesis we will show how one can measure H_0 with <10% error using a single well-measured time delay lens system.

For more details on the history and measurement of H_0, we refer the reader to Tammann (2006). We mention that Tammann (2006) said little regarding gravitational lensing as a method; we compensate for it in this thesis. Freedman & Turner (2003) is a recent review on measuring and understanding the Universe.

As seen in the list above, recent values of H_0 are ∼70 with ∼10% error. Perhaps the two most well-known recent measurements come from the *HST* KP and WMAP. As listed above, the *HST* KP gives 72 ± 8, but we note that the KP depends on distance ladders that are prone to systematic effects (such as the period-luminosity relation of the Cepheids being dependent on metallicity). WMAP gives a tight error bar of ±3, but it assumes that the Universe is flat and that dark energy is described by a cosmological constant with $w = -1$. The value of H_0 from WMAP changes markedly if either of these two assumptions is relaxed. Due to the degeneracies in the

Hubble constant with other cosmological parameters, it is crucial to determine H_0 to better precision than the current $\sim$10% for studying cosmology. Hu (2005) stated that an H_0 that is accurate to percent level is the single most useful complement to CMB parameters for dark energy studies. With H_0 being such an important parameter, it is essential to measure it using a full range of methods. In this thesis, we present strong gravitational lensing as an independent and competitive probe that provides a one-step method (i.e., independent of distance ladders) to obtain H_0.

In chapter 2, we go over the theory of gravitational lensing and describe the properties of quadruply imaged gravitational lens systems. Much of this thesis is based on Bayesian analysis, which we introduce in chapter 3. We explain how to fit a model to a given set of data and how to rank the various models. We apply Bayesian analysis to source intensity reconstruction in gravitational lensing in chapter 4 and demonstrate the source reconstruction using simulated data. In chapters 5 and 6, we describe the observations of B1608+656 and present the image-processing techniques employed. The lens modeling is presented in chapter 7, which consists of two parts: initial parametric modeling and pixelated lens potential reconstruction. Chapter 8 contains the error analysis, and the inferred value of the Hubble constant from B1608+656. Finally, in chapter 9 we discuss independent studies that are related to this thesis. Throughout this thesis, we assume a flat Λ-CDM universe with cosmological parameters of $\Omega_m = 0.3$ and $\Omega_\Lambda = 0.7$, where Ω_m (Ω_Λ) is the ratio of the matter (dark energy) density to the critical density today. Unlike CMB, H_0 from gravitational lensing depends weakly on the flat Λ-CDM assumption because H_0 from lensing is obtained from a ratio of angular diameter distances.

Chapter 2

Gravitational Lensing

In this chapter, we present the theory of gravitational lensing in section 2.1, and describe the properties of quadruply imaged lens systems through a detailed study of the gravitational lens B1608+656 in section 2.2. Most of the material in this chapter was published in Suyu & Blandford (2006).

2.1 Theory

2.1.1 Definitions and Notation

This section summarizes the theory of gravitational lensing. We follow Kochanek, Schneider, & Wambsganss (2006) for the theory of gravitational lensing.

Figure 2.1 shows a typical gravitational lensing diagram. The optical axis is defined as the straight line connecting us and some reference point such as the center of mass of the lens in the lens (image) plane. Any massive object can act as a gravitational lens: stars, galaxies, and clusters of galaxies. In this thesis, we focus on galaxy lenses. Three possible paths for light rays to travel from the source to us are denoted by 1, 2, and 3. Path 2 corresponds to the case with no deflection. The distances D_d, D_s, and D_{ds} are, respectively, the angular diameter distance from us to the lens, from us to the source, and from the lens to the source. For a flat Λ-CDM universe, the expression for the angular diameter distance between redshifts z_1 and

z_2 is

$$D(z_1, z_2) = \frac{c}{H_0} \frac{1}{1+z_2} \left[\int_{z_1}^{z_2} \frac{dz'}{\sqrt{\Omega_m (1+z')^3 + (1-\Omega_m)}} \right], \tag{2.1}$$

where Ω_m $(1 - \Omega_m)$ is the ratio of the matter (dark energy) density to the critical density today, c is the speed of light, and H_0 is the value of the Hubble constant today (e.g., Kochanek et al. 2006). The radiation component has been neglected in equation (2.1) because the redshifts of the source and lens are usually $\lesssim$10. Equation (2.1) reduces to Hubble's law in equation (1.5) with $z_1 = 0$, $z_2 \simeq \frac{v}{c}$ (for $z_2 \ll 1$) and $(1 + z_2) \times D(z_1, z_2)$ as the comoving distance. The angular coordinates on the source and image planes with respect to the optical axis are $\vec{\beta} = (\beta_1, \beta_2)$ and $\vec{\theta} = (\theta_1, \theta_2)$, respectively. Throughout this thesis, coordinate vectors will be denoted by italic scalars with arrows. On the other hand, vectors that are not two-dimensional coordinates will be in bold italic fonts. The physical coordinates (measured in, for example, Mpc) on the source and image planes are $\vec{\eta} = (\eta_1, \eta_2)$ and $\vec{\xi} = (\xi_1, \xi_2)$. They are related to the angular coordinates via

$$\vec{\beta} = \frac{\vec{\eta}}{\eta_0} \quad \text{and} \quad \vec{\theta} = \frac{\vec{\xi}}{\xi_0} \qquad \text{with} \qquad \eta_0 = \frac{D_s}{D_d} \xi_0, \tag{2.2}$$

where ξ_0, an otherwise arbitrary distance scale factor, is appropriately chosen to be $\xi_0 = D_d$.

The lens equation governing the deflection of light rays is

$$\vec{\beta} = \vec{\theta} - \vec{\alpha}(\vec{\theta}), \tag{2.3}$$

where $\vec{\alpha}(\vec{\theta})$ is the scaled deflection angle that is the gradient of a scalar function called the lens (or deflection) potential:

$$\vec{\alpha}(\vec{\theta}) = \vec{\nabla} \psi(\vec{\theta}). \tag{2.4}$$

The lens potential is twice the two-dimensional Newtonian potential that is the solution to the two-dimensional Poisson equation $\nabla^2 \psi_{\text{newton}}(\vec{\xi}) = 8\pi G \Sigma(\vec{\xi})$, where $\Sigma(\vec{\xi})$,

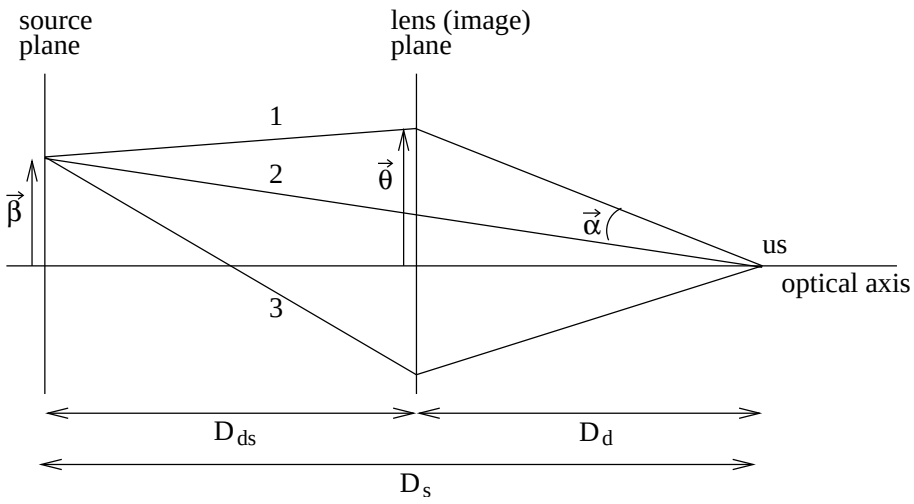

Figure 2.1: The gravitational lensing diagram shows three possible paths for the light rays to travel from the source to us. The angular coordinate on the source (image) plane is $\vec{\beta}$ ($\vec{\theta}$), and the deflection angle is $\vec{\alpha}$. The distances D_{ds}, D_d, and D_s are angular diameter distances.

the surface mass density, is the two dimensional projection of the lens mass density. We define the dimensionless surface mass density as

$$\kappa(\vec{\theta}) = \frac{\Sigma(\xi_0\vec{\theta})}{\Sigma_{cr}} \qquad \text{with} \qquad \Sigma_{cr} = \frac{c^2 D_s}{4\pi G D_d D_{ds}}, \tag{2.5}$$

where D_s, D_d, D_{ds} were previously defined as the angular diameter distances, c is the speed of light, and G is the gravitational constant. The physical significance of Σ_{cr}, the critical surface mass density, is that the condition $\Sigma(\vec{\xi}) > \Sigma_{cr}$ at a point $\vec{\xi}$ in the lens plane is sufficient (but not necessary) for possible multiple images (strong lensing) to occur.

In terms of the dimensionless surface mass density, denoted by $\kappa(\vec{\theta})$, the lens potential is

$$\psi(\vec{\theta}) = \frac{1}{\pi}\int_{\Re^2} d^2\theta' \kappa(\vec{\theta'}) \ln|\vec{\theta} - \vec{\theta'}|. \tag{2.6}$$

The lens equation (2.3) comes from Fermat's principle, which states that the arrival time delay of a light ray from the source to us must be stationary with respect to variations in the path of the light ray. For a given position of the source at $\vec{\beta}$,

the time delay has two contributions: a geometric component due to the light rays traveling different distances to get to us and a gravitational component due to the Shapiro effect. The expression for the arrival time delay relative to the case of no lensing is

$$T(\vec{\theta},\vec{\beta}) = \frac{\xi_o^2}{c}\frac{D_s}{D_d D_{ds}}(1+z_d)\left[\frac{(\vec{\theta}-\vec{\beta})^2}{2} - \psi(\vec{\theta})\right], \tag{2.7}$$

where z_d is the redshift of the lens. Using simple geometry, one can show that the first term in the square brackets is the geometric component; the second term is the gravitational component. By applying Fermat's principle, which is mathematically stated as $\vec{\nabla}_{\vec{\theta}} T(\vec{\theta}) = \vec{0}$, we get the lens equation (2.3). It is important to know that the connection between $\vec{\nabla}_{\vec{\theta}} T(\vec{\theta}) = \vec{0}$ and the lens equation (2.3) is only valid when the surface mass density is smooth. If the time delay surface has an extremum at a location where the surface mass density is singular, there may not be an image at that location (Kochanek et al. 2006).

The constant coefficient in equation (2.7) is proportional to the angular diameter distance and hence inversely proportional to the Hubble constant in a flat Λ-CDM universe (see equation (2.1)). Therefore, by measuring the relative time delays between the various images, we can in principle deduce the value of the Hubble constant if we know the source position ($\vec{\beta}$) and the lens potential ($\psi(\vec{\theta})$).

An important feature of gravitational lensing is the conservation of surface brightness. Image magnification in lensing results in an increase in image flux, permitting detection of distant sources that would otherwise be too faint to be observed. This is the basis for using gravitational lenses as cosmic telescopes. To characterize the magnifications of images in gravitational lensing, a Hessian is used

$$\mathbf{A}(\vec{\theta}) = \frac{\partial\vec{\beta}}{\partial\vec{\theta}}. \tag{2.8}$$

A notational clarification: matrices will be in bold-faced sans serif throughout this

thesis. Using the lens equation (2.3), the above equation can be written as

$$\mathbf{A}(\vec{\theta}) = \begin{pmatrix} 1-\psi_{11}(\vec{\theta}) & -\psi_{12}(\vec{\theta}) \\ -\psi_{12}(\vec{\theta}) & 1-\psi_{22}(\vec{\theta}) \end{pmatrix}, \tag{2.9}$$

where the subscript 1 (or 2) in ψ indicates a derivative with respect to θ_1 (or θ_2). The magnification matrix is defined as $\boldsymbol{\mu} = \mathbf{A}^{-1}$, and the associated magnification factor is

$$\mu(\vec{\theta}) = \frac{1}{\det \mathbf{A}(\vec{\theta})}. \tag{2.10}$$

According to equation (2.10), the positions $\vec{\theta}$ with $\det \mathbf{A}(\vec{\theta}) = 0$ have divergent magnification;[1] the loci of such points on the image plane define the *critical curves*. Using the lens equation (2.3), critical curves on the image plane are mapped to *caustic curves* (or simply *caustics*) on the source plane. The caustic curves separate regions of different image multiplicities.

2.1.2 Mass-Sheet Degeneracy

We follow Kochanek et al. (2006) for a general description of the mass-sheet degeneracy and refer readers to Kochanek et al. (2006) for details. Mass-sheet degeneracy, as the name suggests, refers to a degeneracy in the mass modeling with respect to additions of mass sheets to the lens mass models (but with appropriate scaling of the original distribution). Suppose we have a lens model with surface mass density $\kappa(\vec{\theta})$ (and corresponding lens potential $\psi(\vec{\theta})$) that fits to the observables (i.e., image positions and flux ratios for point sources, and the Einstein ring for extended sources). Consider the following transformation

$$\kappa_\lambda(\vec{\theta}) = (1-\lambda) + \lambda\kappa(\vec{\theta}), \tag{2.11}$$

[1]Since the geometric optics that leads to equation (2.10) fails near critical curves, wave optics must be used. The resulting magnification from wave optics is finite, though potentially very high.

where $\kappa_\lambda(\vec{\theta})$ is the transformed surface mass density, $1-\lambda \equiv \kappa_c$ corresponds to a uniform mass sheet, and the original $\kappa(\vec{\theta})$ is rescaled. This new model κ_λ provides equally good fit to the observables, as we show below.

The general form of the transformation of the lens potential that leads to equation (2.11) is

$$\psi_\lambda(\vec{\theta}) = \frac{1-\lambda}{2}|\vec{\theta}|^2 + \vec{a}\cdot\vec{\theta} + c + \lambda\psi(\vec{\theta}), \tag{2.12}$$

where $\nabla^2\psi_\lambda(\vec{\theta}) = 2\kappa_\lambda(\vec{\theta})$, $\nabla^2\psi(\vec{\theta}) = 2\kappa(\vec{\theta})$, $\vec{a} = (a_1, a_2)$ is a constant vector, and c is a constant. The lens equation for the transformed potential is

$$\begin{aligned} \vec{\beta}_\lambda &= \vec{\theta} - \vec{\nabla}\psi_\lambda(\vec{\theta}) \\ &= \lambda\vec{\beta} - \vec{a}, \end{aligned} \tag{2.13}$$

where we substituted equation (2.12) and used $\vec{\beta} = \vec{\theta} - \vec{\nabla}\psi(\vec{\theta})$ to get from the first to the second line. Therefore, the result of the mass-sheet transformation is to rescale the entire source distribution by λ and translate it by $\vec{a}$. Since the source distribution is not directly observable and the origin of the coordinates on the source plane is arbitrary, the observed image positions and the *relative* flux ratios are invariant under equation (2.11). In fact the shape of the lensed extended images is also invariant. In other words, we cannot distinguish the model κ_λ from κ using gravitational lensing alone since gravitational lensing only measure relative positions and fluxes. This degeneracy can be broken if we know something about the absolute size/luminosity of the source intensity or an absolute mass for the lens (e.g., from observations of the stellar dynamics, which we discuss in chapter 8). This degeneracy is problematic for the determination of the Hubble constant because the Fermat potential, contrary to the image positions and fluxes, does change under the transformation from κ to κ_λ. The Fermat potential for the transformed lens potential $\psi_\lambda(\vec{\theta})$ corresponding to $\kappa_\lambda(\vec{\theta})$

is

$$\begin{aligned}\phi_\lambda(\vec{\theta};\vec{\beta}_\lambda) &= \frac{1}{2}(\vec{\theta}-\vec{\beta}_\lambda)^2 - \psi_\lambda(\vec{\theta}) \\ &= \lambda\phi(\vec{\theta};\vec{\beta}) + \text{const.}, \end{aligned} \tag{2.14}$$

where const. depends only on $\vec{\beta}$. Since we can only measure the relative time delays between the images (and $\vec{\beta}$ is the same for all images), only the relative Fermat potential matters so const. drops out: $\Delta\phi_\lambda(\vec{\theta};\vec{\beta}_\lambda) = \lambda\Delta\phi(\vec{\theta};\vec{\beta})$. Therefore, given measured relative time delays Δt, which are inversely proportional to H_0 and proportional to the relative Fermat potential, the scaled model κ_λ (with the mass sheet $\kappa_c = 1-\lambda$) would lead to an H_0 that is a factor λ lower than the model κ. In other words, if there is any external convergence κ_c due to environment or mass structure along the line of sight to the lens systems that is not incorporated in the lens modeling, then

$$H_0^{\text{true}} = (1-\kappa_c)H_0^{\text{model}}. \tag{2.15}$$

In chapter 8, we will describe methods and observations that help break the mass-sheet degeneracy. For now, readers should simply keep in mind this inherent degeneracy in lensing.

Having gone through the basic definitions and formalism in the previous two subsections, we use these definitions to investigate quadruply imaged gravitational lens systems in the next section.

2.2 Properties of Quadruply Imaged Lens Systems

The gravitational lens B1608+656 will be used to illustrate the properties of quadruply imaged gravitational lens systems. Chapter 6 contains images of B1608+656 that show four images (labeled by A, B, C and D) and two lens galaxies (G1 and G2). To investigate the anatomy of the quad B1608+656, we use the mass distribution model proposed by Koopmans et al. (2003b) that is described in more detail in section 7.2.

The parametric form of the dimensionless surface mass density for each of the two lens galaxies is a singular power law ellipsoid (SPLE):

$$\kappa(\theta_{gal_1}, \theta_{gal_2}) = b \left[\theta_{gal_1}^2 + \left(\frac{\theta_{gal_2}}{q_l} \right)^2 \right]^{\frac{1-\gamma'}{2}}, \tag{2.16}$$

where $(\theta_{gal_1}, \theta_{gal_2})$ are coordinates relative to the galaxy center and b, q_l, and γ' are parameters to fit the data. The origin of coordinates $\vec{\theta}$ is set at the position of image A. Each of the lens galaxies is centered at the coordinates $(\theta_{l1}, \theta_{l2})$ and is rotated by a major-axis position angle $\theta_{\rm PA}$ that is measured from north to east (top to left). There is an additional external shear centered on G1 whose contribution to the lensing potential, in polar coordinates relative to the shear center ((r, ϕ) with $\theta_{\rm sh_1} = r\cos(\phi)$ and $\theta_{\rm sh_2} = r\sin(\phi)$), is

$$\psi_{\rm ext}(\vec{\theta_{\rm sh}}) = \frac{1}{2}\gamma_{\rm ext} r^2 \cos(2\phi), \tag{2.17}$$

where $\gamma_{\rm ext}$ is a parameter characterizing the shear strength. The angle of the external shear, $\theta_{\rm ext}$, is measured from the positive $\theta_{\rm sh_1}$-axis in a counterclockwise direction. An external shear angle of $\theta_{\rm ext} = 0$ corresponds to a stretch along the $\theta_{\rm sh_1}$-axis. We adopt the parameter values of the SPLE1+D (isotropic) model[2] in Koopmans et al. (2003b) and list them in table 2.1.

2.2.1 Critical and Caustic Curves

The critical curves on the image plane and the caustic curves on the source plane of the SPLE1+D (isotropic) model in Koopmans et al. (2003b) are shown in figure 2.2 in the middle panel and the left-hand panel, respectively. The locations of the lens galaxies are indicated by open triangles on the image plane. The marked source and image locations will be discussed in the next section. With the two elliptical lens galaxies, the large critical curve loop is a deformed version of an elliptical curve of one singular power law ellipsoid (equation (2.16)). The corresponding diamond-shaped

[2]SPLE1+D (isotropic): SPLE refers to singular power-law ellipsoid, 1 refers to a prior on the slope of G2 ($\gamma'_{\rm G2} = 2.00 \pm 0.10$) imposed in the lens modeling, and isotropic means isotropic models in stellar dynamics.

Table 2.1: Parameter values for the B1608+656 SPLE1+D (isotropic) model in Koopmans et al. (2003b)

lens galaxy	G1	G2
b	0.526	0.269
q_l	0.604	0.318
γ'	2.05	2.12
centroid $(\theta_{l1}, \theta_{l2})$	(0.425, −1.069)	(−0.291, −0.928)
position angle $\theta_{\rm PA}$ (°)	77.0	68.4
$\gamma_{\rm ext}$	0.077	
shear angle $\theta_{\rm ext}$(°)	13.4	

Note. — These parameter values appear in equations (2.16) and (2.17).

caustic curve, known as an astroid, is typical for elliptical mass distributions. An astroid is composed of four folds (branches of smooth curves) joining at four cusps. An individual power law ellipsoid has an astroid that is symmetrical with respect to the semimajor and semiminor axis of the lens. With the two lens galaxies in the SPLE1+D (isotropic) model, we have an asymmetry in the astroid and two additional small triangular caustics, called the deltoids, that map into the small loops on the image plane.

2.2.2 Image Positions and Time Delay Surface

It is instructive to see how the images move on the image plane as the source is displaced. Understanding such movements is important for analyzing quads and for defining the limit curves in the next section. Figure 2.2 shows the locations of the images, labeled by A, B, C, D, and E (middle panel), when the source is at the center of the astroid caustic (left-hand panel). Despite having five images, the system is called a quad because the central image is usually demagnified and lies near the lens galaxies, making it nearly observationally invisible.[3] The arrival time delay contours in the right-hand panel show that the image locations are at the time delay extrema or saddles, except for the extrema where the surface mass densities are nonsmooth

[3]We refer the reader to Winn, Rusin, & Kochanek (2004) for candidates of central image detections in gravitational lens systems.

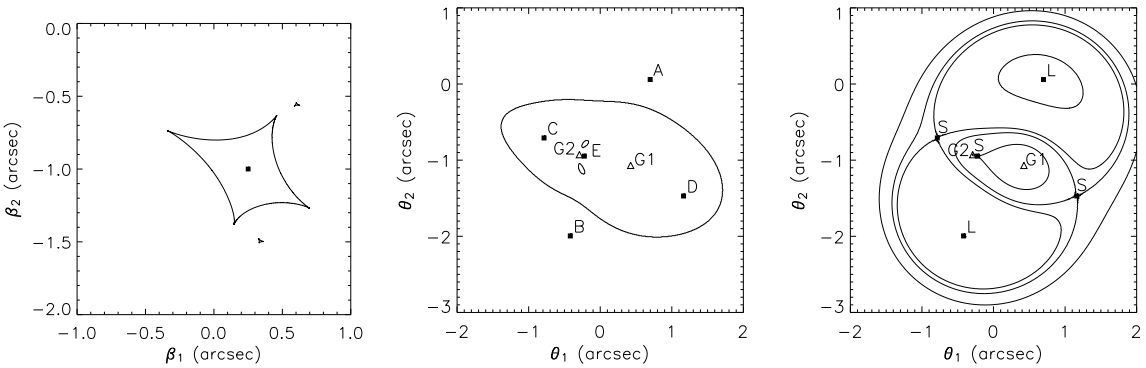

Figure 2.2: Left-hand panel: source is near the center within the astroid caustic of the B1608+656 SPLE1+D (isotropic) model in Koopmans et al. (2003b). Middle panel: the corresponding five images (A, B, C, D, and E), the lens galaxy positions (G1 and G2) indicated by open triangles, and the critical curves. Right-hand panel: crucial time delay contours for demonstrating Fermat's principle. The time delay at each image position is a minimum (L for "low") or a saddle (S). The scales on the source plane and image plane are different due to magnification of the images.

(Kochanek et al. 2006). At the centroids of G1 and G2 whose locations are given in table 2.1, the time delay achieves local maxima, but there are no corresponding images because the surface mass densities are singular at the galaxy centroids in the model described by equation (2.16). Ignoring the central image (E, which is finitely de-magnified), the two images (C and D) inside the critical curve are time delay saddles, and the two images (A and B) outside the critical curve are time delay minima. This is true in general for quads.

Figure 2.3 shows the image locations and the time delay contours as the source moves across a fold from within the caustic. As the source approaches a fold, two of the images (B and C for the upper fold of interest) that are separated by the critical curve come together. When the source is on the fold, the two images merge to become one at the corresponding point on the critical curve. Finally, when the source moves across the fold, the merged image disappears. The merging and disappearance of the two images can be explained using the lemniscate time delay contour (figure-eight shaped contour containing a saddle with two minima) in the right-hand panels. When the source approaches a fold, the time delay saddle of the lemniscate joins with one of its two associated local minima; after the source crosses the fold, only one time

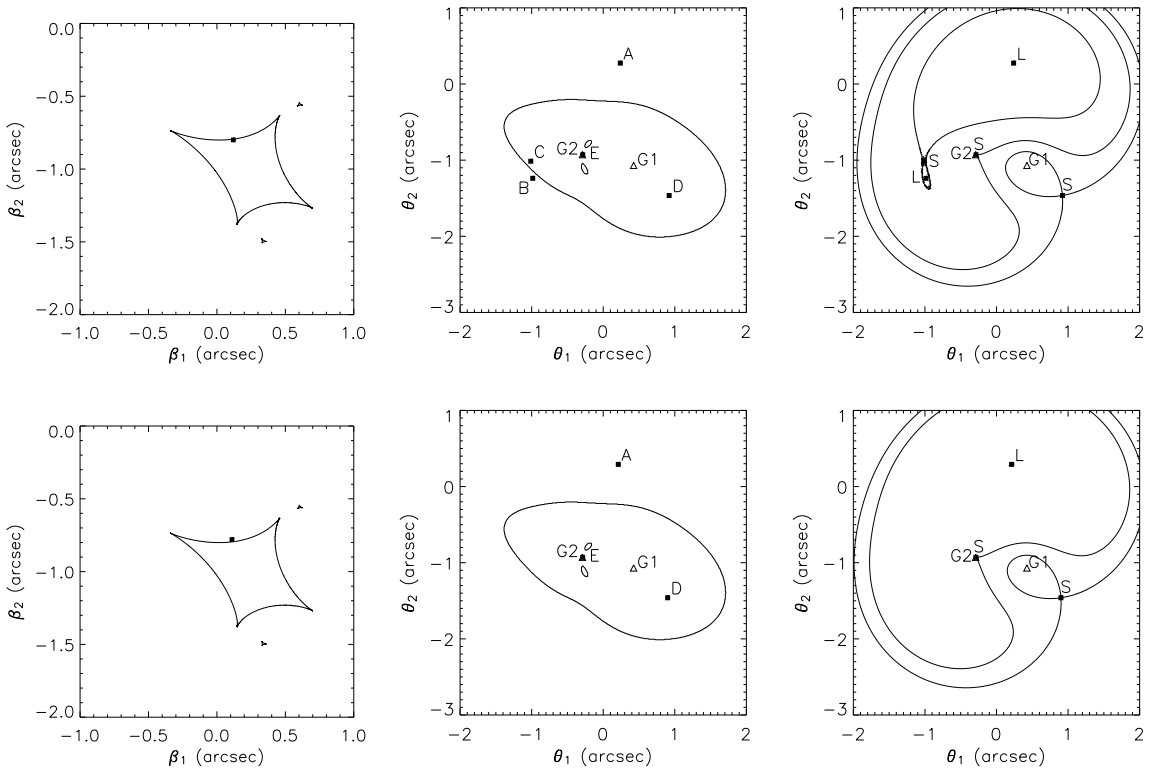

Figure 2.3: Left-hand panels: source position displaced across a fold from inside (top) to outside (bottom) of the astroid caustic curve of B1608+656 SPLE1+D (isotropic) model. Middle panels: image positions (A, B, C, D, and E) corresponding to the source positions shown in the left-hand panels, lens galaxy positions (G1 and G2) indicated by open triangles, and the critical curves. Right-hand panels: corresponding time delay contours. Letter L (for low) or S at each image location represents a time delay minimum or saddle, respectively.

delay minimum remains.

Figure 2.4 shows the image locations and the arrival time delay contours as the source moves from within the astroid caustic across a cusp in a direction that is roughly along the semimajor axis of the lens distribution. As the source approaches the cusp, three of the images (A, B, and C in this case) come together. Two images (A and B) are outside and one image (C) is inside the critical curve. When the source is on the cusp, the three images become one on the critical curve. Finally, when the source moves across the cusp, one image remains outside the critical curve. (We label the remaining image by the one that comes alphabetically first among the three merging images.) The time delay contours in the right-hand panels depict this

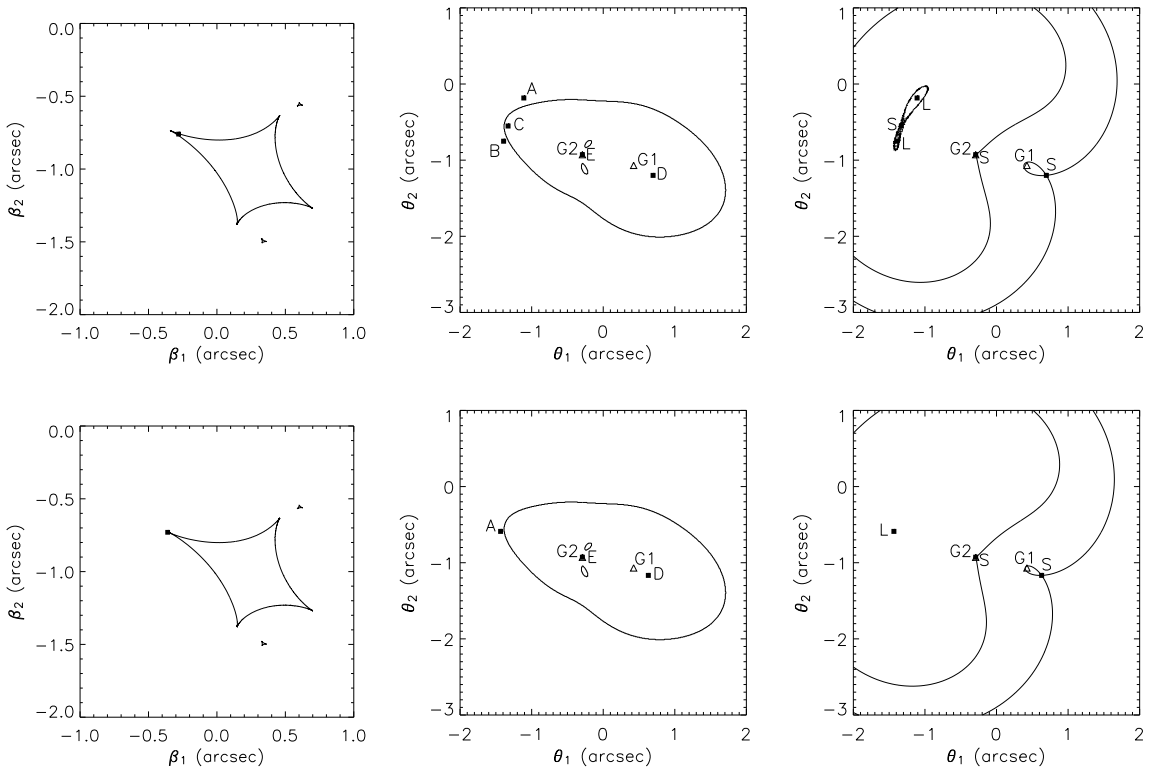

Figure 2.4: Left-hand panels: source position displaced across a cusp approximately along the semimajor axis from inside (top) to outside (bottom) of the astroid caustic curve of B1608+656 SPLE1+D (isotropic) model. Middle panels: image positions (A, B, C, D, and E) corresponding to the source positions shown in the left-hand panels, lens galaxy positions (G1 and G2) indicated by open triangles, and the critical curves. Right-hand panels: corresponding time delay contours. Letter L (for low) or S at each image location represents a time delay minimum or saddle, respectively.

behavior: the time delay saddle of a lemniscate merges simultaneously with both of its two minima and leaves a single minimum in the end.

Figure 2.5 is similar to figure 2.4 but with the source displacing toward a cusp that is roughly along the semiminor axis of lens distribution. The three merging images now have one image (B) outside and two images (C and D) inside the critical curve (shown in middle panels). In terms of the time delay contours (right-hand panels), this corresponds to the simultaneous merging of the saddle of the lemniscate with one of its minima and with the saddle of the enclosing limaçon (heart-shaped contour), leaving only the limaçon saddle in the end.

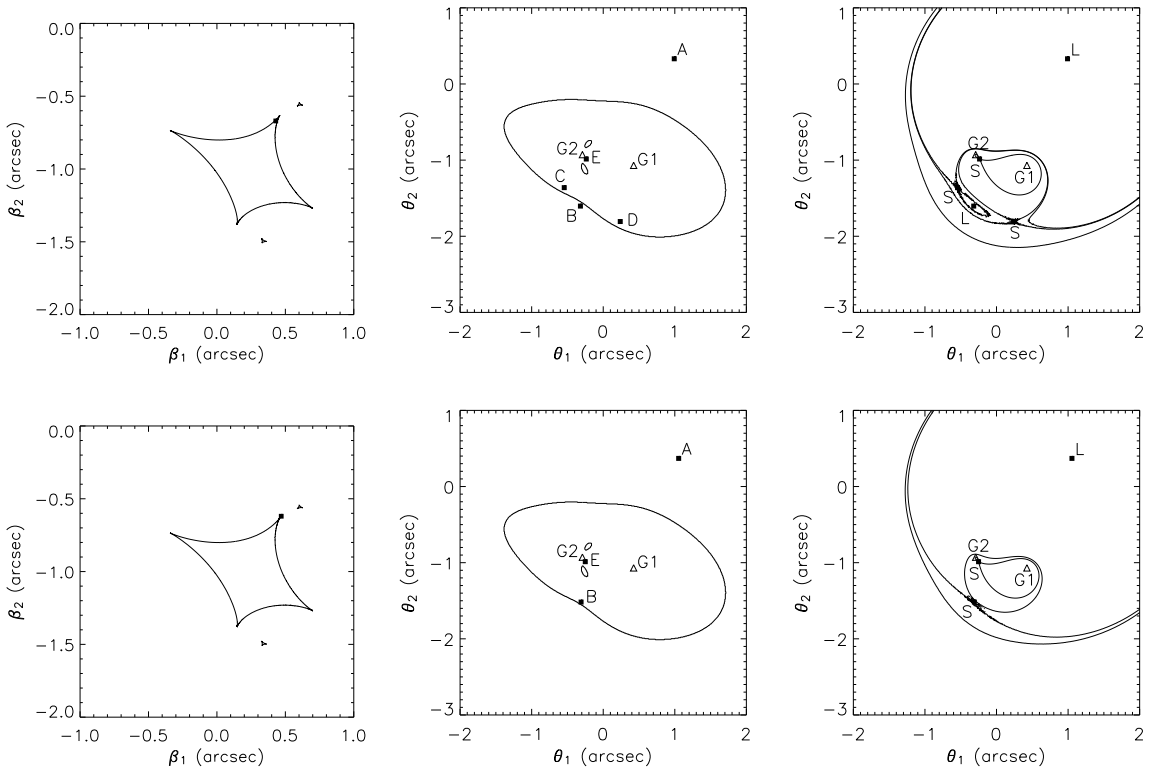

Figure 2.5: Left-hand panels: source position displaced across a cusp approximately along the semiminor axis from inside (top) to outside (bottom) of the astroid caustic curve of B1608+656 SPLE1+D (isotropic) model. Middle panels: image positions (A, B, C, D, and E) corresponding to the source positions shown in the left-hand panels, lens galaxy positions (G1 and G2) indicated by open triangles, and the critical curves. Right-hand panels: corresponding time delay contours. Letter L (for low) or S at each image location represents a time delay minimum or saddle, respectively.

2.2.3 Inner and Outer Limits

The movements of the image locations shown in figures 2.2 to 2.5 allow us to define *limit curves* (Blandford & Narayan 1986). Consider moving a hypothetical point source on the caustic curve. As the source traces around the folds of the caustic, the two nonmerging images trace out the limit curves. For the astroid, the nonmerging image inside the critical curve is on the *inner limit* and the image outside the critical curve is on the *outer limit*. For the deltoids, both nonmerging images are outside the corresponding critical curves. The deltoids thus have only outer limits composed of two images and no inner limits. Figure 2.6 is the plot of the limit curves for the SPLE1+D (isotropic) model in Koopmans et al. (2003b). The inner limit and outer limit for the astroid are shown in green and orange, respectively. The outer limit for the deltoids are shown in cyan.

We focus only on the limit curves of the astroid since they are typical for elliptical lens mass distributions. Both the inner and the outer limits are tangent to the critical curve twice, corresponding to source placement at the cusps of the caustic. The limit curves mark the boundary of the region containing four images.

2.2.4 Isophotal Separatrices

An isophote is an intensity contour. For simplicity, we assume the source intensity distribution has a single maximum with nested, noncrossing contours. We defer the discussion of more general intensity contours to the end of this section. Under the assumption of noncrossing isophotes, an *isophotal separatrix* on the image plane corresponds to a source intensity contour that is tangent to the caustic curve. The isophotes must cross at the critical curve and be tangent to the limit curves as we explain below.

Consider an extended elliptical source intensity distribution centered at $(\beta_{s1}, \beta_{s2}) = (0.088, -1.069)$ with an axis ratio of 0.634 and a semimajor axis position angle of 22.1 degrees.[4] The left-hand panel in figure 2.7 shows four colored intensity contours of

[4]This source model differs from the Koopmans et al. (2003b) source model in the position angle,

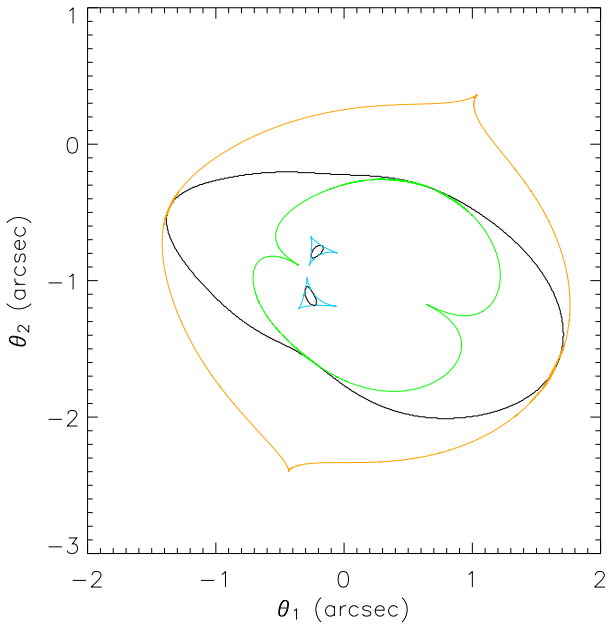

Figure 2.6: The limit curves are plotted with the critical curves (in black) for the SPLE1+D (isotropic) model of B1608+656. The orange (green) curve is the outer (inner) limit associated with the astroid. The limit curves are each tangent to the critical curve of the astroid twice. The cyan curves are the outer limits of the deltoids.

the extended source. The two intermediate isophotes are very close together (light blue and dark blue). The right-hand panel in figure 2.7 shows the mapped isophotes (same colors) with the critical curves (black) and limit curves (red). Each colored set of isophotes must intersect at the critical curve and be tangent to the inner and outer limit. This is shown most clearly by the purple isophotes that consist of a lemniscate (separatrix) with two elliptical satellite isophotes on the image plane. The lemniscate isophote must cross at the critical curve, and the two satellite isophotes must each be tangent to either the inner or the outer limit.

To explain the crossing and tangency conditions, let us consider the purple isophotes in detail. The crossing point of the lemniscate on the critical curve corresponds to the tangency point of the source isophote to the astroid caustic curve. Recall from section 2.2.2 that two of the four images of a hypothetical point source merge on the critical curve as the source moves across the fold from within. Therefore, a segment of the source isophote to either side of the caustic tangency point will map to two segments on the image plane, one inside and one outside the critical curve, that connect at the critical curve. The entire source isophote that is within the caustic will thus correspond to a lemniscate crossing the critical curve on the image plane with one lobe inside and one lobe outside the critical curve. The tangencies of the image isophotes to the limit curves can be understood based on the definition of limit curves, which are the inner and outer boundaries of the four-image region that are marked by the two nonmerging images as a hypothetical source traces around the caustic. The two satellite isophotes correspond to image isophotes traced by the two nonmerging images that must touch the inner and outer limits when the source isophote is tangent to the caustic. Since the inner and outer limits are the four-image boundaries, the touchings of the satellite isophotes to the limit curves become tangencies. Similar reasoning applies to the crossings and tangencies of the other three sets of isophotes.

So far we have restricted ourselves to simple nested, noncrossing source intensity contours. Nonetheless, we can easily generalize the crossing and tangency conditions above. Even with isophotes that are crossing on the source plane, there are still

but the difference is irrelevant for the purpose of describing isophotal separatrices.

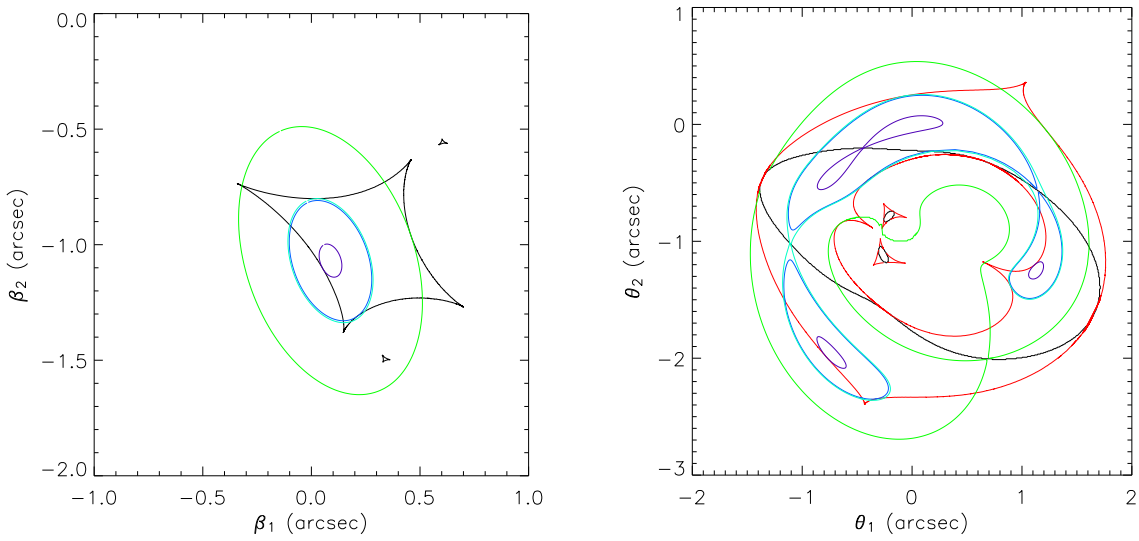

Figure 2.7: Left-hand panel: four isophotes (in colors) of an extended source intensity distribution that are tangent to the astroid caustic curve (black). Right-hand panel: the mapping of the isophotes in the left-hand panel with the critical curve (black) and limit curves (red). These isophotes must cross at the critical curve and their satellite isophotes must be tangent to the limit curves.

isophotes that are tangent to the caustic curve. When the tangent isophotes are mapped to the image plane, these mapped isophotes will again cross on the critical curve and be tangent to the limit curves. However, there will also be isophotal separatrices on the image plane that correspond to the crossing isophotes, if any, on the source plane. These will not necessarily cross on the critical curve as the crossing isophotes on the source plane need not be tangent to the caustic curve. Therefore, for a general source intensity distribution which has crossing isophotes (e.g., source with double nucleus), only *some* of the isophotal separatrices on the image plane need to cross on the critical curve with their corresponding satellite isophotes be tangent to the limit curves.

The crossing of the isophotes at the critical curves and the tangency of the isophotes to the limit curves provide qualitative tests on how good a lens model is. We will apply this test to B1608+656 in section 7.2.

Chapter 3

Bayesian Inference

In this chapter, we review the basics of Bayesian analysis, which provides the underpinning of this thesis. We follow MacKay (1992) for the theory of Bayesian analysis, but use different notation that is more convenient for the application to source intensity reconstruction in gravitational lensing in chapter 4. The material in this chapter was published in Suyu et al. (2006).

In Bayesian analysis, there are two levels of inference for data modeling. In the first level of inference, we choose a model and fit it to the data. This means characterizing the probability distribution for the parameters of the model given the data. In the second level of inference, we want to rank the models quantitatively in the light of the data. By asking for the relative probabilities of models given the data, Bayesian analysis incorporates Occam's razor (which states that overly complex models should not be preferred over simpler models unless the data support them) in this second level of inference. The appearance of Occam's razor will be evident at the end of section 3.2.1. In the following sections, we will describe the two levels of inference in detail.

3.1 Model Fitting

Let $\boldsymbol{d}$ be a vector of data points d_j, where $j = 1, \ldots, N_\mathrm{d}$ and N_d is the total number of data points. Let s_i be the model parameters that we want to infer given the data, where $i = 1, \ldots, N_\mathrm{s}$ and N_s is the number of parameters. Let $\mathbf{f}$ represent the response

function that relates the model parameters to the predicted data. (In the application of source reconstruction in gravitational lensing in chapter 4, $\mathbf{f}$ encodes information on the lens potential, which is fixed in each iteration of source reconstruction.) For simplicity, consider $\mathbf{f}$ to be a constant linear transformation matrix of dimensions $N_{\rm d}$-by-$N_{\rm s}$ such that

$$\boldsymbol{d} = \mathbf{f}\boldsymbol{s} + \boldsymbol{n}, \tag{3.1}$$

where $\boldsymbol{n}$ is the noise in the data characterized by the covariance matrix $\mathbf{C}_{\rm D}$ (here and below, subscript D indicates "data").[1]

Modeling the noise as Gaussian,[2] the probability of the data given the model parameters $\boldsymbol{s}$ is

$$P(\boldsymbol{d}|\boldsymbol{s},\mathbf{f}) = \frac{\exp(-E_{\rm D}(\boldsymbol{d}|\boldsymbol{s},\mathbf{f}))}{Z_{\rm D}}, \tag{3.2}$$

where

$$\begin{aligned} E_{\rm D}(\boldsymbol{d}|\boldsymbol{s},\mathbf{f}) &= \frac{1}{2}\left(\mathbf{f}\boldsymbol{s}-\boldsymbol{d}\right)^{\rm T}\mathbf{C}_{\rm D}^{-1}\left(\mathbf{f}\boldsymbol{s}-\boldsymbol{d}\right) \\ &= \frac{1}{2}\chi^2, \end{aligned} \tag{3.3}$$

and $Z_{\rm D} = (2\pi)^{N_{\rm d}/2}(\det \mathbf{C}_{\rm D})^{1/2}$ is the normalization for the probability. The probability $P(\boldsymbol{d}|\boldsymbol{s},\mathbf{f})$ as a function of the parameters $\boldsymbol{s}$ is called the *likelihood*, and $E_{\rm D}(\boldsymbol{d}|\boldsymbol{s},\mathbf{f})$ is half the usual χ^2 statistic. In many cases, the problem of finding the most likely solution $\boldsymbol{s}_{\rm ML}$ that minimizes $E_{\rm D}$ is illposed. This indicates the need to set a *prior* $P(\boldsymbol{s}|\mathbf{g},\lambda)$ on the parameters $\boldsymbol{s}$. The prior can be thought of as "regularizing" the parameters $\boldsymbol{s}$ to make the prediction $\mathbf{f}\boldsymbol{s}$ smooth. We can express the prior in the following form

[1] In this chapter, we consider Bayesian inference in linear problems. Nonetheless, the analysis in this chapter is completely general for both lensing and non-lensing work.

[2] The Gaussian assumption is usually applicable to optical CCD data because the number of counts per pixels is $\gg 10$, so that Gaussian approximation to Poisson noise is a very good one. The noise at each pixel is characterized by dispersion σ_j, which is the square root of the corresponding diagonal entry of the covariance matrix. In general, there is correlation between adjacent pixels due to charge transfer (bleeding) and the drizzling process, which is characterized by the off-diagonal terms in the covariance matrix.

$$P(\boldsymbol{s}|\mathbf{g},\lambda) = \frac{\exp(-\lambda E_{\rm S}(\boldsymbol{s}|\mathbf{g}))}{Z_{\rm S}(\lambda)}, \tag{3.4}$$

where λ, the so-called regularization constant, is the strength of regularization, $\mathbf{g}$ denotes the type of regularization, and $Z_{\rm S}(\lambda) = \int {\rm d}^{N_{\rm s}}\boldsymbol{s}\exp(-\lambda E_{\rm S})$ is the normalization of the prior probability distribution. The function $E_{\rm S}$ is often called the regularizing function. We focus on commonly used quadratic forms of the regularizing function, and defer the discussion of other priors to section 3.2.2. As we will see in section 3.2.1, Bayesian analysis allows us to infer quantitatively the value of λ from the data in the second level of inference.

Bayes' rule tells us that the *posterior probability* of the parameters $\boldsymbol{s}$ given the data, response function and prior is

$$\overbrace{P(\boldsymbol{s}|\boldsymbol{d},\lambda,\mathbf{f},\mathbf{g})}^{\text{posterior}} = \frac{\overbrace{P(\boldsymbol{d}|\boldsymbol{s},\mathbf{f})}^{\text{likelihood}}\overbrace{P(\boldsymbol{s}|\mathbf{g},\lambda)}^{\text{prior}}}{\underbrace{P(\boldsymbol{d}|\lambda,\mathbf{f},\mathbf{g})}_{\text{evidence}}}, \tag{3.5}$$

where $P(\boldsymbol{d}|\lambda,\mathbf{f},\mathbf{g})$ is the normalization that is called the *evidence* for the model $\{\lambda,\mathbf{f},\mathbf{g}\}$. Since both the likelihood and prior are either approximated or set as Gaussians, the posterior probability distribution is also a Gaussian. The evidence is irrelevant in the first level of inference where we maximize the posterior (equation (3.5)) of parameters $\boldsymbol{s}$ to obtain the most probable parameters $\boldsymbol{s}_{\rm MP}$. However, the evidence is important in the second level of inference for model comparisons. Examples of using the evidence in astronomical context are Hobson, Bridle, & Lahav (2002), Marshall et al. (2002), Marshall (2006) and Limousin et al. (2006).

To simplify the notation, let us define

$$M(\boldsymbol{s}) = E_{\rm D}(\boldsymbol{s}) + \lambda E_{\rm S}(\boldsymbol{s}). \tag{3.6}$$

With the above definition, we can write the posterior as

$$P(\boldsymbol{s}|\boldsymbol{d},\lambda,\mathbf{f},\mathbf{g}) = \frac{\exp(-M(\boldsymbol{s}))}{Z_{\rm M}(\lambda)}, \tag{3.7}$$

where $Z_{\rm M}(\lambda) = \int \mathrm{d}^{N_{\rm s}}\boldsymbol{s}\exp(-M(\boldsymbol{s}))$ is the normalization.

The Most Likely versus the Most Probable Solution

By definition, the most likely solution $\boldsymbol{s}_{\rm ML}$ maximizes the likelihood, whereas the most probable solution $\boldsymbol{s}_{\rm MP}$ maximizes the posterior. In other words, $\boldsymbol{s}_{\rm ML}$ minimizes $E_{\rm D}$ in equation (3.3) ($\nabla E_{\rm D}(\boldsymbol{s}_{\rm ML}) = \mathbf{0}$, where $\nabla \equiv \frac{\partial}{\partial \boldsymbol{s}}$) and $\boldsymbol{s}_{\rm MP}$ minimizes M in equation (3.6) ($\nabla M(\boldsymbol{s}_{\rm MP}) = \mathbf{0}$).

Using the definition of the most likely solution, it is not difficult to verify by doing the derivatives that it is

$$\boldsymbol{s}_{\rm ML} = \mathbf{F}^{-1}\boldsymbol{D}, \tag{3.8}$$

where

$$\mathbf{F} = \mathbf{f}^{\rm T}\mathbf{C}_{\rm D}^{-1}\mathbf{f}, \tag{3.9}$$

and

$$\boldsymbol{D} = \mathbf{f}^{\rm T}\mathbf{C}_{\rm D}^{-1}\boldsymbol{d}. \tag{3.10}$$

The matrix $\mathbf{F}$ is square with dimensions $N_{\rm s} \times N_{\rm s}$ and the vector $\boldsymbol{D}$ has dimensions $N_{\rm s}$.

In certain situations, the most probable solution $\boldsymbol{s}_{\rm MP}$ can in fact be obtained directly from the most likely solution $\boldsymbol{s}_{\rm ML}$. If the regularizing function $E_{\rm S}$ is a quadratic functional that obtains its minimum at $\boldsymbol{s}_{\rm reg}$ (i.e., $\nabla E_{\rm S}(\boldsymbol{s}_{\rm reg}) = \mathbf{0}$), then we can Taylor expand $E_{\rm D}$ and $E_{\rm S}$ to

$$E_{\rm D}(\boldsymbol{s}) = E_{\rm D}(\boldsymbol{s}_{\rm ML}) + \frac{1}{2}(\boldsymbol{s}-\boldsymbol{s}_{\rm ML})^{\rm T}\mathbf{B}(\boldsymbol{s}-\boldsymbol{s}_{\rm ML}), \tag{3.11}$$

and

$$E_{\rm S}(\boldsymbol{s}) = E_{\rm S}(\boldsymbol{s}_{\rm reg}) + \frac{1}{2}(\boldsymbol{s}-\boldsymbol{s}_{\rm reg})^{\rm T}\mathbf{C}(\boldsymbol{s}-\boldsymbol{s}_{\rm reg}), \tag{3.12}$$

where $\mathbf{B}$ and $\mathbf{C}$ are the Hessians of $E_{\rm D}$ and $E_{\rm S}$, respectively: $\mathbf{B} = \nabla\nabla E_{\rm D}(\boldsymbol{s})$ and $\mathbf{C} = \nabla\nabla E_{\rm S}(\boldsymbol{s})$. Equations (3.11) and (3.12) are exact for quadratic forms of $E_{\rm D}$ and $E_{\rm S}$ with the Hessians $\mathbf{B}$ and $\mathbf{C}$ as constant matrices. For the form of $E_{\rm D}$ in equation (3.3), $\mathbf{B}$ is equal to $\mathbf{F}$ that is given by equation (3.9). We define $\mathbf{A}$ as the Hessian of M, i.e., $\mathbf{A} = \nabla\nabla M(\boldsymbol{s})$, and by equation (3.6), $\mathbf{A} = \mathbf{B} + \lambda\mathbf{C}$. Using equations (3.6), (3.11), and (3.12) in $\nabla M(\boldsymbol{s}_{\rm MP}) = \mathbf{0}$, we can get the most probable solution (that maximizes the posterior) as $\boldsymbol{s}_{\rm MP} = \mathbf{A}^{-1}(\mathbf{B}\boldsymbol{s}_{\rm ML} + \lambda\mathbf{C}\boldsymbol{s}_{\rm reg})$. The simplest forms of the prior, especially the ones we will use for the gravitational lensing inversion in chapter 4, have $\boldsymbol{s}_{\rm reg} = \mathbf{0}$. In the case where $\boldsymbol{s}$ correspond to pixel intensity values, $\boldsymbol{s}_{\rm reg} = \mathbf{0}$ implies a prior preference toward a blank image. The noise suppression effect of the regularization follows from this supplied bias. Focusing on such forms of prior, the most probable solution becomes

$$\boldsymbol{s}_{\rm MP} = \mathbf{A}^{-1}\mathbf{B}\boldsymbol{s}_{\rm ML}. \tag{3.13}$$

This result agrees with equation (12) in Warren & Dye (2003). In fact, equation (3.13) is always valid when the regularizing function can be written as $E_{\rm S}(\boldsymbol{s}) = \frac{1}{2}\boldsymbol{s}^{\rm T}\mathbf{C}\boldsymbol{s}$.

Equation (3.13) indicates a one-time calculation of $\boldsymbol{s}_{\rm ML}$ via equation (3.8) that permits the computation of the most probable solution $\boldsymbol{s}_{\rm MP}$ by finding the optimal regularization constant of a given form of regularization. The parameters $\boldsymbol{s}_{\rm MP}$ in equation (3.13) depend on the regularization constant λ since the Hessian $\mathbf{A}$ depends on λ. Bayesian analysis provides a method for setting the value of λ, as described in the next subsection.

3.2 Model Comparison

In the previous section, we found that for a given set of data $\boldsymbol{d}$ and a model (response function $\mathbf{f}$ and regularization $\mathbf{g}$ with regularization constant λ), we could calculate the most probable solution $\boldsymbol{s}_{\rm MP}$ for the particular λ. In this section, we consider two main points: (i) how to set the regularization constant λ for a given form of regularization

g and (ii) how to rank the different models **f** and **g**.

3.2.1 Finding λ

To find the optimal regularization constant λ, we want to maximize

$$P(\lambda|\boldsymbol{d},\mathbf{f},\mathbf{g}) = \frac{P(\boldsymbol{d}|\lambda,\mathbf{f},\mathbf{g})P(\lambda)}{P(\boldsymbol{d}|\mathbf{f},\mathbf{g})}. \tag{3.14}$$

Assuming a flat prior in $\log\lambda$,[3] the evidence $P(\boldsymbol{d}|\lambda,\mathbf{f},\mathbf{g})$ which appeared in equation (3.5) is the quantity to consider for optimizing λ.

Combining and rearranging equations (3.2), (3.4), (3.5), (3.6), and (3.7), we get

$$P(\boldsymbol{d}|\lambda,\mathbf{f},\mathbf{g}) = \frac{Z_{\mathrm{M}}(\lambda)}{Z_{\mathrm{D}}Z_{\mathrm{S}}(\lambda)}. \tag{3.15}$$

For quadratic functional forms of $E_{\mathrm{S}}(\boldsymbol{s})$ with $\boldsymbol{s}_{\mathrm{reg}} = \mathbf{0}$, we have

$$Z_{\mathrm{S}}(\lambda) = e^{-\lambda E_{\mathrm{S}}(\mathbf{0})}\left(\frac{2\pi}{\lambda}\right)^{N_{\mathrm{s}}/2}(\det\mathbf{C})^{-1/2}, \tag{3.16}$$

$$Z_{\mathrm{M}}(\lambda) = e^{-M(\boldsymbol{s}_{\mathrm{MP}})}(2\pi)^{N_{\mathrm{s}}/2}(\det\mathbf{A})^{-1/2}, \tag{3.17}$$

and recall

$$Z_{\mathrm{D}} = (2\pi)^{N_{\mathrm{d}}/2}(\det\mathbf{C}_{\mathrm{D}})^{1/2}. \tag{3.18}$$

Remembering that optimizing a function is equivalent to optimizing the logarithm of that function, we will work with $\log P(\boldsymbol{d}|\lambda,\mathbf{f},\mathbf{g})$ to simplify some of the terms. Recalling that $\boldsymbol{s}_{\mathrm{reg}} = \mathbf{0}$, by combining and simplifying equations (3.15) to (3.18), we

[3] We use a flat prior that is uniform in $\log\lambda$ instead of λ because we do not know the order of magnitude of λ a priori.

have

$$\begin{aligned}\log P(\boldsymbol{d}|\lambda,\mathbf{f},\mathbf{g}) &= -\lambda E_{\rm S}(\boldsymbol{s}_{\rm MP}) - E_{\rm D}(\boldsymbol{s}_{\rm MP}) \\ &\quad -\frac{1}{2}\log(\det\mathbf{A}) + \frac{N_{\rm s}}{2}\log\lambda + \lambda E_{\rm S}(\mathbf{0}) \\ &\quad +\frac{1}{2}\log(\det\mathbf{C}) - \frac{N_{\rm d}}{2}\log(2\pi) \\ &\quad +\frac{1}{2}\log(\det\mathbf{C}_{\rm D}^{-1}). \end{aligned} \tag{3.19}$$

In deriving equation (3.19) using equation (3.16), we implicitly assumed that $\mathbf{C}$, the Hessian of $E_{\rm S}$, is nonsingular. The forms of regularization we will use for gravitational lensing inversion in chapter 4 have nonsingular Hessians so that equation (3.19) is applicable. For the cases in which the Hessian is singular (i.e., at least one of the eigenvalues of the Hessian is zero), the prior probability distribution is uniform along the eigendirections of the Hessian with zero eigenvalues. The prior probability distribution will need to be renormalized in the construction of the log evidence expression. The resulting log evidence expression can still be used to determine the optimal λ in these cases because only the relative probability is important and this normalizing factor of the uniform prior, though infinite, will cancel in the ratios of probabilities.

Solving $\frac{\rm d}{{\rm d}\log\lambda}\log P(\boldsymbol{d}|\lambda,\mathbf{f},\mathbf{g}) = 0$, we get the following equation for the optimal regularization constant $\hat{\lambda}$:

$$2\hat{\lambda}E_{\rm S}(\boldsymbol{s}_{\rm MP}) = N_{\rm s} - \hat{\lambda}{\rm Tr}(\mathbf{A}^{-1}\mathbf{C}), \tag{3.20}$$

where Tr denotes the trace. Since $\boldsymbol{s}_{\rm MP}$ and $\mathbf{A}$ depend on λ, the above equation (3.20) is often nonlinear and needs to be solved numerically for $\hat{\lambda}$.

For the reader's convenience, we reproduce the explanation in MacKay (1992) of equation (3.20). The equation is analogous to the (perhaps) familiar statement that χ^2 should roughly equal the number of degrees of freedom. Focusing on the usual case where $E_{\rm S}(\boldsymbol{s}_{\rm reg} = \mathbf{0}) = \mathbf{0}$ and transforming to the basis in which the Hessian of $E_{\rm S}$ is the identity (i.e., $\mathbf{C} = \mathbf{I}$), the left-hand side of equation (3.20) becomes $2\lambda E_{\rm S}(\boldsymbol{s}_{\rm MP}) = \lambda\boldsymbol{s}_{\rm MP}^T\boldsymbol{s}_{\rm MP}$. This quantity can be thought of as the "$\chi^2_{\rm S}$ of the

parameters" if we associate λ with the width ($\sigma_{\rm S}$) of the Gaussian prior in equation (3.4): $\lambda = 1/\sigma_{\rm S}^2$. The left-hand side of equation (3.20) can be viewed as a measure of the amount of structure introduced by the data in the parameter distribution (relative to the null distribution of $\boldsymbol{s}_{\rm reg} = \mathbf{0}$). Continuing the analogy, the right-hand side of equation (3.20) is a measure of the number of "good" parameters (where "good" here means well-determined by the data, as we explain below). In the same basis where $\mathbf{C} = \mathbf{I}$, we can write the eigenvalues of $\mathbf{A}(= \mathbf{B} + \lambda\mathbf{C})$ as $\mu_i + \lambda$, where μ_i are the eigenvalues of $\mathbf{B}$ and index $i = 1, \ldots, N_{\rm s}$. In this basis, the right-hand side, which we denote by γ, becomes

$$\gamma = N_{\rm s} - \sum_{i=1}^{N_{\rm s}} \frac{\lambda}{\mu_i + \lambda} = \sum_{i=1}^{N_{\rm s}} \frac{\mu_i}{\mu_i + \lambda}. \tag{3.21}$$

For each eigenvalue of $\mathbf{B}$, the fraction $\frac{\mu_i}{\mu_i+\lambda}$ is a value between 0 and 1, so γ is a value between 0 and $N_{\rm s}$. If μ_i is much smaller than λ, then the data are not sensitive to changes in the parameters along the direction of the eigenvector of μ_i. This direction contributes little to the value of γ with $\frac{\mu_i}{\mu_i+\lambda} \ll 1$, and thus it does not constitute as a good parameter. Similar arguments show that eigendirections with eigenvalues much greater than λ form good parameters. Therefore γ, which is a sum of all the factors $\frac{\mu_i}{\mu_i+\lambda}$, is a measure of the effective number of parameters constrained by the data. Thus, the solution to equation (3.20) is the optimal λ that matches the $\chi_{\rm S}^2$ of the parameters to the number of effective parameters.

For a given form of regularization $E_{\rm S}(\boldsymbol{s})$, we are letting the data decide on the optimal λ by solving equation (3.20). Occam's razor is implicit in this evidence optimization. Recall Occam's razor states that overly complex models should not be preferred over simpler models unless the data support them. For an overly small value of λ, the model parameter space is overly large and Occam's razor penalizes such an overly powerful model; for an overly large value of λ, the model parameter space is restricted to a limited region that the model can no longer fit to the data. Somewhere in between the two extremes is the optimal λ that gives a model which fits to the data without being overly complex.

There is a shortcut to obtaining an approximate value of the optimal λ instead of solving equation (3.20) (Bridle et al. 1998). Given that γ is a measure of the effective number of parameters, the classical number of degrees of freedom (NDF) should be $N_\mathrm{d} - \gamma$. At the optimal λ, we thus expect $E_\mathrm{D}(\boldsymbol{s}_\mathrm{MP}) = \frac{1}{2}\chi^2 \sim \frac{1}{2}(N_\mathrm{d} - \gamma)$. Inserting this and the expression of $\lambda E_\mathrm{S}(\boldsymbol{s}_\mathrm{MP})$ from equation (3.20) into equation (3.6), we find that $M(\boldsymbol{s}_\mathrm{MP}) \sim \frac{1}{2}N_\mathrm{d}$. In other words, one can choose the value of λ such that M evaluated at the resulting most probable parameters ($\boldsymbol{s}_\mathrm{MP}$) is equal to half the number of data points. We emphasize that this will give only an approximate result for the optimal λ due to the fuzzy association of NDF with $N_\mathrm{d} - \gamma$, but it may serve as a useful hack.

3.2.2 Ranking Models

We can compare the different regularizations $\mathbf{g}$ and responses $\mathbf{f}$ by examining the posterior probability of $\mathbf{g}$ and $\mathbf{f}$:

$$P(\mathbf{f}, \mathbf{g}|\boldsymbol{d}) \propto P(\boldsymbol{d}|\mathbf{f}, \mathbf{g})P(\mathbf{f}, \mathbf{g}). \tag{3.22}$$

If the prior $P(\mathbf{f}, \mathbf{g})$ is flat, i.e., all schemes for $\mathbf{f}$ and $\mathbf{g}$ are equally probable, then $P(\boldsymbol{d}|\mathbf{f}, \mathbf{g})$ can be used to rank the different models and regularizations. We can write $P(\boldsymbol{d}|\mathbf{f}, \mathbf{g})$ as

$$P(\boldsymbol{d}|\mathbf{f}, \mathbf{g}) = \int P(\boldsymbol{d}|\mathbf{f}, \mathbf{g}, \lambda)P(\lambda)\mathrm{d}\lambda, \tag{3.23}$$

where $P(\boldsymbol{d}|\mathbf{f}, \mathbf{g}, \lambda)$ is precisely the evidence in equation (3.19).

As seen in equation (3.23) above, the regularization constant λ is a nuisance parameter which invariably ends up being marginalized over. We might well expect the corresponding distribution for λ to be sharply peaked, since we expect the value of λ to be estimable from the data (as shown in section 3.2.1); a particular value of λ is preferred as a consequence of the balance between goodness of fit and Occam's razor. Consequently, we can approximate $P(\lambda|\boldsymbol{d}, \mathbf{f}, \mathbf{g})$ by a delta function centered on the most probable constant, $\hat{\lambda}$. The model-ranking evidence $P(\boldsymbol{d}|\mathbf{f}, \mathbf{g})$ in equation

(3.23) can then be approximated by $P(\boldsymbol{d}|\mathbf{f}, \mathbf{g}, \hat{\lambda})$ in equation (3.19).

The approximation of using equation (3.19) to rank regularzations is only valid if the Hessians of the different regularizing functions are nonsingular. When the Hessian is singular, equation (3.19) will need to be modified to include a (infinite) normalization constant that is regularization dependent. The constants for different regularization schemes generally will not cancel when one considers evidence ratios, thus prohibiting one from comparing different regularization schemes.

One can imagine there being much debate on the form of the prior $P(\mathbf{f}, \mathbf{g})$ that should be used. For example, some success has been achieved using maximum entropy methods (e.g., Gull & Daniell 1978; Skilling 1989), whose prior form enforces positivity in the image and is maximally noncommittal with regard to missing data. One practical problem with using the entropic prior is its nonlinearity. In this work we take a modern Bayesian view and argue that while we will always have some a priori prejudice about the reconstructed image (for example, favoring zero flux, or insisting on positive images), we would do well to try and learn from the data itself, assigning series of sensible priors and using the evidence to compare them quantitatively. In this context, we examine a small number of sensibly chosen priors (regularization schemes), and compute the evidence for each. We do not exhaustively seek the prior that maximizes the evidence, noting that this will change from object to object, and observation to observation. What we do provide is the mechanism by which prior forms can be compared, and demonstrate that good quality reconstructions can be obtained by optimizing over our set of candidate priors. In section 4.1, we discuss the various forms of prior that have been used in strong gravitational lensing.

We have presented in this chapter a technique based on Bayesian analysis for model fitting and model comparison. In the next chapter, we will apply this method to source intensity reconstruction in gravitational lensing.

Chapter 4

Pixelated Source Reconstruction

In the previous chapter, we have outlined Bayesian inference for data modeling and model comparison. In this chapter, we apply the Bayesian technique to source intensity reconstruction in strong gravitational lensing.

Lens systems with extended source brightness distributions are particularly useful since they provide additional constraints for the lens modeling due to surface brightness conservation. In such a system, one would need to fit simultaneously the source intensity distribution and the lens potential model (or, equivalently the lens mass distribution) to the observational data. The use of a pixelated source brightness distribution has the advantage over a parametric source brightness distribution in that the source model is not restricted to a particular parameter space. Warren & Dye (2003) introduced a linear inversion method to obtain the best-fitting pixelated source distribution given a lens model and the observational data. Several groups of people (e.g., Wallington et al. 1996; Treu & Koopmans 2004; Dye & Warren 2005; Koopmans 2005; Brewer & Lewis 2006; Suyu et al. 2006) have used pixelated source distributions.

The method of source inversion described in Warren & Dye (2003) requires the source distribution to be "regularized" (i.e., smoothness conditions on the inverted source intensities to be imposed) for reasonable source resolutions.[1] For fixed pixel

[1]The source pixel sizes are fixed and are roughly a factor of the average magnification smaller than the image pixel sizes. In this case, regularization is needed because the number of source pixels is comparable to the number of data pixels. On the other hand, if the number of source pixels is much fewer than the effective number of data pixels (taking into account of the signal-to-noise ratio), the data alone could be sufficient to constrain the pixelated source intensity values and

sizes, there are various forms of regularization to use, and the differences among them have not been addressed in detail prior to this work. In addition, associated with a given form of regularization is a regularization constant (signifying the strength of the regularization), and the way to set this constant has been unclear, again prior to this work. These were two long-standing problems noted in Kochanek et al. (2006). In the next section, Bayesian analysis (introduced in chapter 3) is used to address the above two issues by providing a quantitative method for comparing different values of the regularization constant and the forms of regularization.

Brewer & Lewis (2006) also followed a Bayesian approach for pixelated source inversions. The main difference between Brewer & Lewis (2006) and this work is the prior on the source intensity distribution. Furthermore, we quantitatively compare the various forms of regularization by using the Bayesian evidence for each of the forms of regularization; Brewer & Lewis (2006) mentioned the concept of model comparison but did not apply it.

Dye & Warren (2005) use adaptive source grids to avoid the use of explicit regularization (i.e., uniform priors are imposed since adapting the grids is an implicit form of regularization); however, the Bayesian formalism would still be useful to set the optimal scales of the adaptive pixel sizes objectively. Furthermore, regularized source inversions (as opposed to unregularized—see footnote 1) permit the use of smaller pixel sizes to obtain fine structures.

In this chapter, we apply the Bayesian formalism developed in chapter 3 to source inversions in strong gravitational lensing. For simplicity, let us suppose that the observed image consists only of the lensed source intensity distribution and noise in this chapter. This can be easily generalized to include dust and lens galaxy light (see section 6.1). The outline of the chapter is as follows. In section 4.1, we describe the Bayesian analysis of source inversions in gravitational lensing. Sections 4.2 and 4.3 are two examples illustrating regularized source inversions. In both examples, we use simulated data to demonstrate the Bayesian technique of quantitatively comparing the

regularization would play little role. This is equivalent to imposing a uniform prior on the source intensity distribution (recall from chapter 3, a prior on the source is a form of regularization).

different types of regularization. Finally, section 4.4 contains additional discussions based on the two examples. Most of the material in this chapter was published in Suyu et al. (2006).

4.1 Regularized Source Inversion

To describe the regularized source inversion problem, we follow Warren & Dye (2003) but in the Bayesian language. Let d_j, where $j = 1, \ldots, N_\mathrm{d}$, be the observed image intensity value at each pixel j and let $\mathbf{C}_\mathrm{D}$ be the covariance matrix associated with the image data. Let s_i, where $i = 1, \ldots, N_\mathrm{s}$, be the source intensity value at each pixel i that we would like to reconstruct. For a given lens potential and point spread function (PSF) model, we can construct the N_d-by-N_s matrix $\mathbf{f}$ that maps a source plane of unit intensity pixels to the image plane by using the lens equation (a practical and fast method to compute $\mathbf{f}$ is described in the appendices of Treu & Koopmans (2004), and an alternative method is discussed in Wallington et al. (1996)). We identify E_D with $\frac{1}{2}\chi^2$ (equation (3.3)) and E_S with the quadratic regularizing function. The definitions and notations in our regularized source inversion problem are thus identical to the Bayesian analysis in chapter 3 with data $\boldsymbol{d}$ and mapping matrix (response function) $\mathbf{f}$. Therefore, all equations in chapter 3 are immediately applicable to this source inversion problem, for example the most probable (regularized) source intensity is given by equation (3.13). We take as estimates of the 1 σ uncertainty on each pixel value the square root of the corresponding diagonal element of the source covariance matrix given by

$$\mathbf{C}_\mathrm{S} = \mathbf{A}^{-1}, \tag{4.1}$$

(here and below, subscript S indicates "source"), where $\mathbf{A}$ is the Hessian defined in section 3.1. Equation (4.1) differs from the source covariance matrix used by Warren & Dye (2003). We refer the reader to appendix B for details on the difference.

In summary, to find the most probable source given an image (data) $\boldsymbol{d}$, a lens and PSF model $\mathbf{f}$ and a form of regularization $\mathbf{g}$, the three steps are: (i) find the most

likely source intensity, $\boldsymbol{s}_{\rm ML}$ (the unregularized source inversion with $\lambda = 0$); (ii) solve equation (3.20) for the optimal λ of the particular form of regularization, where $\boldsymbol{s}_{\rm MP}$ is given by equation (3.13); (iii) use equations (3.13) and (4.1) to compute the most probable source intensity and its 1 σ error with the optimal λ from step (ii).

Having found a recipe to compute the optimal λ and the most probable inverted source intensity $\boldsymbol{s}_{\rm MP}$ for a given form of regularization $\mathbf{g}$ and a lens and PSF model $\mathbf{f}$, we can rank the different forms of regularization. For a given potential and PSF model $\mathbf{f}$, we can compare the different forms of regularization by assuming the prior on regularization $\mathbf{g}$ to be flat and using the evidence to evaluate $P(\mathbf{f}, \mathbf{g}|\boldsymbol{d})$ via equations (3.22), (3.23), and (3.19).

In this work, we consider three quadratic functional forms of regularization: zeroth-order, gradient, and curvature (see appendix A for details). These were used in Warren & Dye (2003) and Koopmans (2005). The zeroth-order regularization tries to suppress the noise in the reconstructed source brightness distribution as a way to impose smoothness by minimizing the source intensity at each pixel. The gradient regularization tries to minimize the gradient of the source distribution, which is equivalent to minimizing the difference in the source intensities between adjacent pixels. Finally, the curvature regularization minimizes the curvature in the source brightness distribution. The two examples in the following subsections apply the three forms of regularization to the inversion of simulated data to demonstrate the Bayesian regularized source inversion technique.

Our choice of using quadratic functional forms of the prior is encouraged by the resulting linearity in the inversion. The linearity permits fast computation of the maximization of the posterior without the risk of being trapped in a local maximum during the optimization process. However, the quadratic functional forms may not be the most physically motivated. For example, positive and negative values of the source intensity pixels are equally preferred, even though we know that intensities must be positive. Wallington et al. (1996) and Wayth et al. (2005) used maximum entropy methods that enforced positivity on the source brightness distribution. Such forms of the prior would help confine the parameter space of the source distribution

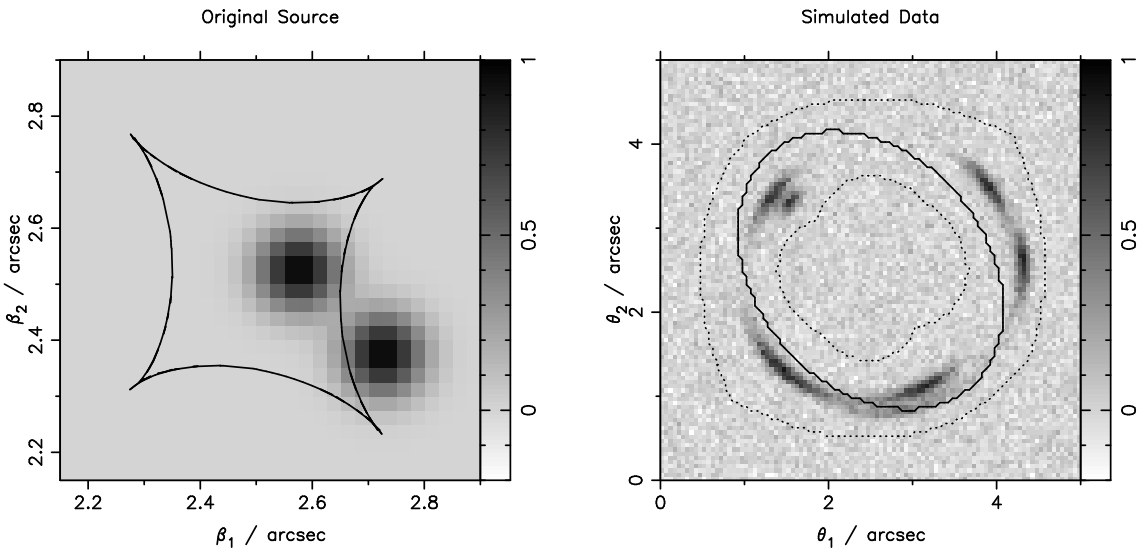

Figure 4.1: Left-hand panel: The simulated Gaussian sources with peak intensities of 1.0 and FWHM of 0.05″, shown with the astroid caustic curve of the SIE potential. Right-hand panel: The simulated image of the Gaussian sources (after convolution with Gaussian PSF and addition of noise, as described in the text). The solid line is the critical curve of the SIE potential, and the dotted lines mark the annular region where the source grid maps using the mapping matrix $\mathbf{f}$.

and result in a perhaps more acceptable reconstruction. The disadvantage of using the entropic prior is its resulting nonlinear inversion, though we emphasize that Bayesian analysis can still be applied to these situations to rank models. Another example is Brewer & Lewis (2006) who used priors suited for astronomical images that are mostly blank. This form of prior also led to a nonlinear system. In the following sections, we merely focus on quadratic forms of the prior because (i) it is computational efficiency, and (ii) we are able to obtain good quality reconstruction without considering more complex regularization schemes.

4.2 Demonstration 1: Gaussian Sources

4.2.1 Simulated Data

As the first example to demonstrate the Bayesian approach to source inversion, we use the same lens potential and source brightness distribution as that in Warren &

Dye (2003). The lens is a singular isothermal ellipsoid (SIE) at a redshift of $z_{\rm d} = 0.3$ with velocity dispersion of 260 $\mathrm{km\,s^{-1}}$, axis ratio of 0.75, and semimajor axis position angle of 40 degrees (from vertical in counterclockwise direction). We use Kormann, Schneider, & Bartelmann (1994) for the SIE model. The image pixels are square and have sizes $0.05''$ in each direction. We use 100×100 image pixels ($N_{\rm d} = 10{,}000$) in the simulated data.

We model the source as having two identical Gaussians with variance $0.05''$ and peak intensity of 1.0 in arbitrary units. The source redshift is $z_{\rm s} = 3.0$. We set the source pixels to be half the size of the image pixels ($0.025''$) and have 30×30 source pixels ($N_{\rm s} = 900$). Figure 4.1 shows the source in the left-hand panel with the caustic curve of the SIE potential. One of the Gaussians is located within the astroid caustic and the other is centered outside the caustic.

To obtain the simulated data, we use the SIE lens model and the lens equation to map the source intensity to the image plane. We then convolve the resulting image with a Gaussian PSF whose FWHM is $0.08''$ and add uniform Gaussian noise of variance 0.067 to the convolved image. For simplicity, the noise is uncorrelated, which is a good approximation to realistic noise with minimal charge transfer and drizzling. The right-hand panel of figure 4.1 shows the simulated data with the critical curve of the SIE model.

4.2.2 Most Likely Inverted Source

We use the original SIE potential, PSF and Gaussian noise models of the simulated data for the source inversion to demonstrate the technique.

The appendices of Treu & Koopmans (2004) describe a computationally efficient method to construct the $\mathbf{f}$ matrix. Following the method, we discretize the SIE potential to the 100×100 grid and model the PSF on a 5×5 grid (which is a sufficient size since the 5×5 grid centered on the Gaussian PSF of FWHM 0.08" contains 99.99% of the total intensity). Subsequently, for every image pixel j, we use the lens equation to trace to the source plane labeled by pixels i and interpolate to

get the elements of unblurred $\mathbf{f}$. Lastly, we multiply the unblurred $\mathbf{f}$ by the blurring (convolution) operator constructed from the 5×5 PSF model to get the full $\mathbf{f}$ matrix. With $j = 1, \ldots, N_{\rm d}$ and $i = 1, \ldots, N_{\rm s}$, the matrix $\mathbf{f}$ is large (10,000 $\times$ 900) but fortunately sparse.

In the right-hand panel of figure 4.1, the dotted lines on the simulated data mark an annular region where the image pixels map to the finite source plane. In other words, the image pixels within the dotted annulus correspond to the nonempty rows of the $\mathbf{f}$ matrix. The annular region thus marks the set of data that will be used for the source inversion process.

With the $\mathbf{f}$ matrix and the data of simulated image intensities in the annulus, we can construct matrix $\mathbf{F}$ and vector $\boldsymbol{D}$ using equations (3.9) and (3.10)[2] for the unregularized inversion (the most likely source intensity, in Bayesian language). We use UMFPACK[3] for sparse matrix inversions and determinant calculations. We compute the inverse of the matrix $\mathbf{F}$ and apply equation (3.8) to get the most likely source intensity. Using UMFPACK, the computation time for the inversion of $\mathbf{F}$, a 900×900 matrix in this example, is only $\sim$20 seconds on a 3.6 GHz CPU. Setting $\lambda = 0$ (implicit in $\mathbf{A}$) in equation (4.1), we obtain the covariance matrix of the inverted source intensity and hence the 1 σ error and the signal-to-noise ratio.

The top row of figure 4.2 shows the unregularized inverted source intensity in the left-hand panel, the 1 σ error of the intensity in the middle panel, and the ratio of these two in the right-hand panel. The unregularized inverted source intensity is smoother inside than outside the caustic curve because the source pixels within the caustic have additional constraints due to higher image multiplicities. The higher image multiplicities also explain the lower magnitude of the 1 σ error inside the caustic curve. Despite the noisy reconstruction especially outside the caustic curve, the two Gaussian sources have significant signal to noise in the right-hand panel. These results agree with Figure 2 in Warren & Dye (2003).

The bottom row of figure 4.2 shows the simulated data in the left-hand panel

[2]The summations associated with the matrix multiplications in equations (3.9) and (3.10) are now summed over the pixels in the annulus instead of all the pixels on the image plane.

[3]a sparse matrix package developed by Timothy A. Davis, University of Florida

(from figure 4.1 for comparison purposes), the reconstructed data (from the most likely inverted source in the top left-hand panel and the $\mathbf{f}$ matrix) in the middle panel, and the residual (the difference between the simulated and reconstructed data) in the right-hand panel. The annular region containing the data used for inversion is marked by dotted lines in the reconstructed and residual images. Visual inspection of the residual image shows that pixels inside the annulus are slightly less noisy than those outside. This is due to overfitting with the unregularized inversion. As we will see in the next subsection, Occam's razor that is incorporated in the Bayesian analysis will penalize such overly powerful models.

4.2.3 Most Probable Inverted Source

Having obtained the most likely inverted source, we can calculate the most probable source of a given form of regularization with a given value of the regularization constant λ using equation (3.13). In the remainder of this section, we focus on the three forms of regularization (zeroth order, gradient, and curvature) discussed in appendix A. For each form of regularization, we numerically solve equation (3.20) for the optimal value of regularization constant λ using equation (3.13) for the values of $\boldsymbol{s}_{\mathrm{MP}}$. Table 4.1 shows the optimal regularization constant, $\hat{\lambda}$, for each of the three forms of regularization. The table also includes the value of the evidence in equation (3.19) evaluated at $\hat{\lambda}$, which is needed for ranking the different forms of regularization in the next subsection.

Figure 4.3 verifies the optimization results for the gradient form of regularization. The evidence in dot-dashed lines (rescaled) is indeed a sharply peaked function of λ, justifying the delta-function approximation; the optimal regularization constant $\hat{\lambda} = 34.2$ (listed in table 4.1) is marked by the crossing point of the dashed and dotted lines, demonstrating the balance between goodness of fit and simplicity of model that maximizing the evidence achieves. The plots of equations (3.20) and (3.19) for zeroth-order and curvature regularizations look similar to figure 4.3 and are thus not shown.

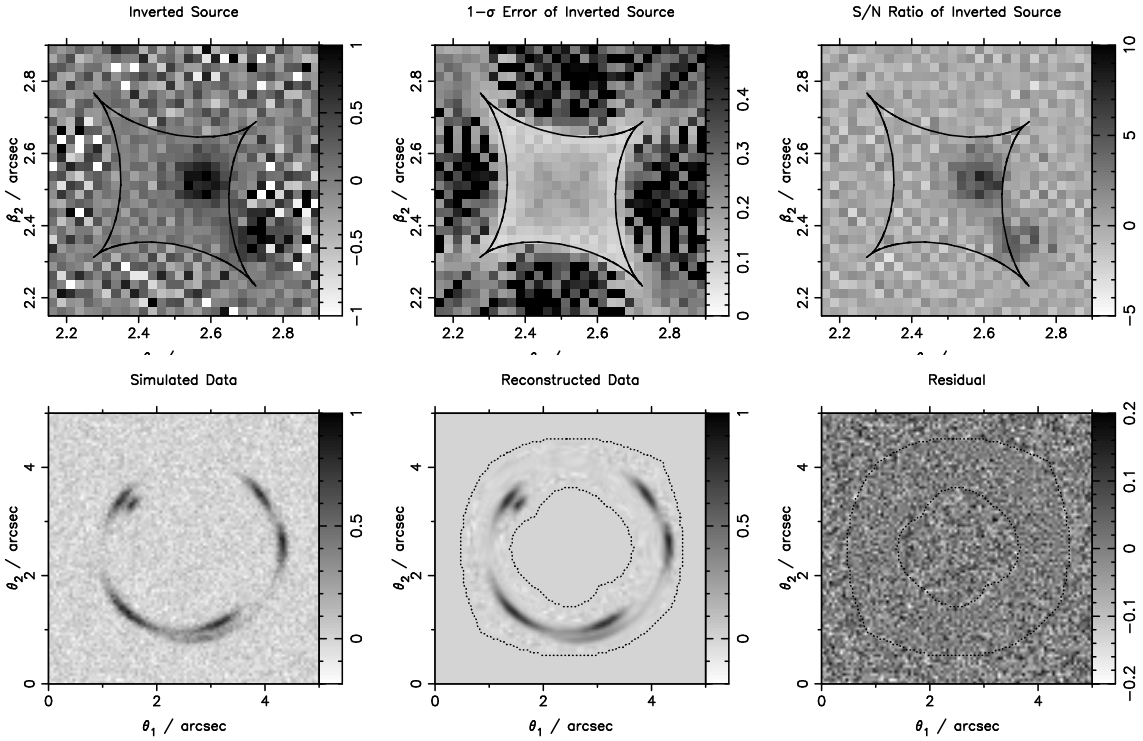

Figure 4.2: Unregularized inversion of Gaussian sources. Top left-hand panel: the most likely reconstructed source intensity distribution. The intensities outside the caustic curve of the potential model are not well reconstructed due to fewer constraints (lower image multiplicities) outside the caustic curve. Top middle panel: the 1 σ error of the inverted source intensity. The error is smaller inside the caustics due to additional multiple image constraints. Top right-hand panel: the signal-to-noise ratio of the inverted source intensity. The presence of the Gaussian sources is clear in this panel even though the reconstruction in the top left-hand panel is noisy. Bottom left-hand panel: the simulated data. Bottom middle panel: the reconstructed image using the most likely reconstructed source (top left-hand panel) and the $\mathbf{f}$ matrix from the potential and PSF models. Reconstructed data are confined to an annular region that maps on to the source plane. Bottom right-hand panel: the residual image obtained by subtracting the bottom middle panel from the bottom left-hand panel. The interior of the annular region is less noisy than the exterior, indicating that the unregularized reconstructed source is fitting to the noise in the simulated data.

Table 4.1: The optimal regularization constant for each of the three forms of regularization for the inversion of two Gaussian sources

regularization	zeroth order	gradient	curvature
$\hat{\lambda}$	17.7	34.2	68.5
$\log P(\boldsymbol{d}\|\hat{\lambda}, \mathbf{f}, \mathbf{g})$	5086	5367	5410
$\gamma = N_{\rm s} - \hat{\lambda}{\rm Tr}(\mathbf{A}^{-1}\mathbf{C})$	536	287	177
$\chi^2 = 2E_{\rm D}$	3583	3856	4019
$N_{\rm annulus}$	4325	4325	4325
$\chi^2/N_{\rm annulus}$	0.83	0.89	0.93
$\chi^2/(N_{\rm annulus} - N_{\rm s})$	1.05	1.12	1.17
$\chi^2/(N_{\rm annulus} - \gamma)$	0.95	0.95	0.97

Note. — The log evidence, γ (the right-hand side of equation (3.20)), and the χ^2 evaluated at the optimal regularization constant are also listed. The number of data pixels in the annulus for inversion, $N_{\rm annulus}$, and three possible forms of constructing the reduced χ^2 are shown. The last row with the number of degrees of freedom equaling $N_{\rm annulus} - \gamma$ gives reduced χ^2 closest to 1. This supports our interpretation of γ as the number of "good" parameters determined by the data.

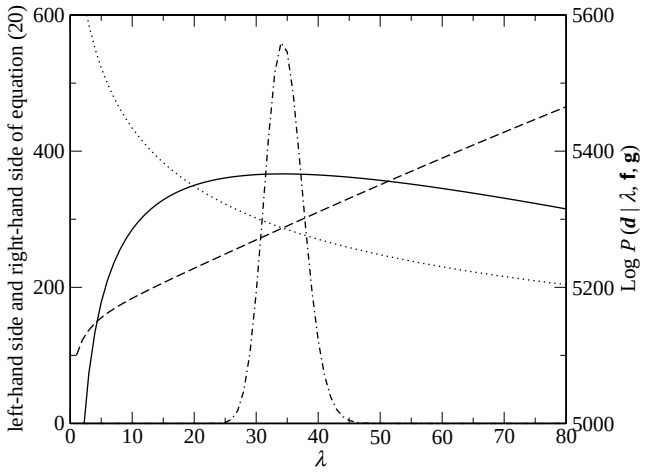

Figure 4.3: To demonstrate the λ optimization process, equations (3.19) and (3.20) are plotted as functions of λ for the gradient regularization. The left-hand side and right-hand side of equation (3.20) are in dashed lines and dotted lines, respectively. The log evidence in equation (3.19) is shown in solid lines. The evidence, which has been rescaled to fit on the graph, is in dot-dashed lines. The left and right vertical axes are for equation (3.20) and (3.19), respectively. The crossing point of the left-hand side and right-hand side of equation (3.20) gives the optimal $\hat{\lambda}$, the position where the log evidence (hence evidence) obtains its maximum.

In table 4.1, we constructed three reduced χ^2 using the number of degrees of freedom (NDF) as $N_{\rm annulus}$, $N_{\rm annulus} - N_{\rm s}$, or $N_{\rm annulus} - \gamma$, where $N_{\rm annulus}$ is the number of data pixels used in the inversion and recall $N_{\rm s}$ is the number of source pixels reconstructed. In each of the three forms of regularization, the reduced χ^2 with NDF $= N_{\rm annulus} - \gamma$ is closest to 1.0, which is the criterion commonly used to determine the goodness of fit. This supports our interpretation of the γ, the right-hand side of equation (3.20), as the number of "good" parameters determined by the data. The values of the reduced χ^2 is not strictly 1.0 because Bayesian analysis determines the optimal λ by maximizing the evidence instead of setting the reduced χ^2 to 1.0.

For each of the three forms of regularization and its optimal regularization constant listed in table 4.1, we use equations (3.13) and (4.1) to obtain the most probable source intensity and its 1 σ error. Figure 4.4 shows the most probable source intensity (left-hand panels), the 1 σ error (middle panels), and the signal-to-noise ratio (right-hand panels) for zeroth-order (top row), gradient (middle row) and curvature (bottom row) regularizations. The panels in each column are plotted on the same scales in order to compare the different forms of regularization. The regularized inverted sources in the left-hand panels clearly show the two Gaussians for all three regularizations. Curvature regularization results in a smoother source reconstruction than gradient regularization which in turn gives smoother source intensities than zeroth-order regularization. The 1 σ errors in the middle column also indicates the increase in the smoothness of the source from zeroth-order to gradient to curvature regularization due to a decrease in the error. This smoothness behavior agrees with the notion that regularizations associated with higher derivatives in general result in smoother source reconstructions. Since the error in the middle column decreases from the top to the bottom panel, the signal to noise of the source reconstruction increases in that order. Looking closely at the 1 σ error in the middle column for gradient and curvature regularizations, the pixels in the left and bottom borders have larger error values. This can be explained by the explicit forms of regularization in equations (A.2) and (A.3). The pixels at the bottom and left borders are only constrained by their values relative to their neighbors, whereas the pixels at the top and right

borders have additional constraints on their values directly (last two terms in the equations). Visually, we observe that the source reconstruction with curvature regularization matches the original source in figure 4.1 the best. In the next subsection, we will quantitatively justify that curvature regularization is preferred over gradient and zeroth-order regularizations in this example with two Gaussian sources.

In figure 4.5, we show the reconstructed image and the image residual for the most probable inverted source with curvature regularization. We omit the analogous figures for zeroth-order and gradient regularizations because they look very similar to figure 4.5. The left-hand panel is the simulated data in figure 4.1 that is shown for convenience for comparing to the reconstructed data. The middle panel is the reconstructed data obtained by multiplying the corresponding regularized inverted source in figure 4.4 by the $\mathbf{f}$ mapping matrix (only the pixels within the annulus [dotted lines] are reconstructed due to the finite source grid and PSF). The right-hand panel is the residual image, which is the difference between the simulated and the reconstructed data. The slight difference among the reconstructed data of the three forms of regularizations is the amount of noise. Since the most probable inverted source gets less noisy from zeroth-order to gradient to curvature regularization, the reconstructed data also gets less noisy in that order. The residual images of all three forms of regularization look almost identical and match the input (uniform Gaussian) noise, a sign of proper source reconstruction.

In contrast to the residual image for the unregularized case in figure 4.2, the noise in the residual image in figure 4.5 is more uniform. This is Occam's razor in action—the presence of regularization prevents the overfitting to the noise within the annulus. For each form of regularization, the value of $\hat{\lambda}$ (table 4.1) is optimal since it leads to the residual image in figure 4.5 having the input noise, which is uniform Gaussian noise in our example. If we overregularize (i.e., use overly large λ), then we expect the model to no longer fit to the data. This is shown in figure 4.6 which were obtained using curvature regularization with $\lambda = 2000$. The panels in the figure are displayed in the same way as in figure 4.2. The inverted source (top left-hand panel) in figure 4.6 shows the smearing of the two Gaussian sources due to overly

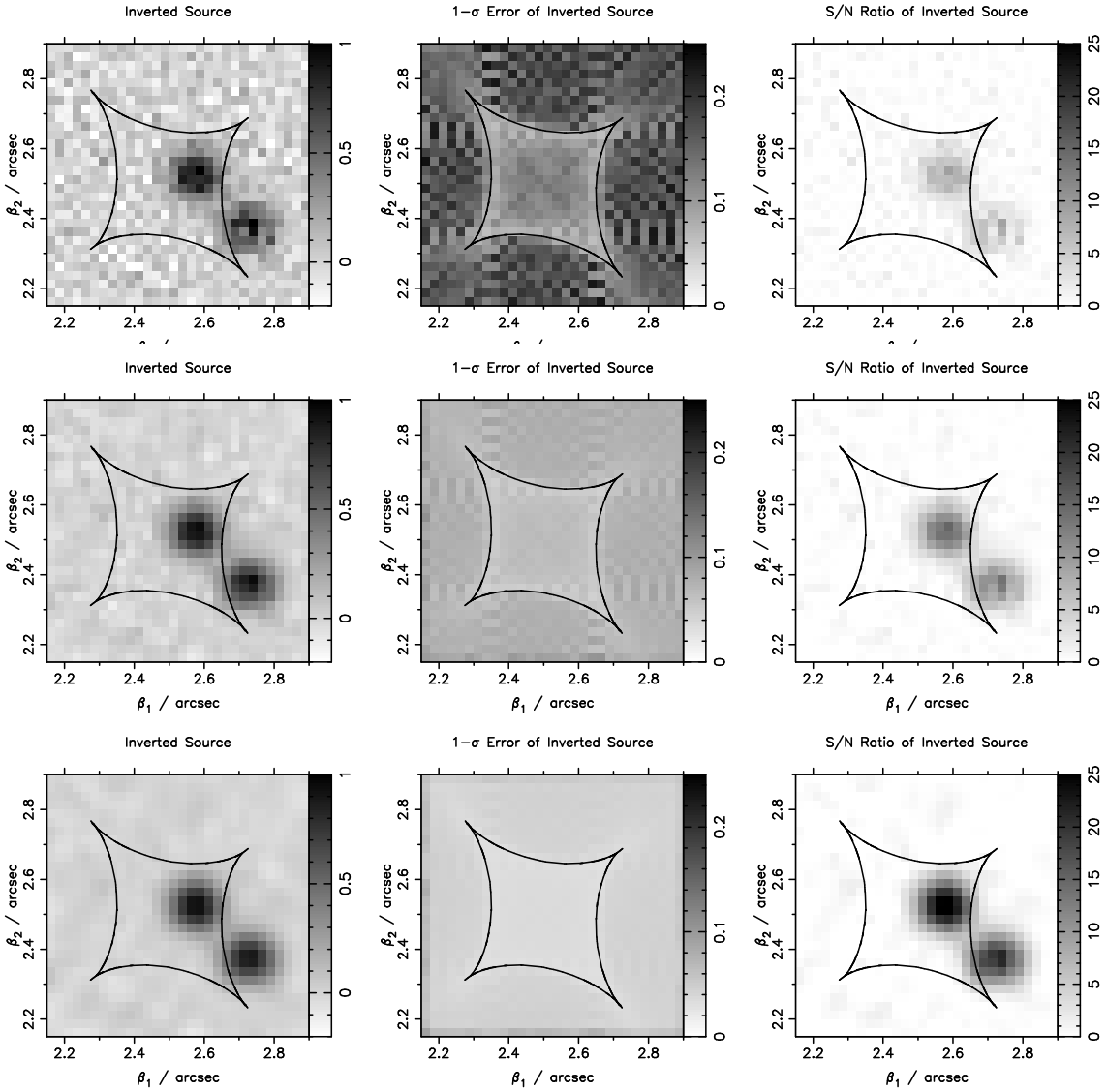

Figure 4.4: The regularized source inversions of Gaussian sources with zeroth-order, gradient and curvature regularizations. Top row, from left to right: most probable inverted source, the 1 σ error, and the signal-to-noise ratio with zeroth-order regularization. Middle row, from left to right: same as top row but with gradient regularization. Bottom row, from left to right: same as top row but with curvature regularization. The panels in each column are plotted on the same scales for comparison among the different forms of regularization.

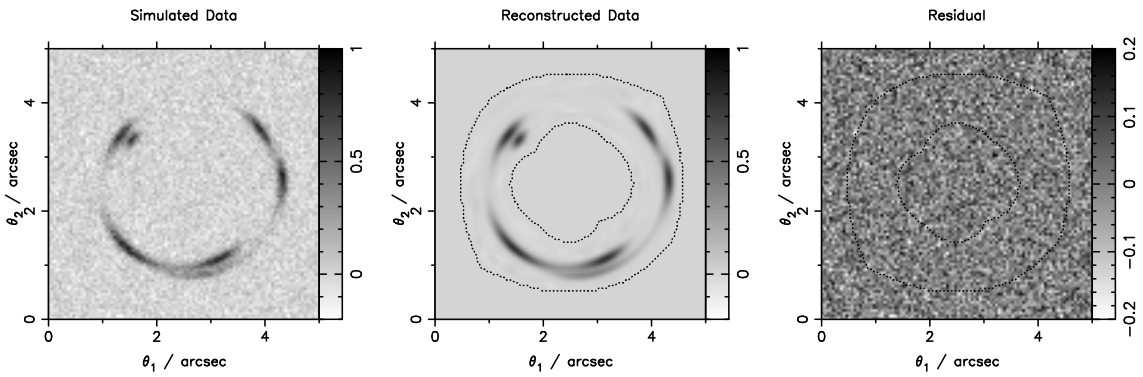

Figure 4.5: The image residual for curvature regularized source inversion with Gaussian sources. From left to right: simulated data, reconstructed data using the corresponding most probable inverted source in figure 4.4, and the residual equaling the difference between simulated and reconstructed data. The reconstructed data is restricted to the annulus marked by dotted lines that is mapped from the finite source grid using $\mathbf{f}$. The noise in the residual image is more uniform compared to that of the unregularized inversion in figure 4.2.

minimized curvature among adjacent pixels. The resulting residual image (bottom right-hand panel) in figure 4.6 thus shows arc features that are not fitted by the model. However, note that the inferred signal-to-noise ratio in the source plane is very high; models that overly regularize the source intensities give precise (with small magnitudes for the error) but inaccurate results. Such overly regularized models lead to low values of the evidence, which is the quantity to consider for the goodness of reconstruction. We seek an accurate reconstruction of the source, and a signal-to-noise ratio that accurately reflects the noise in the data. The comparison among the unregularized, optimally regularized and overly regularized inversions shows the power of the Bayesian approach to objectively determine the optimal $\hat{\lambda}$ (of a given form of regularization) that minimizes the residual without fitting to the noise. In the next subsection, we will see how Bayesian analysis can also be used to determine the preferred form of regularization given the selection of regularizations.

4.2.4 Optimal Form of Regularization

In the previous subsection, we showed how Bayesian analysis allowed us to determine objectively the optimal regularization constant for a given form of regularization by

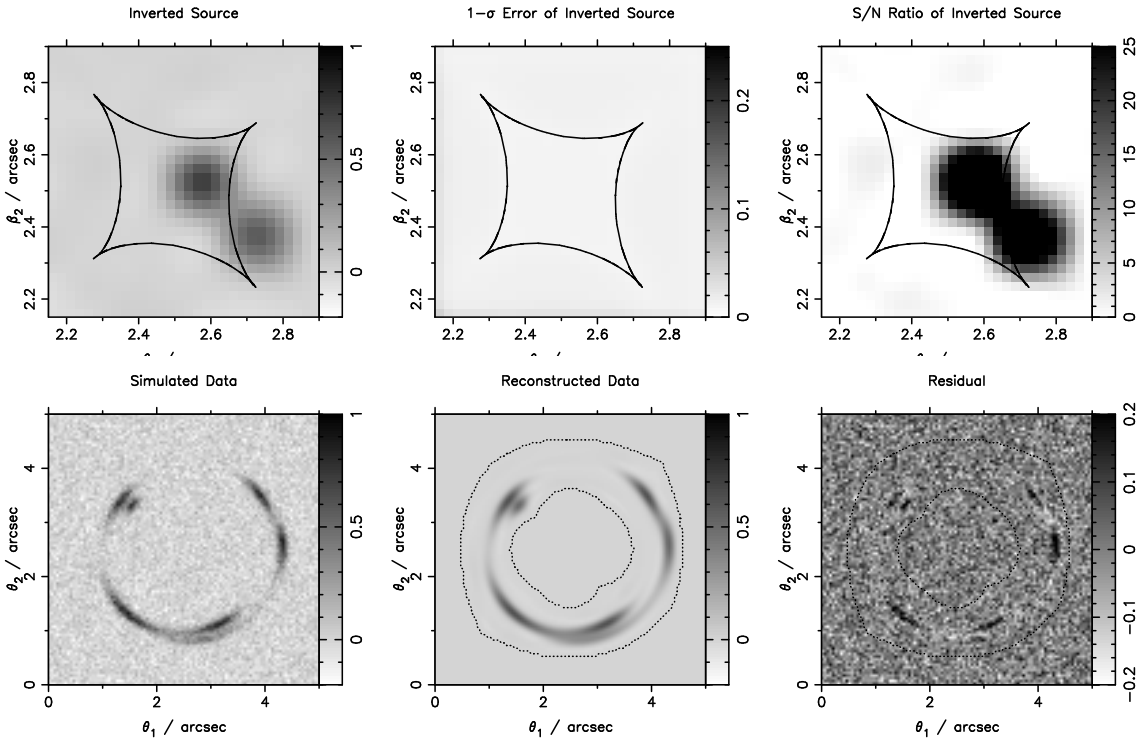

Figure 4.6: Overly regularized source inversion of Gaussian sources using curvature regularization with $\lambda = 2000$. Top row: the overly regularized source shows smearing of the original two Gaussians (left-hand panel), the 1 σ error of the source intensity (middle panel), and the signal-to-noise ratio (right-hand panel). Bottom row: simulated data (left-hand panel), reconstructed data using the reconstructed source in the top left-hand panel and the $\mathbf{f}$ mapping matrix (middle panel), and the image residual showing arc features due to the overly regularized inverted source (right-hand panel).

maximizing the evidence in equation (3.19). In this subsection we look for the optimal form of regularization given the selection of regularizations.

Since there is no obvious prior on the regularization, we assume that the prior on the regularization is flat. In this case, the different forms of regularization are ranked by the value of $P(\boldsymbol{d}|\mathbf{f},\mathbf{g})$ in equation (3.23). Since the evidence $P(\boldsymbol{d}|\mathbf{f},\mathbf{g},\lambda)$ is sharply peaked at $\hat{\lambda}$ (as seen in figure 4.3), $P(\boldsymbol{d}|\mathbf{f},\mathbf{g})$ can be approximated by $P(\boldsymbol{d}|\mathbf{f},\mathbf{g},\hat{\lambda})$. The values of the evidence $P(\boldsymbol{d}|\mathbf{f},\mathbf{g},\hat{\lambda})$ in table 4.1 indicate that the evidence for curvature regularization is $\sim e^{43}$ and $\sim e^{324}$ higher than that of gradient and zeroth-order regularizations, respectively. Therefore, curvature regularization with the highest evidence is preferred to zeroth order and gradient for the two Gaussian sources. In quantitative terms, curvature regularization is $\sim e^{43}$ more probable than gradient regularization, which is $\sim e^{281}$ more probable than zeroth-order regularization. This agrees with our comment based on figure 4.4 in section 4.2.3 that visually, curvature regularization leads to an inverted source that best matches the original source of two Gaussians.

The values of the reduced χ^2 using NDF $= N_{\text{annulus}} - \gamma$ in table 4.1 show that curvature regularization has the highest reduced χ^2 among the three forms of regularization. The higher χ^2 value means a higher misfit due to fewer degrees of freedom (with more correlated adjacent pixels) in curvature regularization. Nonetheless, the misfit is noise dominated since figure 4.5 shows uniform residual and the reduced χ^2 is $\sim$1.0. Therefore, the evidence optimization is selecting the simplest model of the three regularization schemes that fits to the data, encapsulating the spirit of Occam's razor.

For general source brightness distributions, one may expect that curvature regularization with its smoothing and simplification effects will always be preferred to the gradient and zeroth-order forms of regularization. We show that this is not the case by considering the source inversion of a box source (region of uniform intensity) and two point sources as our next example.

4.3 Demonstration 2: Box and Point Sources

4.3.1 Simulated Data

To generate the simulated data of the box and point sources, we keep the following things the same as those in the example of two Gaussian sources: number of source pixels, source pixel size, number of image pixels, image pixel size, SIE potential model, and PSF model. The variance of the uniform uncorrelated Gaussian noise for the box and point sources is 0.049, which leads to the same signal-to-noise ratio within the annular region as that in the two Gaussian sources. Figure 4.7 shows the box source and two point sources of unit intensities with the caustic curves of the SIE in the left-hand panel, and the simulated image in the right-hand panel.

We follow the same procedure as that in the previous example of two Gaussian sources to obtain the most likely inverted source, the most probable inverted source of a given form of regularization, and the optimal form of regularization. Furthermore, we plot the results in the same format as that in the example of two Gaussian sources in section 4.2.

4.3.2 Most Likely Inverted Source, Most Probable Inverted Source, and Optimal Form of Regularization

Figures 4.8 shows the most likely inverted source in the top row and the corresponding image residual in the bottom row. Similar to figure 4.2, the most likely inverted source in the top left-hand panel of figure 4.8 has poorly constrained pixels outside the caustic curves due to lower image multiplicities. The residual image in the bottom right-hand panel of figure 4.8 shows slight overfitting to the noise inside the annulus.

For regularized inversions, we solve equation (3.20) for the optimal regularization constant for each of the three forms of regularization. We list the optimal regularization constants, $\hat{\lambda}$, and the associated log evidence evaluated at $\hat{\lambda}$ in table 4.2. Figure 4.9 shows the most probable inverted source using the optimal regularization constant in table 4.2 for each of the three forms of regularization. By visual inspection, the

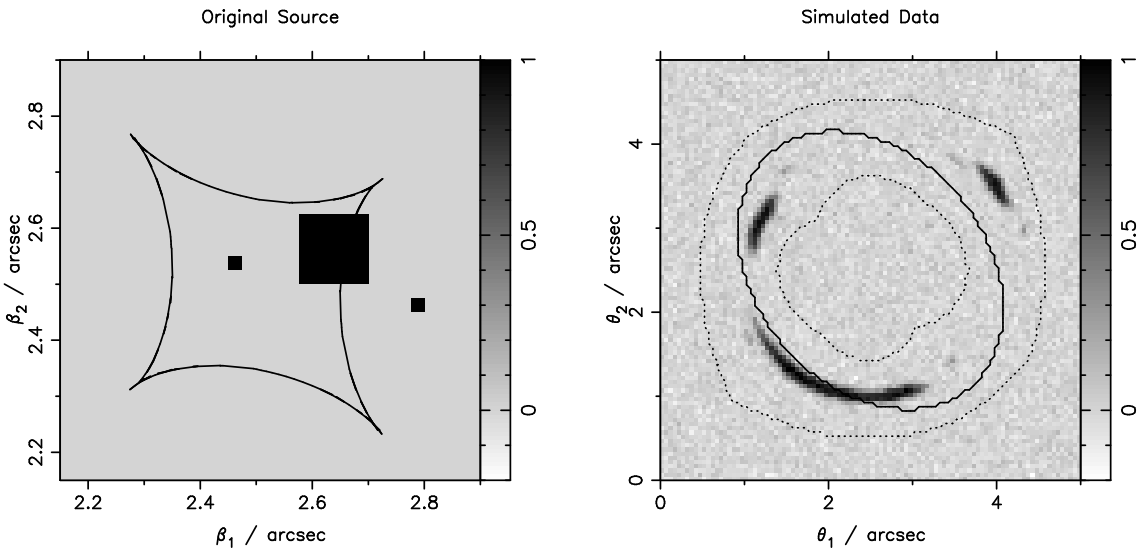

Figure 4.7: Left-hand panel: The simulated box and point sources with intensities of 1.0, shown with the astroid caustic curve of the SIE potential. Right-hand panel: The simulated image of the box and point sources (after convolution with Gaussian PSF and addition of noise as described in the text). The solid line is the critical curve of the SIE potential and the dotted lines mark the annular region where the source grid maps using the **f** mapping matrix.

inverted source intensities (left-hand panels) with gradient regularization matches the original source brightness distribution (figure 4.7) the best since curvature regularization overly smears the sharp edges and zeroth-order regularization leads to higher background noise. This is supported quantitatively by the values of the evidence in table 4.2 with the highest value for gradient regularization (which is $\sim e^{37}$ more probable than curvature regularization and $\sim e^{222}$ more probable than zeroth-order regularization). Again, this example illustrates that the signal-to-noise ratio does not determine the optimal regularization—the right-hand panels of figure 4.9 show that curvature regularization leads to the highest signal-to-noise ratio, but the Bayesian analysis objectively ranks gradient over curvature! Finally, figure 4.10 shows the reconstructed image (middle panel) and the image residual (right-hand panel) using the gradient regularization. The corresponding plots for the zeroth-order and curvature regularizations are similar and hence are not shown.

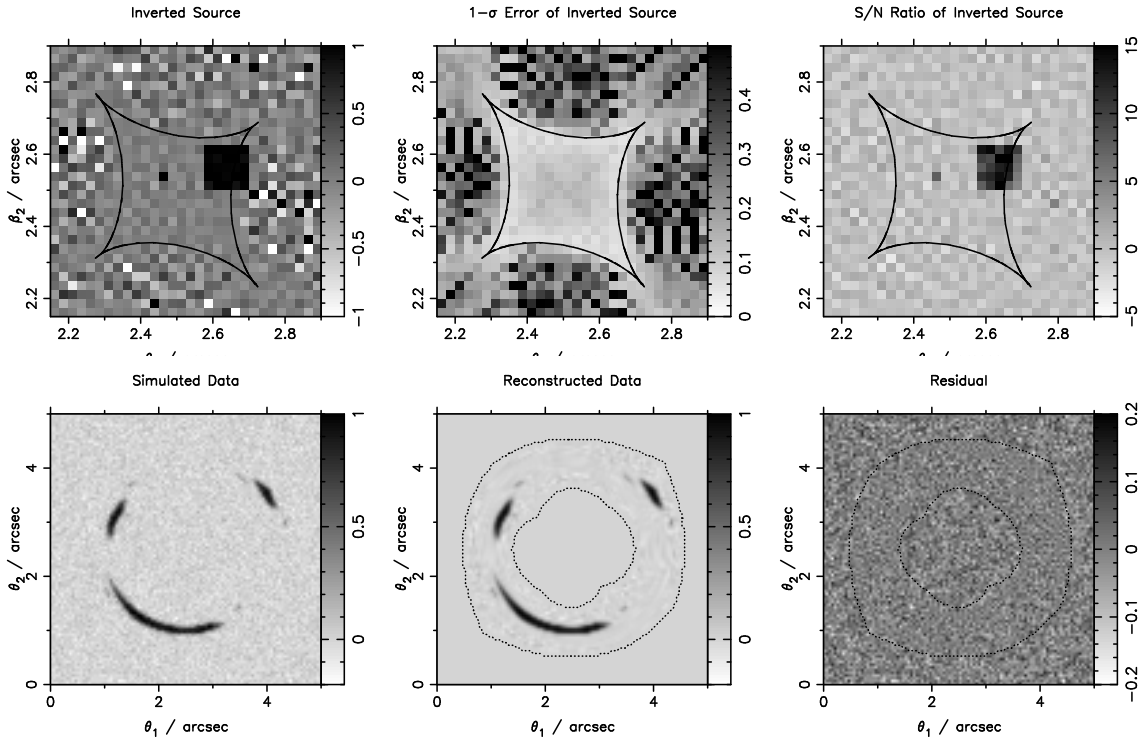

Figure 4.8: Unregularized source inversion of box and point sources. Top left-hand panel: the most likely reconstructed source intensity distribution. The intensities outside the caustic curve of the potential model are not well reconstructed due to fewer constraints (lower image multiplicities) outside the caustic curve. Top middle panel: the 1 σ error of the inverted source intensity. The error is smaller inside the caustics due additional multiple image constraints. Top right-hand panel: the signal-to-noise ratio of the inverted source intensity. Bottom left-hand panel: the simulated data. Bottom middle panel: the reconstructed image using the most likely reconstructed source (top left-hand panel) and the $\mathbf{f}$ matrix from the potential and PSF models. Reconstructed data is confined to an annular region that maps on to the source plane. Bottom right-hand panel: the residual image obtained by subtracting the bottom middle panel from the bottom left-hand panel. The interior of the annular region is less noisy than the exterior, indicating that the reconstructed image is fitting to the noise in the simulated data.

Table 4.2: The optimal regularization constant for each of the three forms of regularization for the inversion of box and point sources

Regularization	zeroth order	gradient	curvature
$\hat{\lambda}$	19.8	21.0	17.1
$\log P(\boldsymbol{d}\|\hat{\lambda}, \mathbf{f}, \mathbf{g})$	6298	6520	6483

Note. — The listed log evidence value is evaluated at the optimal regularization constant.

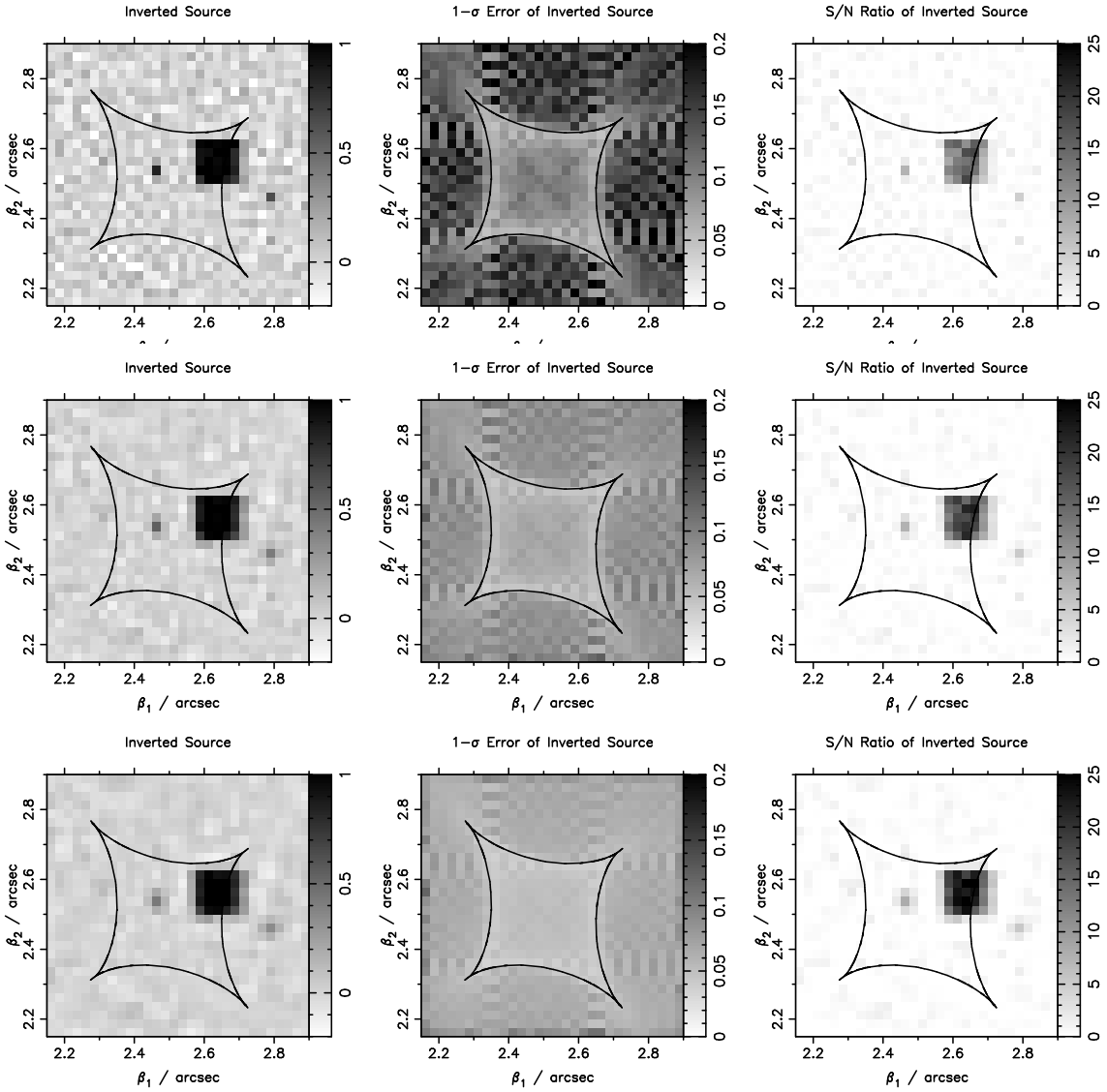

Figure 4.9: The regularized source inversions of box and point sources with zeroth-order, gradient and curvature regularizations. Top row, from left to right: most probable inverted source, the 1 σ error, and the signal-to-noise ratio with zeroth-order regularization. Middle row, from left to right: same as top row but with gradient regularization. Bottom row, from left to right: same as top row but with curvature regularization. The panels in each column are plotted on the same scales for comparison among the different forms of regularization.

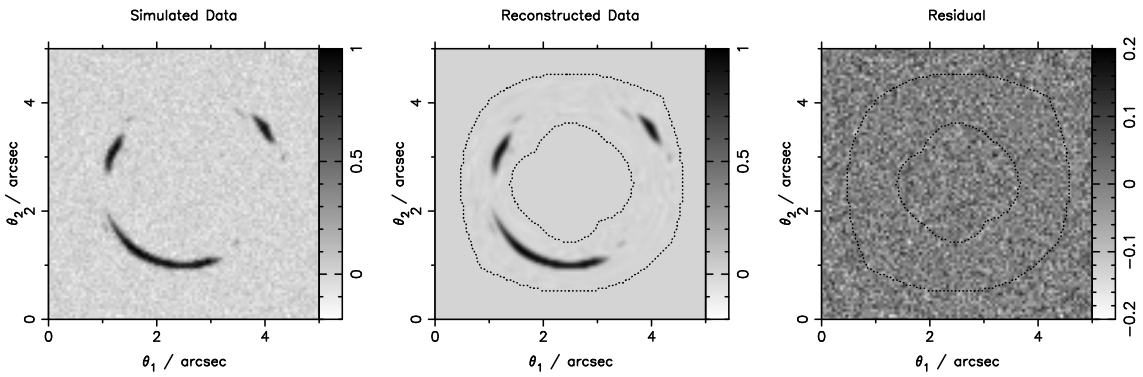

Figure 4.10: The image residual for gradient regularized source inversion with box and point sources. From left to right: simulated data, reconstructed data using the corresponding most probable inverted source in figure 4.9, and the residual equaling the difference between simulated and reconstructed data. The reconstructed data are restricted to the annulus marked by dotted lines that is mapped from the finite source grid using $\mathbf{f}$. The noise in the residual image is more uniform compared to that of the unregularized inversion in figure 4.8.

4.4 Discussion

4.4.1 Preferred Form of Regularization

The two examples of source inversion considered in sections 4.2 and 4.3 show that the form of regularization that is optimally selected in the Bayesian approach depends on the nature of the source. Generally, with the three forms of regularization considered, curvature regularization is preferred for smooth sources and gradient (or even zeroth order) is preferred for sources with sharp intensity variations. In the two examples of source inversion, we found that at least one of the three considered forms of regularization (which is not always the curvature form) allowed us to reconstruct successfully the original source in the inversion. Therefore, we did not need to consider other forms of regularization. Nonetheless, this does not preclude other forms of regularization to be used. Even with additional types of regularization, Bayesian analysis can always be used to choose the optimal one from the selection of forms of regularization.

4.4.2 Optimal Number of Source Pixels

So far, we have not discussed the size and the region of the source pixels to use. In both demonstration examples in sections 4.2 and 4.3, we used source pixels that were half the size of the image pixels. In reality, one has to find the source region and the size of source pixels to use.

The selection of the source pixel size for a given source region can be accomplished using Bayesian analysis in the model comparison step of section 3.2.2 (the size of the source pixels is part of $\mathbf{f}$ since different source pixels sizes result in different matrices $\mathbf{f}$). We find that source pixels sizes that are too large do not have enough degrees of freedom to fit to the data. On the other hand, source pixels that are too small will result in some source pixels being excluded in the $\mathbf{f}$ matrix (using the $\mathbf{f}$ construction method in Treu & Koopmans (2004)), which leads to a failure in the most likely source inversion since some pixels will be unconstrained. Therefore, for fixed pixel sizes over a source region (which our codes assume), the minimum source pixel size will be set by the minimum magnification over the source region. To improve the resolution in areas where there is more information, one would need to use adaptive grids. Dye & Warren (2005) have used adaptive grids in their source inversion routine, and we are also in the process of developing a code with adaptive gridding that will appear in a future paper. Our methods differ from that of Dye & Warren (2005) in that we follow a Bayesian approach and can thus quantitatively compare the forms of regularization and the structure of source pixelation.

At this stage, we cannot compare different source regions since the annular region on the image plane that maps to the source plane changes when the source region is altered. Recall that we only use the data within the annulus for source inversion. If the annular region changes, the data for inversion also change. For model comparison between different data sets, we would need to know the normalization in equation (3.22), which we do not. Therefore, the best we can do in terms of source region selection is to pick a region that is large enough to enclose the entire luminous source, but small enough to not have the corresponding annular region exceeding the image

region where we have data. Once the source region is selected, we can apply Bayesian analysis to determine the optimal source pixel size (subject to the minimum limit discussed above) and the optimal form of regularization given the data.

4.4.3 Weighting Regularization

Some gravitational lens systems, such as B1608+656, have a bright nucleus at the center of the extended source (which was not present in the case of the simulated data in the previous sections). The gradient and curvature types of regularizations may be inappropriate with the presence of the point source because these regularizations bias toward smooth source intensity distributions. With uniform regularization as the ones used in the previous sections, the central region near the point source would be overregularized whereas the outer regions would be underregularized. We remedy this by downweighting the regularization at each pixel by the intensity at that pixel. Specifically, we first reconstruct the source with uniform regularization weighting (the kind of regularizations use in the previous section) to get an estimate of the intensities, and we then use these intensities as weights for our weighted source intensity reconstruction. This has the effect of having a higher dynamical range for the source intensity reconstruction. While this does accentuate the dim extended background source intensity when tested on simulated data, the effect is small on the B1608+656 source reconstruction. In addition to accentuating the background source intensity, the weighted regularization also amplifies the noise. We find that this causes instabilities in the iterative and perturbative potential reconstruction method (described in chapter 7) that requires source reconstruction at each iteration. Therefore, when weighting the regularization in the source reconstruction, we do so only in the very last iteration as an option.

4.4.4 Usage of Source Inversion

In this thesis, we use the source reconstruction for two purposes:

(i) *Pixelated potential reconstruction.* As will be described in the chapter 7, the

iterative and perturbative potential correction scheme (Blandford et al. 2001) that we use requires values of the source intensity gradient at each iteration. Therefore, we reconstruct the source intensity following the method outlined and demonstrated in this chapter.

(ii) *Model comparison.* As described in chapter 3 and earlier in this chapter, we can use the Bayesian evidence values from the source reconstructions to compare the models **f** (which incorporate the PSF and lens potential) and **g**. In images of real lens systems, there are, in addition to the lensed source intensity distributions, light from the lens galaxies and dust extinction (in some cases like B1608+656). As will be shown in chapter 6, we can also use the Bayesian evidence from source inversion to compare different dust (if there is dust extinction in the lens system) and lens galaxy light models. The important thing is to keep the data set fixed for comparing these models (so that the normalization in equation (3.22) in section 3.2.2 remains the same for different models). Therefore, when we compare models, we mark an annular region enclosing the Einstein ring and use the same annulus of data for all models (where models refer collectively to the lens potential, PSF, dust, lens galaxies' light, and regularization). For the chosen data set, we determine the source region that maps to the annular region and reconstructs the source intensities in this region. The shape of this source region is generally not rectangular, so we generalize the regularization schemes in appendix A to patch the right-most and top-most pixels (pixels adjacent to the edge of grid or adjacent to the unmapped source pixels) with lower derivatives. The resulting Bayesian evidence values from the source reconstruction then allow us to compare the different models. We will use this model comparison technique in chapters 6 and 8 to compare various PSF, dust, lens galaxies' light and lens potential models for B1608+656.

Chapter 5

Observations of B1608+656

In this chapter, we describe observations of B1608+656 since its discovery as a gravitational lens.

5.1 Discovery VLA Observations and Ground-Based Optical and Infrared Follow-Ups

The gravitational lens B1608+656 was discovered in the Cosmic Lens All-Sky Survey (CLASS)[1] (Myers et al. 1995). It was observed using the Very Large Array (VLA) at a frequency of 8.4 GHz in A configuration on 1994 March 1 in the CLASS survey, and was discovered independently by Snellen et al. (1995) using VLA at 8.4 and 15 GHz in B configuration on 1994 July 23. The radio source had been detected prior to its identification as a gravitational lens system, and Table 1 in Snellen et al. (1995) lists the relevant radio observations between 1990 and 1994. Upon discovery, the lens system was subsequently followed up in the optical and infrared bands. The optical image was taken with the COSMIC camera in 1.5″ seeing on the Palomer Observatory 5 m telescope on 1994 August 9, and the 2.2 μm infrared image was obtained with the W. M. Keck 10 m telescope on 1994 August 22. A spectrum taken at Palomar Observatory on the same night as the optical image showed Mg II $\lambda\lambda 2796, 2803, \mathrm{H}\varepsilon, \mathrm{H}\delta$ absorption lines and the [O II] $\lambda 3727$ emission line, and gave a measurement for the redshift of the lens at $z_d = 0.6304$ (Myers et al. 1995). The strong Balmer absorption lines suggest

[1]CLASS is a large and systematic search for gravitational lenses in a sample of 14,000 flat-spectrum radio sources using the Very Large Array.

that the primary lens G1 has K+A poststarburst population (Dressler & Gunn 1983; Myers et al. 1995; Surpi & Blandford 2003; Koopmans et al. 2003b). The first spectrum of the source was obtained using the Low Resolution Imaging Spectrograph on the W. M. Keck 10 m Telescope on 1994 September 4; the source redshift could not be derived because no standard star exposure was taken with the same setup due to instrumental problems. Further optical spectra of the source were taken on 1995 July 21 and 23 on the Palomar 5 m Telescope and yielded a source redshift of $z_s = 1.394$, with prominent high-order Balmer absorption lines and Mg II absorption (Fassnacht et al. 1996). The absence of [O II] emission line indicates that the source is a poststarburst or E+A galaxy. Further infrared imaging obtained on 1995 July 18 with the Cassegrain infrared camera at f70 focus of the Palomar 5 m Telescope hinted at the presence of extended emission from the host. The optical imaging obtained on the Palomar 1.5 m Telescope on 1995 April 24–27 implied the absolute magnitude for the source to be $M(r) = -22.8$ mag after correcting for lens magnification (Fassnacht et al. 1996).

5.2 Time Delays, Flux Ratios, and Image Positions

There were three VLA monitoring campaigns to measure the time delays between the four images in B1608+656 (Fassnacht et al. 1999, 2002). Figure 5.1 shows the VLA observations of B1608+656 that is extracted from Fassnacht et al. (1999). The four images are labeled as A, B, C and D. In the first monitoring season from 1996 October 10 to 1997 May 9, the system was observed by Fassnacht et al. (1999) in 64 epochs that were separated on average by 3.6 days. The lensed source showed only ∼5% variation during this first season, leading to time delay measurements with large (12%–20%) uncertainties (Fassnacht et al. 1999). In both the second (from 1998 Feb 13 to 1998 Oct 19 with 81 epochs) and the third (from 1999 June 15 to 2000 Feb 14 with 92 epochs) monitoring seasons, the source flux density varied by 25%–30%. The joint analysis of all three data sets reduced the uncertainties on the time delays by factors of 2–3; the resulting time delay values were also consistent with those measured from the first season. The three relative time delay values are $\Delta t_{AB} = 31.5 \pm 1.5$ days, $\Delta t_{CB} = 36.0 \pm 1.5$ days, and $\Delta t_{DB} = 77.0 \pm 1.5$ days for the

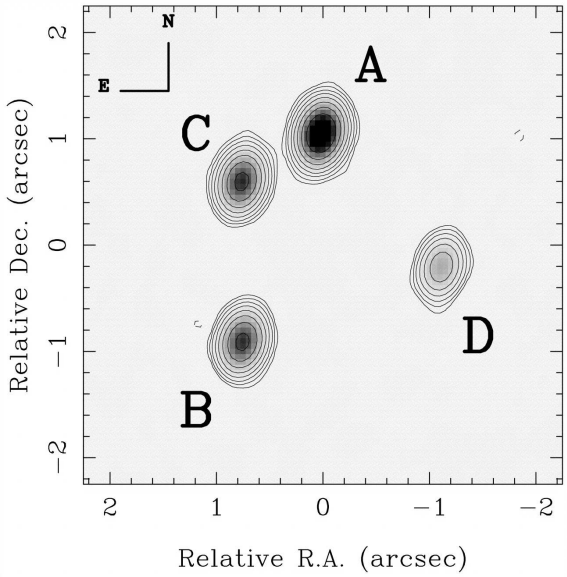

Figure 5.1: Map from VLA observation of B1608+656 on 1996 November 18. The contours are -3, 3, 6, 12, 24, 48, 96, 192, 384, and 768 times the rms noise level of 0.035 mJy beam^{-1}. This map and its caption are obtained from Fassnacht et al. (1999).

1σ confidence limit (Fassnacht et al. 2002). These relative time delays, accurate to within a few percent, make B1608+656 an excellent candidate for measuring the Hubble constant to high precision.

The flux density ratios were also determined from the VLA monitoring (Fassnacht et al. 2002) and are listed in table 5.1. The errors on the individual ratio fluxes are 20%, conservative estimates placed by Koopmans et al. (2003b). The fluxes may be unreliable due to mass substructure (e.g., Mao & Schneider 1998; Metcalf & Madau 2001; Bradač et al. 2002, 2004), radio microlensing (e.g., Koopmans & de Bruyn 2000; Schechter & Wambsganss 2002), or interstellar medium (ISM) propagation effects (Koopmans et al. 2003a). This large uncertainty is justified by the formal errors on the flux ratios within a single season being much smaller than the differences between seasons (Fassnacht et al. 2002). Also listed in table 5.1 are the locations of the four lensed images of the source that were accurately measured with the Very Long Baseline Array (Koopmans & Fassnacht 1999).

Table 5.1: Image positions, flux ratios and relative time delays in B1608+656

Image	$\Delta\theta_1$(arcsec)	$\Delta\theta_2$(arcsec)	$S_{\rm norm}$	Δt(days)
A	$\equiv 0.0000 \pm 0.001$	$\equiv 0.0000 \pm 0.001$	2.020 ± 0.404	31.5 ± 1.5
B	-0.7380 ± 0.001	-1.9612 ± 0.001	1.000 ± 0.200	$\equiv 0.0$
C	-0.7446 ± 0.001	-0.4537 ± 0.001	1.034 ± 0.207	36.0 ± 1.5
D	$+1.1284 \pm 0.001$	-1.2565 ± 0.001	$0.347 \pm \infty$	77.0 ± 1.5

Note. — The image positions are from Koopmans & Fassnacht (1999) using VLBI observations. The flux ratios and relative time delays are from Fassnacht et al. (2002) with VLA monitoring. The image labeling can be seen in figure 5.1.

5.3 *HST* Images

B1608+656 has been observed by the *Hubble Space Telescope* (*HST*) in the optical and infrared wavelengths in three bands (V, I, and H) with four instruments (Wide Field and Planetary Camera 2 [WFPC2], Near Infrared Camera and Multi-Object Spectrometer [NICMOS] 1 and 2 [NIC1 and NIC2], and Advanced Camera for Surveys [ACS]). Reduced images are shown in the next chapter. Table 5.2, that was extracted from Surpi & Blandford (2003) and extended to include the ACS imaging, summarizes the observations. The ACS images in V and I (Proposal 10158; PI: Fassnacht) have signal-to-noise ratios that are higher than the WFPC2, and will therefore be used in the analysis in later chapters. Each orbit of the ACS visits consisted of one 4-exposure dither pattern in one filter (either F606W or F814W) in the Wide Field Channel (WFC) to permit drizzling to higher angular resolution than the default ACS CCD pixel size ($\sim 0.05''$). This subpixel scale is especially important for characterizing the point spread function. In order to correct for the dust extinction in the lens system, we also include the combined NIC1 H-band images (Proposal 7422; PI: Readhead) that has higher signal to noise than NIC2.

5.4 Velocity Dispersion of Lenses

A spectrum of B1608+656 was taken by Koopmans et al. (2003b) on 2000 July 3 using the Echellette Spectrograph and Imager (Sheinis et al. 2002) on the Keck II Telescope. The slit was placed at P.A.=83° and was thus aligned with the major axis of primary lens galaxy G1 within 4°. A slit width of $0.75''$ was used, giving an instrumental resolution of $\sigma \sim 20$ km s^{-1}. Through extensive Monte Carlo simulations, Koopmans et al. (2003b)

Table 5.2: *HST* observations of B1608+656

Proposal PI	Proposal ID	Date	Instrument	Filter	Exposures	Exposure Time (s)
N. Jackson	5908	1996 Apr 7	WFPC2	F555W	1	2
					3	500
				F814W	3	800
E. Falco	7495	1997 Sep 29	NIC2	F160W	4	704
P. Schechter	6555	1997 Nov 1	WFPC2	F606W	4	2900
				F814W	1	2800
					3	2900
A. Readhead	7422	1998 Feb 7	NIC1	F160W	5	3840
					1	2048
					1	896
C. Fassnacht	10158	2004 Aug 24	ACS/WFC	F606W	4	609
					4	646
				F814W	4	632
					4	646
		2004 Aug 25	ACS/WFC	F606W	8	609
					8	646
				F814W	8	632
					8	646
		2004 Aug 29	ACS/WFC	F606W	4	609
					4	646
				F814W	4	632
					4	646
		2004 Aug 29	ACS/WFC	F606W	4	609
				F814W	4	632
					4	646
					4	646

determined the stellar velocity dispersion of the dominant lens galaxy G1 to be $\sigma_{ap} = 247 \pm 35$ km s^{-1} within an aperature of $1.7'' \times 0.75''$ centered on G1.

5.5 X-Ray Measurement

Since B1608+656 lies in a group (Fassnacht et al. 2006), X-ray observations can help determining the positions and masses of galaxy groups and clusters. Dai & Kochanek (2005) obtained X-ray observations of B1608+656 using the Advanced CCD Imaging Spectrometer on *Chandra* for 29.7 ks on 2003 September 21. The lens was placed on the back-illuminated ACIS-S3 chip and the data was taken in the TIMED/VFAINT mode. Images A, B, and C in B1608+656 were resolved in the observation, but image D was not detected. Dai & Kochanek (2005) did not detect significant X-ray emission from nearby galaxy groups or clusters associated with B1608+656. They derived an upper limit for the X-ray luminosity on any cluster at the lens redshift within $4'$ from B1608+656 of $\sim 6 \times 10^{42}$ erg s^{-1}.

5.6 Group Environment

A spectroscopic survey of B1608+656 was conducted by Fassnacht et al. (2006) where redshifts for 97 galaxies in the B1608+656 field were obtained. Figure 5.2, extracted from Fassnacht et al. (2006), shows the spatial distribution of galaxies in the field. Open circles mark the galaxies of which redshifts have been measured. The Low Resolution Imaging Spectrograph in both long-slit and multislit modes (Oke et al. 1995) and the Echellette Spectrograph and Imager (Sheinis et al. 2002) on W. M. Keck Telescopes were used for the observations. The survey led to the discovery of four groups of galaxies along the line of sight to B1608+656 (Fassnacht et al. 2006). One group is at the redshift of the B1608+656 lens system, and contains at least nine members, including the lens. This group appears to have a low mass with estimated velocity dispersion of 150 ± 60 km s^{-1}. The other three groups, each containing $\sim$10 members, lie in front of B1608+656 and are at redshifts of 0.265, 0.426, and 0.52. The groups at 0.265 and 0.52 are roughly centered at the lens (using luminosity-weighted group positions), and the group at 0.426 is located at $\sim 1'$ south of the lens.

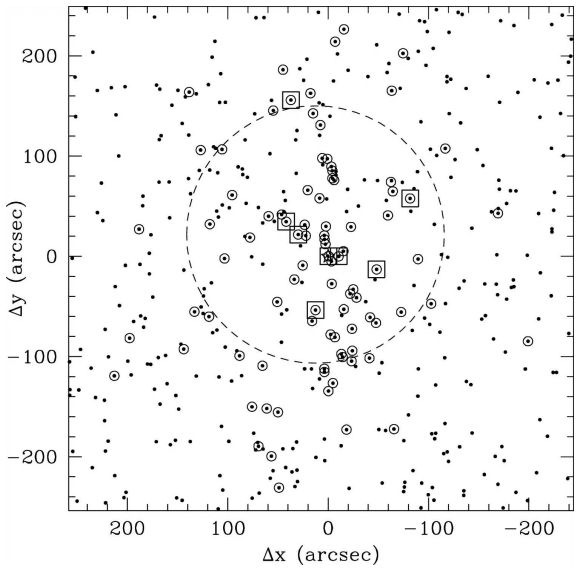

Figure 5.2: Spatial distribution of the galaxies in field of B1608+656. The field of view is $10' \times 11'$, with the axes labeled in terms of offsets from the B1608+656 lens system in units of arcseconds. The dots represent the positions of galaxies with magnitudes $r < 23$, while the open circles mark the galaxies for which redshifts have been obtained. The open squares mark the galaxies in the group that is physically associated with B1608+656. The large dashed circle has a radius of 1 h^{-1} comoving Mpc at the redshift of the lensing galaxy. This figure and its caption are obtained from Fassnacht et al. (2006).

We return to these velocity dispersion and group environment observations in chapter 8, where we discuss their impact on H_0. Meanwhile, in the next chapter, we present the image processing of the *HST* observations.

Chapter 6

Image Processing

The *HST* ACS images of B1608+656 in figure 6.1 show the two galaxy lenses and the presence of a dust lane through the system. Since G1 is an elliptical galaxy which typically contains little dust, Koopmans & Fassnacht (1999) and Surpi & Blandford (2003) suggested that the dust comes from G2, likely a dusty late-type galaxy, through dynamical interaction. This explains the differential color variation in G1 due to dust extinction (Surpi & Blandford 2003) that will also be seen later in this chapter. This may also explain why G1 appears to be a poststarburst galaxy as tidal interactions trigger star formation.

Since the presence of the dust lane through the system and the light from the lens galaxies affect the isophotes of the Einstein ring of the lensed extended source (which are needed for determining the lens potential that is directly related to H_0), we need to correct for the dust and lens galaxies' light. This is the reason for observing B1608+656 in multiple wavelength bands; we can determine the amount of dust by comparing the amount of extinction in different bands (dust extinction is wavelength dependent) and fitting to empirical dust extinction laws. However, before we can determine the amount of extinction, we need to first unify the resolutions of the images in different wavelength bands due to point spread function (PSF) dependences on the wavelength. This requires PSF modeling, deconvolution, and reconvolution for each wavelength band image. Having unified the resolutions of the images, we can determine the intrinsic colors of the various components (lens galaxies, lensed source galaxy, AGN at core of source galaxy) in the system that are needed for dust correction. After correcting for dust, we can then determine the light profiles of G1 and G2 by fitting them to Sersic profiles. At this stage, with the PSF, dust map, and lens galaxies' light profiles, we can recover the lensed Einstein ring for lens

potential modeling. Even though the procedure outlined above for dust and lens galaxies' light corrections appears to be sequential, in fact the effects of the PSF, dust extinction, lens galaxies' light, and lensing are interdependent. It is therefore difficult to fold them into the Bayesian formalism discussed in chapters 3 and 4. Instead, we approach this problem by obtaining a representative sample of models (PSF, dust, lens galaxies' light, and lens potential) and comparing them collectively. We extend the Bayesian analysis introduced in chapters 3 and 4 to compare these models objectively using the evidence from the generalized (see section 6.1 below) source intensity reconstruction.

To execute the above plan of attack, we begin in section 6.1 by extending the formalism in section 4.1 to include the effects of PSF, dust, lens galaxies' light, and lensing. In section 6.2, we describe the drizzling process for the ACS images that were used for the analysis. In sections 6.3 to 6.5, we present a suite of PSF, dust and lens galaxies' light models and describe in detail how they were obtained. Finally, in section 6.6, we compare these PSF, dust and lens galaxies' light models.

6.1 Bayesian Analysis

Suppose that we have a set of PSF, dust and lens galaxies' light models (the process of obtaining these models is described in detail in the next few sections of this chapter), a lens potential model, and the observed image. We can separate the observed image into two components, the lensed source and the lens galaxies, and we can express the observed image (as a vector for the intensities of the image pixels) as

$$\boldsymbol{d} = \overbrace{\mathbf{B}\cdot\mathbf{K}\cdot\mathbf{L}\cdot\boldsymbol{s}}^{\text{lensed extended source}} + \overbrace{\mathbf{B}\cdot\mathbf{K}\cdot\boldsymbol{g}}^{\text{lens galaxies}} + \boldsymbol{n}, \tag{6.1}$$

where $\mathbf{B}$ is a PSF blurring matrix, $\mathbf{K}$ is a dust extinction matrix, $\mathbf{L}$ is the lensing matrix (containing the lens potential model), $\boldsymbol{s}$ is the source intensity distribution, $\boldsymbol{g}$ is the lens galaxies' intensity distribution,[1] and $\boldsymbol{n}$ is the noise in the data characterized by the covariance matrix $\mathbf{C}_{\mathrm{D}}$.[2] This is an extended version of equation (3.1). The order of the matrix

[1]Note that the distinction between the bold-face italic $\boldsymbol{g}$ for the galaxies' intensity distribution and the bold-face sans serif $\mathbf{g}$ for the type of regularization in earlier chapters.

[2]A reminder on the notation: bold-face sans serifs represent matrices and bold-face italics represent vectors. The dimensions of the matrices and vectors are usually $N_{\mathrm{pix}} \times N_{\mathrm{pix}}$ and N_{pix},

products in both terms are obtained by tracing backward along the light rays: we first encounter the PSF blurring from the telescope ($\mathbf{B}$), then dust extinction ($\mathbf{K}$) in the lens plane, then the strong lensing effects ($\mathbf{L}$) in the case of the lensed source, and finally the origin of light ($\boldsymbol{s}$ or $\boldsymbol{g}$). Here we assume that the dust lies in a screen in front of the lensed source and the lens galaxies, which may not be true in the latter case. In general, dust and stars are mingled in the lens galaxies. One approach to modeling this is to assume that the dust is uniformly distributed in the lens galaxies and recover the unreddened light profile (G. Surpi, private commmunications). However, we will see that the dust screen assumption for the lens galaxies is acceptable as we find that the lens modeling based on the recovered Einstein ring depends much more strongly on the PSF and dust (see section 6.6) than on the lens galaxies' light profiles. Therefore, it is unnecessary to obtain high precision lens galaxies' light profiles by treating the realistic (and much harder) situation of mixed light and dust.

If the lensed source contains a bright core such as an AGN, then we could consider extending equation (6.1) and write the observed image as

$$\boldsymbol{d} = \mathbf{B} \cdot \mathbf{K} \cdot \mathbf{L} \cdot \boldsymbol{s} + \sum_{i=1}^{N_{\mathrm{images}}} \alpha_i \mathrm{PSF}(\tilde{\theta}_{\mathrm{i}}) + \mathbf{B} \cdot \mathbf{K} \cdot \boldsymbol{g} + \boldsymbol{n}, \tag{6.2}$$

where the we model the light from the extended part of the host (the first term) separately from the point sources (the second term), and α_i are the intensities of the point sources (which are generally not the same for all images due to time delay difference and finite resolution, even though surface brightness is conserved). For B1608+656, we find that a separate modeling of the point sources is not necessary for reconstructing the lens potential (see chapter 7).

Equation (6.1) is in the form of equation (3.1) in chapter 3 with $\mathbf{f}$ replaced by $\mathbf{B} \cdot \mathbf{K} \cdot \mathbf{L}$ and $\boldsymbol{d}$ replaced by $\boldsymbol{d} - \mathbf{B} \cdot \mathbf{K} \cdot \boldsymbol{g}$; therefore, given $\mathbf{B}$, $\mathbf{K}$, $\boldsymbol{g}$, $\mathbf{L}$ and $\boldsymbol{d}$, one can solve for the most probable source intensity distribution $\boldsymbol{s}_{\mathrm{MP}}$, as outlined in chapter 3 and section 4.1. Furthermore, one can use the Bayesian evidence of the source reconstruction to rank different models of PSF, dust extinction, lens galaxies' light, and lens potential (see section 3.2.2). In essence, a poor PSF, dust, lens galaxies' light, or lens potential model will result in a source reconstruction with poor goodness of fit, and thus a low evidence value. Good

respectively, where N_{pix} represents either the number of image pixels or source pixels.

models will map the multiple lensed images back to the same source intensity distribution, whereas bad models will map the multiple images back to multiple disagreeing copies of the source. It is the multiple nature of the images that allows us to use the reconstructed source to gauge the goodness of models. The next few sections contain details of obtaining a representative suite of PSF ($\mathbf{B}$), dust ($\mathbf{K}$) and lens galaxies' light ($\boldsymbol{g}$) models, and the last section of this chapter compares these models quantitatively and objectively within the Bayesian framework.

6.2 Image Drizzling

Multiband image processing is necessary for correcting for dust extinction. Based on the observations of B1608+656 listed in table 5.2, we select, based on signal to noise, the ACS/WFC F606W and F814W as the images in the V and I bands for the analysis. As mentioned in chapter 5, we also include the combined NIC1 F160W image for dust correction. Since the observations in each band consist of multiple exposures that may be dithered (shifted by a fraction of the CCD pixel size to achieve higher resolution), the exposures need to be "drizzled." Drizzling refers to Variable-Pixel Linear Reconstruction, an algorithm for reconstructing *HST* images with the effects of geometric distortion (both on image shape and photometry) and cosmic rays removed (Fruchter & Hook 1997). The drizzled images on rectangular grids for different instruments are generally not on the same resolution and not aligned. This is the case for the NICMOS and ACS images. We use SWarp[3] to align the combined NICMOS image to the ACS images. In the next two subsections, we briefly describe the drizzling process for combining the dithered ACS images and the SWarping of the NICMOS image.

6.2.1 ACS Image Processing

The ACS images in F606W and F814W were dithered using the pattern described in York et al. (2005) to reduce finite-pixel effects. The two four-point dither patterns with parallelogram shapes allowed the final images to be drizzled onto a subpixelized grid of half the ACS pixel scale. The ACS data were reduced using the multidrizzle package (Koekemoer

[3]Developed by Emmanuel Bertin, SWarp is a program to resample and co-add FITS images using any arbitrary astrometric projection defined in the WCS standard.

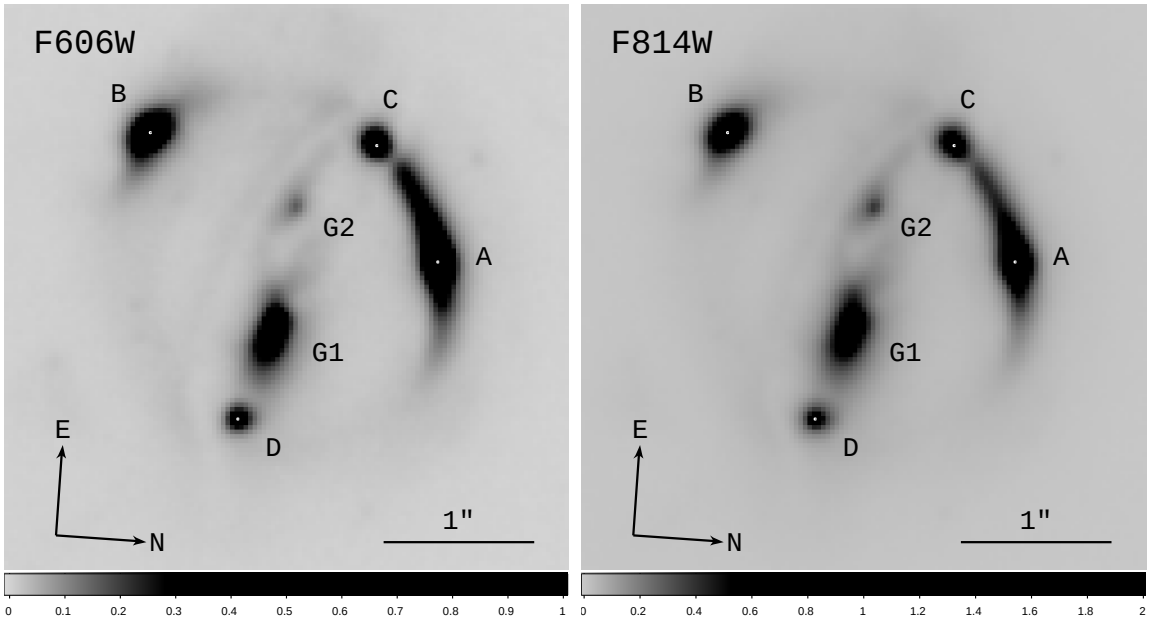

Figure 6.1: Left-hand (right-hand) panel: drizzled *HST* ACS F606W (F814W) images with 0.03″ pixels from 9 (11) *HST* orbits. The dust lane and interacting galaxy lenses are clearly visible.

et al. 2002), producing drizzled images with 0.03″ pixel scale. The drizzled ACS images are shown in figure 6.1. The corresponding output weight images from multidrizzle give the values for the inverse variance of each pixel. We approximate the noise covariance matrix as diagonal and use the variance values for the diagonal entries. Due to the drizzling process, these diagonal entries will generally be overestimated by a factor of a few because the true covariance matrix has off-diagonal elements to take into account the correlation in the noise between adjacent pixels. It is assumed that the effect of drizzling (which results in nondiagonal covariance matrix) can be modeled as having a diagonal covariance matrix with the diagonal elements rescaled (Casertano et al. 2000).

6.2.2 NICMOS Image Processing

The NIC1 F160W image was processed in the same manner as in Koopmans et al. (2003b), and it was transformed to the ACS frame using SWarp. The final SWarped NIC1 F160W image with 0.03″ pixel scales is shown in figure 6.2.

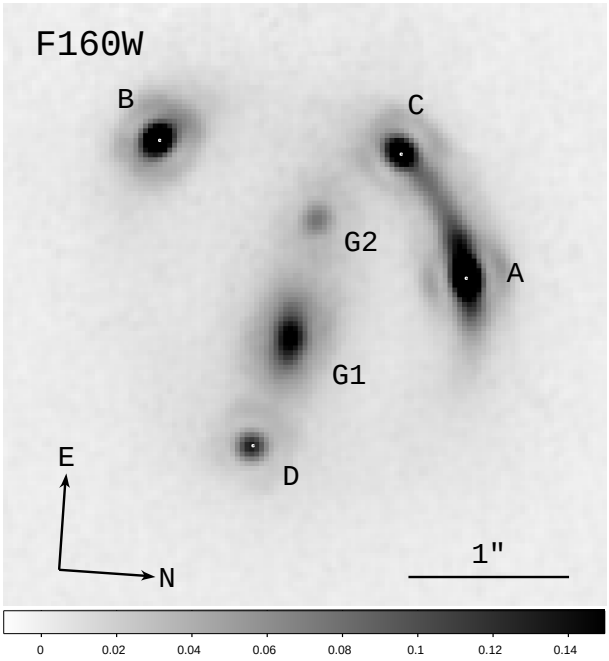

Figure 6.2: *HST* NICMOS F160W image that is SWarped to aligned to the ACS frame with 0.03″ pixel size.

6.3 PSF Modeling

In this section, we describe the procedure for obtaining the PSFs for the ACS and the NICMOS images.

6.3.1 ACS PSF

It is known that the ACS PSF is both spatially and temporally varying (e.g., Rhodes et al. 2007). One source of temporal variation is the "breathing" of the telescope while it orbits, which causes the focal length of the telescope to change (and hence the PSF). Instead of adopting a universal PSF, we take the approach of modeling several PSFs using different means, and comparing them quantitatively using the Bayesian analysis described in chapter 3 and in section 6.1. This has the advantage of using the data (the observed image) to rank the models. For each of the two drizzled ACS images, we create five models for the PSF based on either the Tiny Tim package (Krist & Hook 1997) or the unsaturated stars in the fields: (i) drizzled PSF ("PSF-drz") from the modified Tiny Tim by Rhodes et al. (2007), (ii) single (nondrizzled) Tiny Tim PSF ("PSF-f3") with a telescope focus value of -3, (iii)

closest star ("PSF-C") located at $\sim 9''$ in the northeast direction from B1608+656 in the drizzled ACS field with a Vega magnitude of 21.3 in F814W, (iv) bright star #1 ("PSF-B1") that is located at $\sim 1.9'$ southwest of B1608+656 in the drizzled ACS field with a Vega magnitude of 18.7 in F814W, and (v) bright star #2 ("PSF-B2") that is located at $\sim 1.6'$ south of B1608+656 in the drizzled ACS field with a Vega magnitude of 19.1. These PSFs are shown in figure 6.3 for the F814W image.

The Tiny Tim frame(s) were drizzled and resampled to pixel sizes of $0.03''$ to match the resolution of the ACS images. We keep in mind that the Tiny Tim PSFs (PSF-drz and PSF-f3) may be insufficient due to the time varying nature of the PSF, and the aging of the detector since the Tiny Tim code was written. We expect the closest star to B1608+656 (PSF-C) to be a good approximation to the PSF because the spatial variation of PSF across $\sim 9''$ should be negligible and any temporal variations effect are the same as in the lens. However, this closest star is not bright enough to see the secondary maxima in the PSF, so we include additionally two of the brightest stars in the drizzled field mentioned above. For each of the stars in F606W and F814W, we make a small cutout around the star (25×25 pixels for PSF-C, 51×51 pixels for PSF-B1, and 41×41 pixels for PSF-B2), and centered it on a 200×200 grid, which is the size of the drizzled science image cutouts of B1608+656 that are used for the image processing.

6.3.2 NICMOS PSF

The PSF of NICMOS is thought to be more stable, and thus we use one NICMOS PSF model: the Tiny Tim NICMOS PSF. The output Tiny Tim PSF is in the CCD frame of NICMOS with pixel size $0.043''$. As with the science image of NICMOS F160W, the PSF was SWarped to align to the ACS images with $0.03''$ pixels for the dust correction step. Figure 6.4 shows the SWarped NICMOS PSF in log scale. Since there is only one PSF model for NICMOS, PSF specifications throughout the rest of the chapter generally refer to the ACS PSFs.

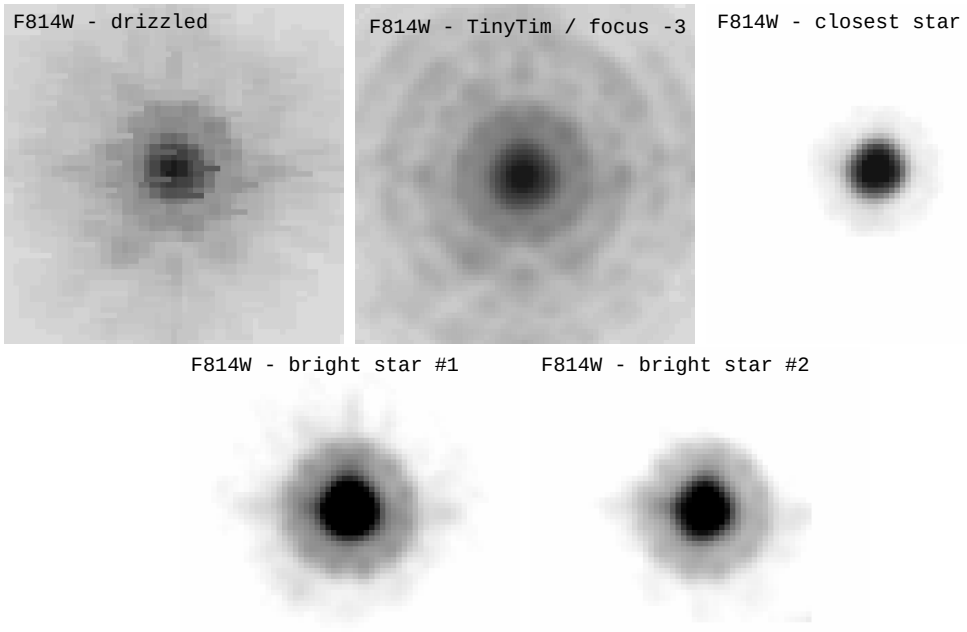

Figure 6.3: ACS F814W PSF models for B1608+656. Top row, from left to right: the drizzled PSF model (PSF-drz) based on Rhodes et al. (2007), the Tiny Tim PSF (PSF-f3) with a focus value of -3, and closest star (PSF-C) to B1608+656 in the drizzled ACS F814W field. Bottom row, from left to right: bright star #1 (PSF-B1) that is located at $\sim$1.9$'$ southwest of B1608+656 in the drizzled ACS F814W field, and bright star #2 (PSF-B2) that is located at $\sim$1.6$'$ south of B1608+656 in the drizzled ACS F814W field. These PSF are plotted on log scales to show small scale (secondary ring) features. PSF-drz (top left-hand panel) does not have a central single peak due to difficulty in the alignment of different frames. PSF-C (top right-hand panel) shows no secondary maxima due to its low signal to noise.

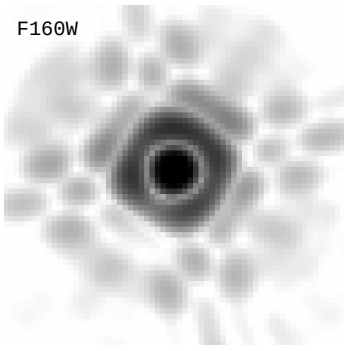

Figure 6.4: The NICMOS F160W PSF obtained from Tiny Tim and SWarped to align with the ACS CCD orientation of B1608+656. The plot is in log scale to show the prominent secondary maxima due to the longer pivot wavelength in F160W.

6.4 Dust Correction

With observations in two or more wavelengths, we can correct for the dust extinction using empirical dust extinction laws. We adopt the extinction law of Cardelli et al. (1989) with the following dust extinction ratios at the redshift of the lens $z_d = 0.63$ for $R_V = 3.1$ (galactic extinction):

$$\frac{A_{\rm F606W}}{A_{\rm V}} = 1.5613,\ \frac{A_{\rm F814W}}{A_{\rm V}} = 1.1386,\ \text{and}\ \frac{\rm A_{F160W}}{\rm A_V} = 0.4133, \tag{6.3}$$

where

$$A_\lambda = (m_{\rm observed} - m_{\rm intrinsic})_\lambda \tag{6.4}$$

is the extinction (difference between the observed and intrinsic magnitudes) at wavelength λ. The values in equation (6.3) agree with the values from the extinction law in Pei (1992) within 1.5%. In order to correct for the extinction, we need to know the intrinsic colors of the objects. For each color type of objects, we denote the intrinsic color of the object by $Q_F = (m_F - m_1)_{\rm intrinsic}$ where $F = 1, \ldots, N_{\rm b}$ is in sequence from the reddest to the bluest wavelengths, and $N_{\rm b}$ is the number of wavelength bands used for dust correction. We separate the color maps (discussed in the following subsection) of B1608+656 into three color types (components) with different intrinsic colors: lens galaxies, lensed extended source (Einstein ring), and the core of the lensed source (AGN point source). Following Koopmans et al. (2003b), we take the bluest color in each of these three components to be the intrinsic color. Combining equations (6.3) and (6.4) and the definition of intrinsic colors, we can write the observed magnitudes at each image pixel in each of the wavelength band F in terms of A_V and the intrinsic magnitude of the reddest wavelength band $(m_1)_{\rm intrinsic}$ as

$$m_F \equiv (m_F)_{\rm observed} = (m_1)_{\rm intrinsic} + Q_F + A_V k_F, \tag{6.5}$$

where $k_F \equiv \frac{A_F}{A_V}$ are constants given by equation (6.3). We can solve for A_V and $(m_1)_{\rm intrinsic}$ at each image pixel by minimizing the following $\chi^2_{\rm dust}$ for each pixel:

$$\chi^2_{\rm dust} = \sum_{F=1}^{N_{\rm b}} \left(m_F - (m_1)_{\rm intrinsic} - Q_F - A_V k_F\right)^2, \tag{6.6}$$

where we have weighted the images of the different bands equally. The solution that minimizes the $\chi^2_{\rm dust}$ is

$$A_V = \frac{\frac{1}{N_{\rm b}}\left(\sum_F k_F\right)\left(\sum_F m_F\right) - \frac{1}{N_{\rm b}}\left(\sum_F k_F\right)\left(\sum_F Q_F\right) - \sum_F k_F m_F + \sum_F k_F Q_F}{\frac{1}{N_{\rm b}}\left(\sum_F k_F\right)^2 - \sum_F k_F^2}, \quad (6.7)$$

and

$$(m_1)_{\rm intrinsic} = \frac{1}{N_{\rm b}}\left(\sum_F m_F - \sum_F Q_F - \sum_F A_V k_F\right), \quad (6.8)$$

where the sums over F go from 1 to $N_{\rm b}$. We emphasize that equations (6.7) and (6.8) give the A_V and $(m_1)_{\rm intrinsic}$ at each pixel. Since A_V varies from pixel to pixel (depending on the amount of dust seen in that pixel), the various A_V values of all pixels provide a dust map. Similarly the $(m_1)_{\rm intrinsic}$ values of all pixels give the dust-corrected image in the reddest wavelength band. The resulting values of $(m_1)_{\rm intrinsic}$ and the intrinsic colors yield the intrinsic (dust-corrected) magnitudes in the other bands $(m_F)_{\rm intrinsic}$ where $F = 2, \ldots, N_{\rm b}$. For any one band F, we can then construct the diagonal dust matrix $\mathbf{K}$ in equation (6.1) whose diagonal entries are $10^{-0.4(m_F - (m_1)_{\rm intrinsic} - Q_F)}$.

6.4.1 Obtaining the Intrinsic Colors

The dust correction method outlined above requires the intrinsic colors from the color maps, which we now discuss in detail. To construct the color maps, we need to unify the different resolutions of the images in different bands (due to the wavelength dependence of the PSF). We do so by deconvolving the F606W, F814W, and F160W images using their corresponding PSFs, and reconvolving the images with the F814W PSF for each set of the five ACS PSFs and the single NICMOS PSF described in section 6.3. Reconvolved images are preferred to deconvolved images because the latter show small scale features (of a few pixels' size) that are artificial due to the amplification of the noise during the deconvolution process. We select the F814W PSF for the reconvolution because F814W will be used for the lens potential modeling, due to its high signal to noise compared to F160W and its less severe dust extinction compared to F606W. In working with the reconvolved images, we assume that the dust varies on a scale larger than the F814W PSF, which is true for the regions near the Einstein ring. For the deconvolution, we use IDL's max_entropy iterative routine that is based on Hollis et al. (1992). In general, increasing the number of iterations would

Table 6.1: The number of iterations in the max_entropy deconvolution routine for the different PSF models in each of the ACS/F606W, ACS/F814W, and NICMOS/F160W images

	F606W	F814W	F160W
PSF-drz: drizzled PSF	56	34	20
PSF-f3: Tiny Tim PSF of focus −3	21	>200	20
PSF-C: closest stellar PSF	16	25	20
PSF-B1: bright stellar PSF #1	14	24	20
PSF-B2: bright stellar PSF #2	15	37	20

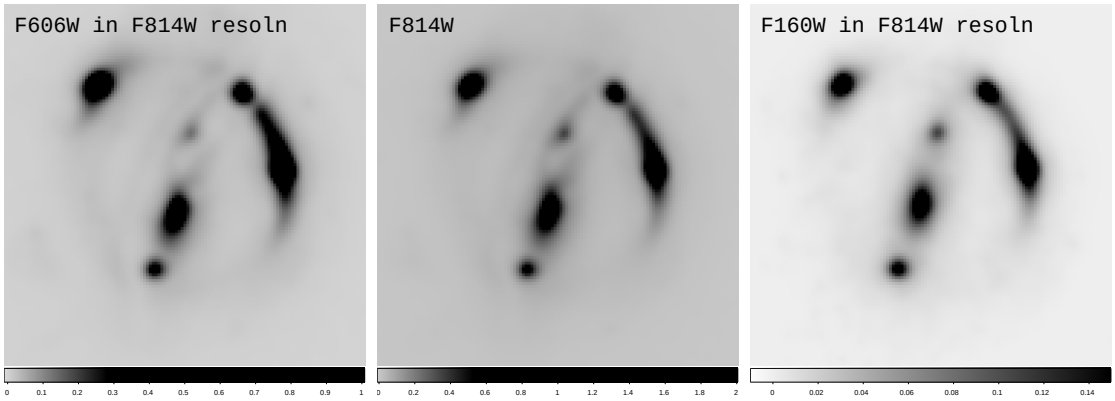

Figure 6.5: From left to right: example deconvolved and reconvolved F606W, F814W, and F160W images in the resolution of F814W. These images were first deconvolved using, respectively, the ACS PSF-B1 and the NICMOS Tiny Tim PSF. They were then reconvolved to the F814W resolution using PSF-B1.

decrease the amount of image residual. For the ACS images, for which we have the weight images, we set the number of iterations in the max_entropy routine such that the reduced χ^2 is $\sim$1; for the NICMOS image, we set the number of iterations to be 20, which gives residual errors (within $\sim$15% near the four point images) that are consistent with the residuals in the ACS deconvolution. Table 6.1 lists the number of iterations in the max_entropy for the different PSF models. We are unable to deconvolve the ACS F814W image using PSF-f3 with a reasonable number of iterations ($\ll$200). This means that PSF-f3 is a bad model, which we have expected due to temporal variations in the PSF. We therefore discard this PSF model. As an example, figure 6.5 shows the reconvolved images for PSF-B1.

For each set of PSF models (PSF-drz, PSF-C, PSF-B1, and PSF-B2 for ACS, and Tiny Tim PSF for NICMOS), we construct the color maps F606W-F814W, F606W-F160W, and

F814W-F160W from the reconvolved F606W, F814W, and F160W. Figure 6.6 shows the three color maps derived from figure 6.5 for PSF-B1. Shown in all three color maps are regions with bluer color slightly west of G1. Since the centroid of this blue region is offset from the centroid of G1, we believe that this blue region arise from differential reddening and not intrinsic color variation within G1 (Surpi & Blandford 2003). The colors maps also show regions of bluer color around images C and D, and we again think these are not purely artificial because of the misalignment in the image positions and the centroids of these blue regions, especially in F606W-F160W and F814W-F160W. Furthermore, we expect and find more dust at the crossing point of the isophotal separatrix of the image pair A–C because lensing models predict the crossing point to be closer to image A. However, these bluer regions near images C and D may also arise from the lensed source being intrinsically bluer than the surrounding. In the F606W-F814W color map, there is a faint ridge of bluer color connecting images A and C. This may be due to the asymmetry in the stellar PSF model (with the star position not exactly centered within a pixel), which would cause the F606W and F814W isophotes to shift relative to each other after the deconvolution and reconvolution. For the color maps from the other PSF models, we find that the color maps from PSF-C and PSF-B2 look similar to PSF-B1 with varying amounts of noise due to varying brightness of the stellar PSFs. PSF-drz gave colors maps that differ from the stellar PSFs (PSF-C, PSF-B1 and PSF-B2) because PSF-drz, especially that of F606W, did not exhibit a single brightness peak but a string of equal brightness pixels at the center due to frame alignment difficulties during the drizzling process. This caused the brightest pixels in the Einstein ring to shift by $\sim$1 pixel after the deconvolution and the reconvolution process in F606W, and created artificial sharp highlights tracing the edge of the ring in the F606W-F814W color map. As will be seen in section 6.6, this leads to PSF-drz and its resulting dust map being ranked lower compared to other models.

In each of the color maps, we mark three color regions: one within the Einstein ring for the lens galaxies, one for the Einstein ring of the lensed extended source, and one for the lensed AGN (core of the extended source). Within each region, we determine the bluest color, assume that this part of the region was not dust extincted, and adopt this color as the intrinsic color. This assumes that each of the three components has constant intrinsic color. Table 6.2 lists the intrinsic colors for each of the three pairs of color maps. Due to the noise in the color maps, the intrinsic colors of F606W-F814W are not identical to the

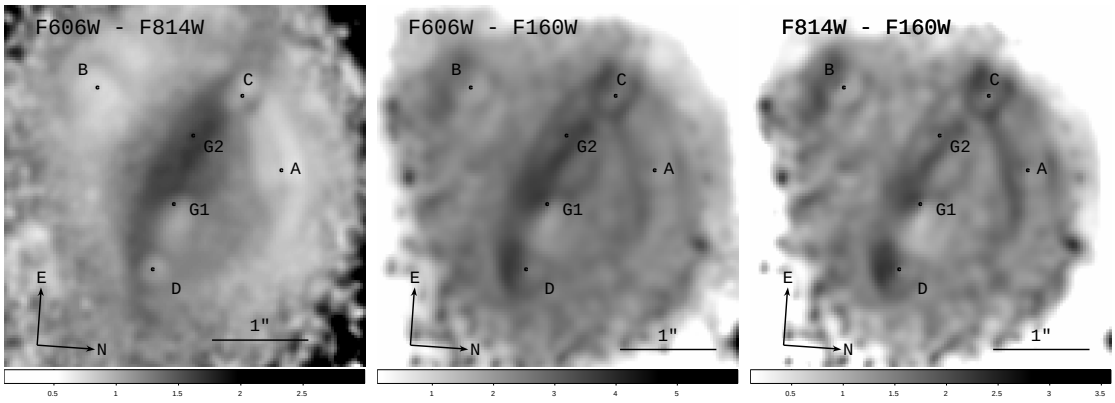

Figure 6.6: From left to right: the derived color maps F606W-F814W, F606W-F160W, and F814W-F160 using PSF-B1 and the images in figure 6.5.

difference between F606W-F160W and F814W-F160W, but agree within the noise.

6.4.2 Resulting Dust Maps

With the intrinsic colors determined for each PSF model, we obtain two dust maps (A_V maps) using (a) only the ACS F606W and F814W images, and (b) the ACS F606W and F814W images together with the NICMOS F160W image. This way, we can assess whether the inclusion of the lower signal-to-noise NICMOS image (with the much broader PSF) improves the dust correction. The left-hand panel of figure 6.7 is the resulting A_V dust map derived using PSF-B1 and using images in all 3 bands. The dust map shows the east–west dust lane through the system (extincting light from C, G2, G1, and D) that is visible in the original drizzled ACS F606W and F814W images. There is little extinction near images A and B, but there are faint dust rings surrounding the images that are mostly due to imperfect F160W deconvolution. The right-hand panel of figure 6.7 is the resulting dust-corrected F814W image that exhibits two signs of proper dust correction: the smoother lens galaxy profiles and the correctly shifted crossing point of the isophotal separatrix of the image pair A–C. The dust maps obtained from the other PSF models with or without the inclusion of the NICMOS image show similar features except for the following two dust maps: (I) The ACS-only (no NICMOS) dust map from PSF-B2 showed a faint ridge of dust connecting images A and C. As explained, this may be due to the asymmetric/bad PSF model. Since the dust map otherwise exhibits the correct features, we keep this dust map

Table 6.2: Intrinsic colors of the AGN, Einstein ring, and lens galaxies in B1608+656

		F606W-F814W	F606W-F160W	F814W-F160W
PSF-drz	AGN	0.50	1.91	1.4
	ring	0.70	2.20	1.5
	lens	0.84	1.88	1.0
PSF-C	AGN	0.78	2.10	1.3
	ring	0.84	2.30	1.5
	lens	1.04	2.05	1.0
PSF-B1	AGN	0.72	1.85	1.1
	ring	0.76	2.10	1.3
	lens	1.04	1.85	0.82
PSF-B2	AGN	0.70	1.99	1.17
	ring	0.80	2.10	1.3
	lens	1.01	1.92	0.85

Note. — The intrinsic colors are based on color maps derived from the four ACS PSF models (PSF-drz, PSF-C, PSF-B1, and PSF-B2) and the single NICMOS Tiny Tim PSF. The intrinsic colors for each of the three color regions are determined from the bluest colors in the respective region.

for the next analysis step.

(II) The ACS-only dust map from PSF-drz. In this case, the dust map showed prominent artificial lensing arc features due to the ∼1 pixel offset in the image positions/arcs in the deconvolved and reconvolved F606W and F814W images. Therefore, we discard this dust map of the ACS-only images for PSF-drz, but keep the dust map derived from using all three bands (that includes NICMOS).

After discarding the ACS PSF-f3 and the ACS-only dust map from PSF-drz, we have a total of seven dust maps (and resulting dust-corrected F814W images) that are derived using a representative set of PSF and intrinsic colors. Recall from the beginning of the chapter, all of these are reasonable dust corrections to use. We will compare these dust maps and PSF models in section 6.6.

6.5 Lens Galaxy Light

For each of the seven resulting dust-corrected F814W images in section 6.4.2 and its corresponding PSF, we create an elliptical mask for the lens galaxies' region that excludes the

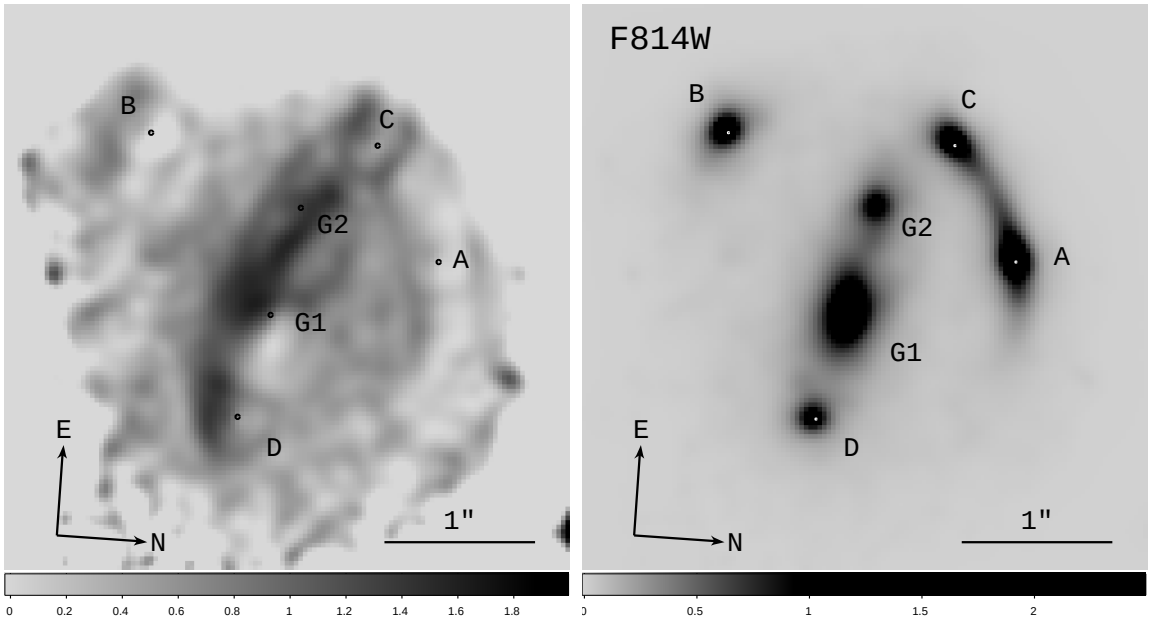

Figure 6.7: Left-hand panel: the A_V map obtained from dust correction with PSF-B1 using all 3 bands of images and the intrinsic colors listed in table 6.2. Galactic dust extinction law was assumed. The dust lane through image C, G2, G1, and D is visible. Right-hand panel: dust extinction corrected F814W image using PSF-B1 and the 3-band dust map in the left-hand panel. Compared to the right-hand panel in figure 6.1, the light profile of G1 is more elliptical and the crossing point of the isophotal separatrix of images A and C has shifted toward A after the dust correction.

Einstein ring, and fit the lens galaxies' light to elliptical Sersic profiles using GALFIT (Peng et al. 2002). In particular, we impose the Sersic indices to be one of the following pairs: $(n_{G1}, n_{G2}) = (1,1), (2,2), (3,3), (3,4), (4,3), (4,4)$. There are more pairings with $n = 3$ and $n = 4$ since previous works by, for examples, Blandford et al. (2001) and Koopmans et al. (2003b) found G1 to be well described by $n = 4$ (de Vaucouleur profile). With the multidrizzle weight image that was scaled to keep the signal to noise the same after dust correction, we obtain a reduced χ^2 value (= χ^2 divided by the number of degrees of freedom, which is the number of pixels minus the number of parameters for describing the elliptical Sersic profiles) for each of the profile fittings. For each dust-corrected F814W image, we pick the Sersic index pair with the lowest χ^2 from the fit (top two pairs in the case of PSF-drz) and list them in table 6.3. As an illustration, figure 6.8 shows the GALFIT Sersic $(n_{G1}, n_{G2}) = (3,4)$ results of the dust-corrected F814W image using the 3-band dust map from PSF-B1. Apart from the cores, most of the observed lens galaxies' light matches the dusted Sersic profiles in the middle panel, as shown in the residual map in the right-hand panel. This misfit near the cores may be due to intrinsic color variations in the lens galaxies or the simplistic assumption that the dust lie in a screen in front of the lenses instead of the more realistic situation of the dust mixing with the light from the lens. The misfit could also arise from a bad PSF or the failure of the single Sersic model at the center. Nonetheless, accurate light fitting near the galaxies is not important; it is the isophotes of the Einstein ring that we need to have accurate dust and lenses' light corrections for the lens modeling. For the ring, the dust screen assumption in our approach is valid. We find that the lens modeling is much more sensitive to the dust and PSF models than the lens galaxy light profiles (see section 6.6), and thus we find it unnecessary to improve the lens galaxies' light modeling at this stage.

6.6 Comparison of PSF, Dust, and Lens Galaxies' Light Models

Following the method outlined in section 6.1 (based on chapter 3 and section 4.1), we can use the Bayesian evidence from the source intensity reconstruction to compare the different PSF ($\mathbf{B}$), dust ($\mathbf{K}$) and lens galaxy light ($\boldsymbol{g}$) models. For each set of $\mathbf{B}$, $\mathbf{K}$, and $\boldsymbol{g}$, we obtain

Table 6.3: Best-fitting Sersic light profiles for the lens galaxies G1 and G2 for the seven different dust-corrected F814W images based on different PSF and dust maps

PSF	dust map	Sersic indices (n_{G1}, n_{G2})	reduced $\chi^2_{\text{lens light}}$
drz	3-band	$(3, 4)$	4.48
drz	3-band	$(3, 3)$	4.53
C	3-band	$(3, 4)$	5.11
C	2-band	$(3, 3)$	6.13
B1	3-band	$(3, 4)$	5.53
B1	2-band	$(2, 2)$	7.16
B2	3-band	$(2, 2)$	5.95
B2	2-band	$(2, 2)$	8.19

Note. — In the PSF column, "drz"≡drizzled Tiny Tim, "C"≡closest star, "B1"≡bright star #1, and "B2"≡bright star #2. In the dust map column, "2-band" represents the dust map obtained from just the two ACS bands, and "3-band" represents the dust map obtained from the two ACS and the one NICMOS band.

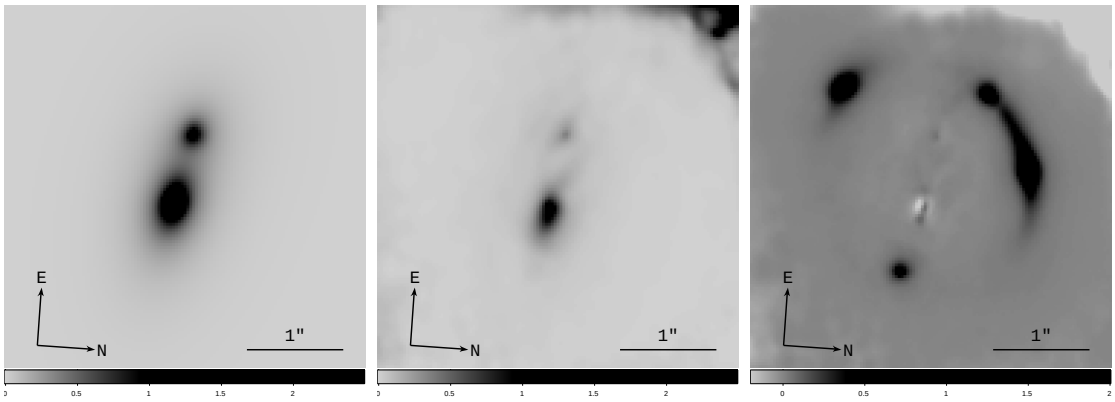

Figure 6.8: Sersic lens galaxy light profile fitting to the dust-corrected F814W image with PSF-B1 and its corresponding 3-band dust map using GALFIT. The left-hand panel shows the best-fit Sersic light profiles with Sersic indices $(n_{G1}, n_{G2}) = (3, 4)$. The middle panel shows the dust extincted galaxy light profiles, which is the left-hand panel with the dust extinction. The right-hand panel shows image residual (difference between the F814W drizzled image in figure 6.1 and the middle panel) with dominant misfit near the cores of the lens galaxies.

the corresponding galaxy subtracted F814 image ($\boldsymbol{d} - \mathbf{B} \cdot \mathbf{K} \cdot \boldsymbol{g}$) that is analogous to the one shown in the right-hand panel of figure 6.8. We then make a 130×130 cutout of the $0.03''$ galaxy subtracted image and use the SPLE1+D (isotropic) lens potential model in Koopmans et al. (2003b), which is the most up-to-date parametric lens potential model for B1608+656, for the source intensity reconstruction.

For model comparison, the data used for the source intensity reconstruction must be the same for all models (so that the normalization in equation (3.22) in section 3.2.2 remains the same for different models). We therefore mark an elliptical annular region enclosing the Einstein ring, and use the data (image intensity values) inside this region for the source intensity reconstructions for each set of the PSF, dust and lens galaxy light models. The source grid, which we fix to have 30×30 pixels, has pixels sizes that are on average $\sim$0.03" to cover the marked elliptical annular region when mapped to the image plane. Even though the source pixel size is large (approximately the same size as image pixel size), we achieve reasonable reconstructions. The required computing memory also becomes prohibitively high as the number of pixels increases, so we keep the number of grid points to be 30×30 for now. In the inversions, we reduced the PSF to 11×11 to keep the matrices such as $\mathbf{B}$ reasonably sparse for computing speed. The regularization matrices are uniform (unweighted), and we try all three forms of regularization (zeroth order, gradient, and curvature).

Table 6.4 lists the suite of PSF, dust and lens galaxies' light models we obtained in the previous section. We label the different models by numbers from 1 to 10 in the left-most column. Models #9 and #10 correspond to the mixing of the dust maps and lens galaxies' light profiles derived from PSF-B1 with PSF-C and vice versa. For each set of models, the source intensity distribution for B1608+656 is reconstructed. As an example, figure 6.9 shows the results of the source reconstruction with zeroth-order regularization (forms of regularizations were described in detail in chapter 4) using PSF-B1, its corresponding 3-band dust map, and resulting Sersic $(n_{\rm G1}, n_{\rm G2}) = (3, 4)$ galaxy light profile. The top left-hand panel shows the reconstructed source intensity distribution that is approximately localized, an indication that the lens potential model is close to the true potential model. The edge pixels in the 1 σ error map in the top middle panel have higher values than the interior pixels due to less regularization on these pixels. The pixels outside the caustics have higher 1 σ error values due to lower image multiplicity outside the caustics. The bottom right-hand panel shows significant image residuals, a sign that the PSF, dust, lens

Table 6.4: PSF, dust, and lens galaxy light model comparison based on Bayesian source inversion

	PSF	dust map	Sersic (n_{G1}, n_{G2})	reg. type	log evidence
1	drz	drz/3-band	drz/3-band/(3, 4)	grad	-7.60×10^4
2	drz	drz/3-band	drz/3-band/(3, 3)	grad	-7.61×10^4
3	C	C/3-band	C/3-band/(3, 4)	zeroth	-6.57×10^4
4	C	C/2-band	C/2-band/(3, 3)	zeroth	-5.45×10^4
5	B1	B1/3-band	B1/3-band/(3, 4)	zeroth	-4.78×10^4
6	B1	B1/2-band	B1/2-band/(2, 2)	zeroth	-4.95×10^4
7	B2	B2/3-band	B2/3-band/(2, 2)	zeroth	-7.59×10^4
8	B2	B2/2-band	B2/2-band/(2, 2)	zeroth	-1.10×10^5
9	C	B1/3-band	B1/3-band/(3, 4)	zeroth	-9.52×10^4
10	B1	C/2-band	C/2-band/(3, 3)	zeroth	-3.90×10^4

Note. — For each set of the PSF, dust, and lens galaxies' light profiles derived in sections 6.3 to 6.5, the Bayesian log evidence value is from the source intensity reconstruction using the SPLE1+D (isotropic) model in Koopmans et al. (2003b). In the PSF column, "drz"≡drizzled Tiny Tim, "C"≡closest star, "B1"≡bright star #1, and "B2"≡bright star #2. In the dust map column, we list which PSF model was used for the dust map derivation, and we list "2-band" for the dust map obtained from just the two ACS bands and "3-band" for the dust map obtained from the two ACS and the one NICMOS band. In the lens galaxy light profile column, we again list which PSF model and dust map were used for obtaining the dust-corrected F814W image for GALFIT and re-state the Sersic indices in table 6.3. The column of "reg. type" refers to the preferred type of regularization for the source reconstruction, based on the highest Bayesian evidence value. It can be one of three types: zeroth order, gradient, or curvature.

galaxies' light, or the lens potential models are not the true ones. In chapter 7, we will use a pixelated potential correction scheme, which is more suitable for interacting galaxy lenses, to improve the parametric SPLE1+D (isotropic) model. The source intensity reconstructions using other PSF, dust and lens galaxies' light models give overall similar inverted source intensities and image residuals, but the source intensities can be more localized or more scattered and the magnitude and structures of the images residual vary for different model sets.

Table 6.4 summarizes the results of model comparison. The "reg. type" column denotes the preferred type of regularization for the source reconstruction based on the highest Bayesian evidence value. It can be one of the three types that we use: zeroth order,

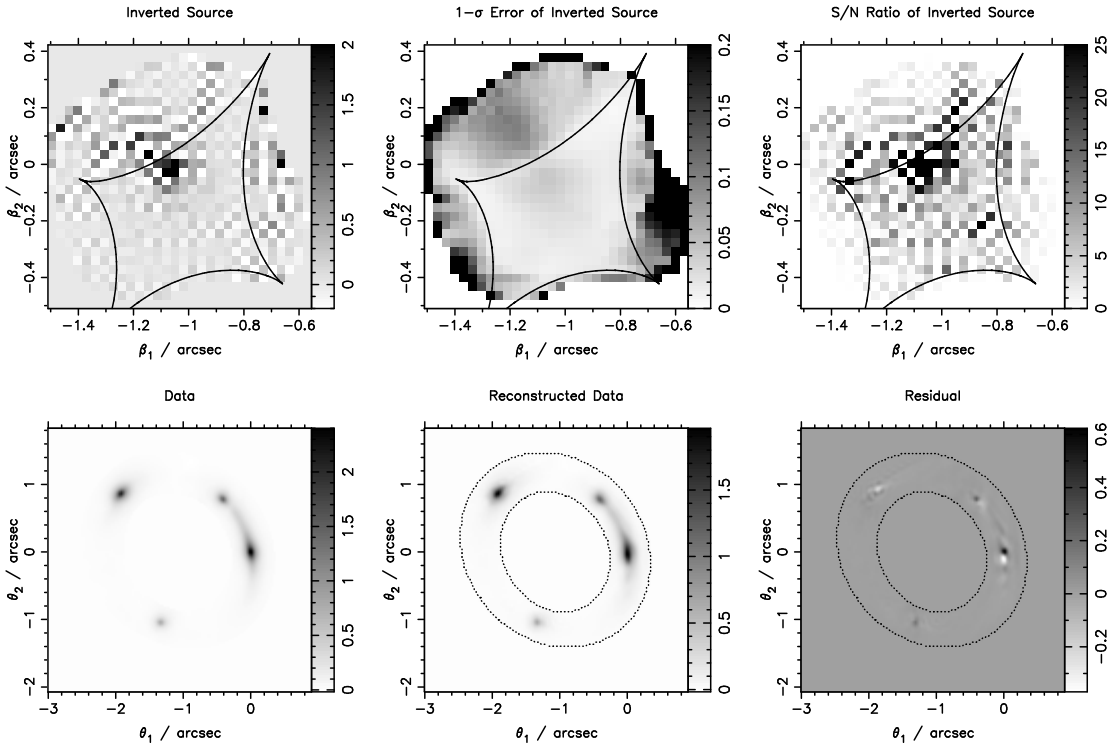

Figure 6.9: Source intensity reconstruction of B1608+656 with PSF-B1 and its corresponding 3-band dust map and lens galaxy light (Model 5 in table 6.4). Top panels from left to right: the reconstructed source intensity distribution with the caustic curves of the SPLE1+D (isotropic) model, the 1 σ error for the source intensity values, and the signal-to-noise ratio that is the ratio of the left-hand panel to the middle panel. Bottom panels from left to right: the observed F814W galaxy subtracted image, the reconstructed image using the reconstructed source in the top left-hand panel, and the image residual that is the difference between the bottom left-hand and the bottom middle panels.

gradient, and curvature. The last column lists the log evidence values from the inversions. Assuming the different models to be equally probable a priori, we use these evidence values for model comparison. The log evidence values range from -3.90×10^4 to -1.10×10^5. The difference between the evidence values in models 1 and 2 (where the models only differ in the Sersic light profiles) is in general much smaller than the difference between models with different PSF or dust model, justifying our earlier claim that the source reconstruction (part of lens modeling) is much less sensitive to the galaxies' light profiles than the PSF/dust models. Models 1 and 2 with PSF-drz have log evidence values on the low side, which was expected with PSF-drz not having a single brightness central peak due to misalignments in the drizzling process. Models 3 and 4 with PSF-C is better than Models 1 and 2, but they are still not the best in the list, possibly due to the low signal to noise in the PSF (hence the absence of secondary maxima) with the closest star being relatively dim. Models 5 and 6 from PSF-B1 are the best models in Models 1 through 8 where there is no mixing of PSF and dust maps, with Model 5 (3-band dust map) being preferred to Model 6 (2-band dust map). This implies that the PSF variation across the ACS field between B1608+656 and the location of the bright star #1 should be sufficiently small such that the gain in the signal to noise in the PSF is preferred. We see that this is not the case with Models 7 and 8 from PSF-B2, which have lower log evidence values than Models 3 and 4 from PSF-C. The PSF variation between B1608+656 and the location of the bright star #2 or the asymmetry in the PSF due to the star not being centered on a single pixel may explain the less preferred Models 7 and 8. Models 9 and 10 are mixed models, in the sense that we use PSF-C but use the dust map and lens galaxy light derived from PSF-B1 (and vice versa) for the source reconstruction. In Model 9 where we use PSF-C, the resulting log evidence value is near the low end, and in Model 10 where we use PSF-B1, the resulting log evidence value is the highest among all the models. Comparing Model 9 to Model 5 and comparing Model 10 to Model 4, we see the importance of having a high signal-to-noise PSF even if the shape of PSF is compromised (since we expect PSF-B1 to be less accurate in shape due to ACS variation across field). The results of Models 3–8 show that it depends on the input PSF whether the inclusion of the NICMOS image for dust correction would produces a better dust map. In Models 3 and 4, excluding NICMOS created a better model, where as for Models 5–8, including NICMOS is better. Most of the models show that zeroth-order regularization is preferred to gradient and curvature; however, we mention that the

difference in the log evidence values between the different regularization schemes are very small ($\lesssim 0.02 \times 10^4$) and the resulting reconstructions for different types of regularization are almost identical. This is because differences in evidence are currently dominated by changes in goodness of fit rather than subtle differences between the prior forms. Only when the image residual is reduced will the prior (regularization) begin to play a greater role in avoiding the reconstruction to fit to noise in the data by keeping the source model simple.

This chapter has illustrated a method of creating sensible PSF, dust, and lens galaxies' light models for the gravitational lens B1608+656. We have by no means exhausted all possible PSF, dust and lens galaxies' light modeling, but what we provide is a representative sample of models and an objective and quantitative approach for comparing these models. This collection of PSF, dust and lens galaxies' light models leads to image residuals that cannot be beaten down further unless we improve the SPLE1+D (isotropic) parametric lens potential model by Koopmans et al. (2003b) to take into account the two *interacting* galaxy lenses. The pixelated potential reconstruction of B1608+656 is the subject of chapter 7.

Chapter 7

Lens Potential Model

In the previous chapter, we obtained a suite of PSF, dust and lens galaxies' light models and presented a method for comparing these models given a lens potential. In this chapter, we focus on the determination of the lens potential that is crucial for measuring the Hubble constant.

7.1 Introduction

Traditionally, parametric lens potentials (such as singular isothermal ellipsoids, singular power law ellipsoids, etc.) have been used to model gravitational lenses. The parameters of the lens (mass, ellipticity, etc.) were obtained by fitting the predictions of the model to the observed quantities such as the image positions of the lensed object, the flux ratios, time delays, etc. This approach is often sufficient for simple isolated systems with a single lens galaxy. However, in the case of B1608+656, the lens is comprised of two *interacting* galaxies. We therefore do not expect B1608+656 to be well described by simple parametric models. This is demonstrated in the next section where the most comprehensive parametric lens model of B1608+656 to date (Koopmans et al. 2003b) is shown to violate the qualitative constraints discussed in section 2.2.4. To account for the interacting galaxies and the possible presence of substructures in the lens, we will reconstruct the potential on a grid of pixels. This is possible (i.e., the many pixel values of the potential are not underconstrained) because the source intensity distribution is extended and multiply imaged. We use the perturbative and iterative potential reconstruction scheme proposed by Blandford et al. (2001) that was also studied by Koopmans (2005). In this method, an initial lens potential

model is perturbatively and iteratively corrected to obtain the true lens potential. The initial lens potential will be parametric (to allow faster convergence with a smaller number of parameters) and would ideally be close to the true potential. It will then be refined via perturbative and iterative corrections on a grid of pixels.

Another approach to pixelated lens modeling is to solve for the dimensionless surface mass density on a grid of pixels (e.g., Williams & Saha 2000; Saha et al. 2006). However, this is not well suited for the Hubble constant measurement since H_0 is directly related to the lens potential not the lens mass density. Furthermore, both Williams & Saha (2000) and Saha et al. (2006) only use the image positions of the lensed source and not the Einstein ring of the lensed extended source to constrain the lens mass density.

In section 7.2, we describe the initial parametric model used for B1608+656. In section 7.3, we review the method of potential reconstruction proposed by Blandford et al. (2001) and test the method using two different approaches: integration along characteristics (section 7.3.1) and matrix inversion (section 7.3.2). Part of this work was published in Suyu & Blandford (2006). Finally, in section 7.3.4, we apply the pixelated potential reconstruction method to B1608+656.

7.2 Initial Parametric Model

The most comprehensive parametric lens modeling of B1608+656 to date was performed by Koopmans et al. (2003b), who described the lenses as singular power law ellipsoids (SPLE) (equation (2.16)). The parameters of the models and the Hubble constant were constrained by fits to (a) the four image positions measured by Very Large Baseline Array (Koopmans & Fassnacht 1999), (b) the radio flux ratios (except for the use of image D) (Fassnacht et al. 2002) and the three relative time delays (Fassnacht et al. 1999, 2002) from Very Large Array observations, (c) the Einstein ring (tracing along 90 equally separated radial spokes the brightest points of the ring on the spokes) from optical (GO-6555; PI: Schechter) and infrared (GO-7422; PI: Readhead) *HST* images (see table 5.2), and (d) the velocity dispersion of G1 (Koopmans et al. 2003b). As in section 2.2, we adopt the parameter values in the SPLE1+D (isotropic) model in Koopmans et al. (2003b), which are listed in table 2.1.

Recall the critical curves and limit curves of the SPLE1+D (isotropic) model (figure

2.2), and the crossing and tangency conditions that they must satisfy (discussed in section 2.2.4). We use the result of section 2.2.4 to qualitatively test the SPLE1+D (isotropic) model in Koopmans et al. (2003b) by superimposing the critical and limit curves of the model on the intensity contours of the observational data. Figure 7.1 shows the isophotal separatrices (in black in various line styles) of the deconvolved, dust corrected, and lens galaxy subtracted *HST*/WFPC2 F814W image of B1608+656 (Koopmans et al. 2003b) with the critical curves (red) and limit curves (green, orange, cyan). We check the crossing and tangency conditions for each of the four sets of isophotal separatrices, using figure 2.7 as a guide for the approximate crossing and tangency locations. For the dashed isophotes, the conditions for the crossing of the separatrix at the critical curve and the tangency to the limit curves are violated. For the solid isophotes, the crossing at $(\theta_1, \theta_2) \sim (-0.8, -1.1)$ is not at the critical curve, but the tangency requirements at $\sim(0.9, -1.4)$ and $\sim(0.4, 0.3)$ are satisfied within the noise. For the dotted isophotes, the crossing at $\sim(0.7, -1.9)$ is at the critical curve within the noise, but the isophotes near $\sim(-0.5, -0.9)$ and $\sim(1.1, 0.2)$ are not tangent to the limit curves. Lastly, for the long-dashed isophotes, the crossing at $\sim(1.3, -0.6)$ is on the critical curve, and the isophotes near $\sim(-0.5, -0.6)$ and $\sim(-0.3, -2.4)$ are tangent to the limit curves, within the noise. Therefore, the SPLE1+D (isotropic) model proposed by Koopmans et al. (2003b) satisfies the crossing and tangency conditions stated in section 2.2.4 for some, but not all, of the isophotal separatrices. As a result, the model proposed by Koopmans et al. (2003b) must not represent the true lens potential of the system, especially in the regions where the crossings and tangencies fail. This reflects the fact that the two lens galaxies are interacting; thus they cannot be perfectly described by elliptical mass distributions. Recall that we need an accurate model of the lens potential to calculate the Hubble constant. In the next section, we examine the method of potential correction.

The potential reconstruction method in the next section requires the starting potential to be "close" to the true potential (which we quantify in the subsequent sections). For sources that are extended enough that the images are well connected by light from the source, the iterative process of potential correction either converged to the true potential from a close enough initial model (with a resulting localized source intensity reconstruction with minimal image residual), or the iterative process does not converge to a solution from an initial model that is not close to the true model. For the sources that are not extended

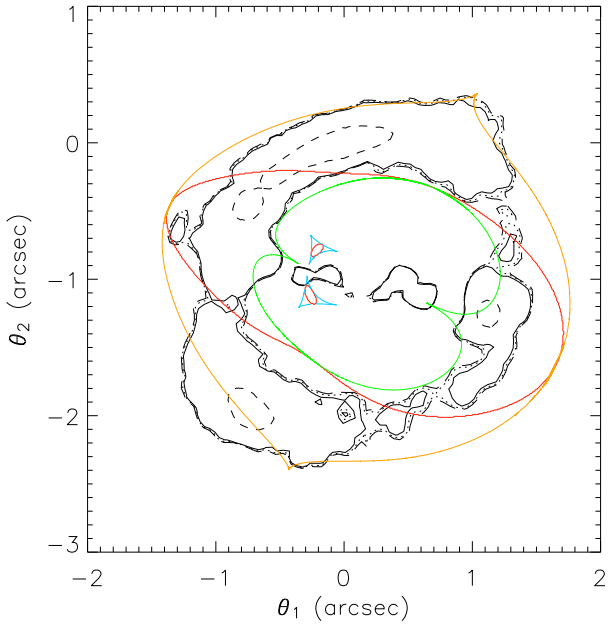

Figure 7.1: The deconvolved, dust corrected, and lens galaxy subtracted *HST*/F814W image of B1608+656 (Koopmans et al. 2003b). The isophotal separatrices (in black in various line styles) are shown with the critical curves (red) and limit curves (green, orange, and cyan) of the SPLE1+D (isotropic) model in Koopmans et al. (2003b). Some of the isophotal separatrices are not intersecting at the critical curve of the model and some of the satellite isophotes are not tangent to the limit curves of the model.

enough, we can obtain local corrections to the potential near high signal-to-noise images of the lensed source to faithfully reconstruct the source with minimal image residual, but the method does not permit the determination of the global offset between isolated images. In section 7.3.4, the iterative potential reconstruction using SPLE1+D (isotropic) (Koopmans et al. 2003b) as the initial model is shown to converge for a representative PSF, dust, and lens galaxy light models (i.e., the image residual is reduced and the source reconstruction is more localized after potential correction). Therefore, this initial model is indeed close enough to the true potential, and it is not necessary to find a new initial parametric model for B1608+656. The initial source intensity reconstruction with the uncorrected SPLE1+D (isotropic) model for a given PSF, dust and lens galaxies' light model was shown in figure 6.9 in chapter 6. Despite having an initial model, we briefly describe a method for finding an initial parametric model in the rest of this section for completeness.

Suppose we are to determine the parameter values of a parametric potential model using the data from lensing alone. The key to determining the parameter values given the data is embedded in equations (3.22) and (3.23). Approximating $P(\lambda|\boldsymbol{d},\mathbf{f},\mathbf{g})$ by a delta function centered on the most probable constant, $\hat{\lambda}$, the model-ranking evidence $P(\boldsymbol{d}|\mathbf{f},\mathbf{g})$ in equation (3.23) can thus be approximated by $P(\boldsymbol{d}|\mathbf{f},\mathbf{g},\hat{\lambda})$ in equation (3.19). Therefore, for a set of parameter values in the potential model (which is incorporated in $\mathbf{f}$), we perform the source reconstruction outlined in chapter 4 and use the resulting Bayesian evidence and the prior on the parameter values as the yard stick. Usually, the prior on the parameter values are observationally motivated. For example, by fitting the two mass components in B1608+656 as singular power law ellipsoids (described earlier in this section), one possible prior on the parameters of SPLE model is to assume that mass follows light and to demand that the centroids and position angles match to the observed values within error bars. This can be translated as imposing Gaussian priors on the centroids and positions angles with the standard deviations given by the measurement error bars. In using equation (3.22) to compare different parametric models, it is important to keep in mind that the data set $\boldsymbol{d}$ must be kept the same. This was emphasized in chapters 4 and 6 , where we mark an annular region enclosing the Einstein ring and use the data in this region for the source reconstruction. As a result, the source intensity reconstruction region will usually be nonrectangular and will change from one parametric potential model to another. For computational simplicity, we use a big enough rectangular grid on the source plane such that when this rectangu-

lar region is mapped to the image plane, the mapped region encloses the marked annular region. We then create a mask on the rectangular source grid to exclude the pixels that are not mapped to the annular region on the image plane. We only reconstruct the source intensities of pixels within the mask, which is generally nonrectangular. The regularizing functions described in appendix A can be easily generalized for this nonrectangular source reconstruction region. The top-most and right-most pixels in the region (instead of the top and right edge of pixels) are patched with lower derivatives to ensure a nonsingular Hessian of $E_{\rm S}$.

In addition to gravitational lensing observations, one can use stellar dynamics to further constrain the parameter values and break the mass-sheet degeneracy (e.g., Grogin & Narayan 1996a,b; Tonry & Franx 1999; Koopmans & Treu 2002; Treu & Koopmans 2002; Barnabè & Koopmans 2007) (the mass-sheet degeneracy was described in section 2.1.2). This will be discussed in more detail in section 8.2. The joint analysis of lensing and stellar dynamics is beyond the scope of this thesis, and we refer the reader to, e.g., Barnabè & Koopmans (2007) for more details on this subject.

The nonlinear optimization of the Bayesian evidence (either from lensing only or joint lensing and dynamics) gives the parameter values for the initial parametric model that is then used for the pixelated potential reconstruction.

7.3 Potential Reconstruction

The method of potential reconstruction was first suggested by Blandford et al. (2001). Following the notation in section 2.1, let $I(\vec{\theta})$ be the observed image intensity of a gravitational lens system with an extended source. For a given potential model, $\psi(\vec{\theta})$, one can obtain the best-fitting source intensity distribution (e.g., Wallington et al. 1996; Treu & Koopmans 2004; Warren & Dye 2003; Dye & Warren 2005; Brewer & Lewis 2006, chapters 3 and 4). Let $I(\vec{\beta})$ be the source intensity translated to the image plane via the potential model, $\psi(\vec{\theta})$. We define the intensity deficit on the image plane by

$$\delta I(\vec{\theta}) = I(\vec{\theta}) - I(\vec{\beta}), \tag{7.1}$$

where $\vec{\theta}$ and $\vec{\beta}$ are related via the lens equation (2.3). The intensity deficit is zero everywhere with the true lens potential distribution, up to the noise in the data.

Consider a lens potential model that is perturbed from the true potential, $\psi_0(\vec{\theta})$, by $\delta\psi(\vec{\theta})$:

$$\psi(\vec{\theta}) = \psi_0(\vec{\theta}) + \delta\psi(\vec{\theta}). \tag{7.2}$$

We can correct the potential model perturbatively by solving for the perturbation $\delta\psi(\vec{\theta})$. For a given image (fixed $\vec{\theta}$ and $I(\vec{\theta})$), we can relate a change in position on the source plane, $\delta\vec{\beta}$, to the potential perturbation using the lens equation (2.3):

$$\delta\vec{\beta} = -\frac{\partial\delta\psi(\vec{\theta})}{\partial\vec{\theta}}. \tag{7.3}$$

Expanding $I(\vec{\beta})$ to first order in $\delta\vec{\beta}$ and using equation (7.3) in equation (7.1), we obtain

$$\delta I(\vec{\theta}) = -\frac{\partial I(\vec{\beta})}{\partial\vec{\beta}} \cdot \delta\vec{\beta} = \frac{\partial I(\vec{\beta})}{\partial\vec{\beta}} \cdot \frac{\partial\delta\psi(\vec{\theta})}{\partial\vec{\theta}}. \tag{7.4}$$

The source intensity gradient $\frac{\partial I(\vec{\beta})}{\partial\vec{\beta}}$ implicitly depends on the potential model $\psi(\vec{\theta})$ since the source position $\vec{\beta}$ (where the gradient is evaluated) is related to $\psi(\vec{\theta})$ via the lens equation (2.3). To first order, using the perturbed model $\psi(\vec{\theta})$ is equivalent to using the true model $\psi_0(\vec{\theta})$ in the evaluation of the source intensity gradient $\frac{\partial I(\vec{\beta})}{\partial\vec{\beta}}$.

We can solve equation (7.4) for the potential correction, $\delta\psi(\vec{\theta})$, provided that we start at a potential model that is close to the true potential. (We quantify what "close" means in the subsequent subsections.) Using the updated potential, we can repeat the source reconstruction and potential correction process. This leads to a perturbative and iterative reconstruction method. We expect the potential to be closer to the true potential after each iteration, which is indicated by a decrease in the magnitude of the intensity deficit.

The potential reconstruction method can be pixelated, thus providing a flexible parametrization scheme. With perfect data, we can pixelate the potential distribution to match the observed image pixelation; however, with realistic noisy data, the potential grid needs to be coarser than the data grid to allow both the source intensity distribution and the potential to be constrained. For the source reconstruction in chapter 4 that uses pixelated potential on the same resolution as the data, we bilinearly interpolate the coarse potential grid to get

it on the finer data grid.

7.3.1 Integration along Characteristics

One method to solve for the potential correction is to integrate along the characteristics of the partial differential equation (7.4). The solution is

$$\delta\psi(\vec{\theta}) = \delta\psi(\vec{\theta_A}) + \int_{\vec{\theta_A}}^{\vec{\theta}} \frac{d\theta_s \delta I(\vec{\theta})}{\left|\frac{\partial I(\vec{\beta})}{\partial \vec{\beta}}\right|}, \tag{7.5}$$

where

$$d\theta_s = \left(d\theta_1^2 + d\theta_2^2\right)^{1/2}, \tag{7.6}$$

$$\left|\frac{\partial I(\vec{\beta})}{\partial \vec{\beta}}\right| = \sqrt{\left(\frac{\partial I(\vec{\beta})}{\partial \beta_1}\right)^2 + \left(\frac{\partial I(\vec{\beta})}{\partial \beta_2}\right)^2}, \tag{7.7}$$

and $\vec{\theta_A}$ is an arbitrary reference point that is conveniently chosen to be at the location of one of the images, say A. (The reference point is arbitrary because the potential is determined up to a constant.) The characteristic curves, on which we must integrate to obtain the potential correction, are given by curves that satisfy

$$\frac{d\theta_1}{d\theta_2} = \frac{\partial I/\partial \beta_1}{\partial I/\partial \beta_2}. \tag{7.8}$$

Each point on a characteristic curve thus follows the source intensity gradient (evaluated at the corresponding source location given by the lens equation (2.3)) that is directly translated to the image plane without distortions via the magnification matrix. Due to the direct translation of the source intensity gradient, the characteristic curves differ from the curves on the image plane that map to the source intensity gradient curves. The structure of the characteristic curves allows us to determine whether the potential solution given by equation (7.5) is unique. This is demonstrated in the example toy model that follows.

To summarize, the four steps for the method are: (i) start with a potential model close to the true potential, (ii) calculate the intensity deficit (equation (7.1)) of each pixel, (iii) calculate the potential correction of each pixel (equation (7.5)) by integrating along the characteristics (equation (7.8)), (iv) obtain the corrected potential and repeat the process (steps (ii) to (iv)) until the intensity deficit approaches zero. In the remainder of this

subsection, we examine a quadruply imaged toy model to test the method of potential reconstruction.

Example Toy Model for Integration along Characteristics

To demonstrate the method of potential reconstruction via integration along the characteristics, we consider a toy model with a simple lens potential that produces a quad like B1608+656.

The toy system has a nonsingular isothermal ellipsoid lens whose potential takes the form:

$$\psi(\theta_1, \theta_2) = (\theta_1^2 + 2\theta_2^2 + 0.1)^{1/2}. \tag{7.9}$$

We take the perturbed potential to be the original potential that is rotated clockwise by 1.1 degrees. The source intensity distribution has elliptical contours with axis ratio of 0.634 and position angle of 147.2 degrees. The source nucleus is located at $(\beta_{1s}, \beta_{2s}) = (0.1, 0.05)$ and has an intensity peak of 100, in arbitrary units. We assume the data is perfect with no noise, but we discretize the image plane region [-2,2]×[-2,2] into a 201×201 grid in order to correct for the perturbation of every pixel. In figure 7.2, the left-hand panel shows the caustic curves (dashed) and the source intensity contours (dotted), and the right-hand panel shows the corresponding critical curves (dashed) and image intensity contours (dotted). Analogous to B1608+656, there is an astroid caustic in the left-hand panel. The additional elliptical caustic curve is due to the nonsingular nature of the lens potential. Different regions separated by the caustic curves have different image multiplicities. In the enclosed region intersected by the astroid and elliptical caustic curves, a source has five images on the image plane. In the region within the caustic curves excluding the intersection, a source has three images. In the region outside the caustic curves, a source has one image. The astroid caustic is mapped to the outer critical curve and the elliptical caustic is mapped to the inner critical curve. As for B1608+656, we focus on the astroid caustic and the outer critical curve. Among the isophotes in the right-hand panel, the four isophotal separatrices that are shown match to the four isophotes tangent to the astroid caustic in the left-hand panel. The separatrices intersect at the outer critical curve, as required (section 2.2.4). Figure 7.3 shows the arrival time delay contour of the source nucleus of the toy model. The

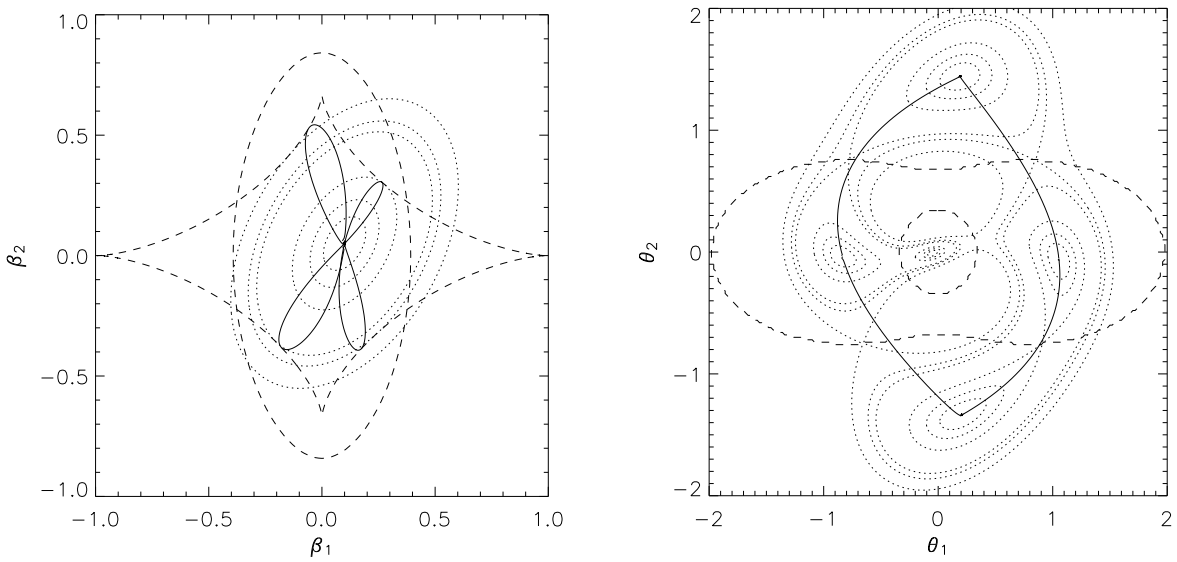

Figure 7.2: Left: the caustic curve (dashed) of the original toy potential model with the intensity contours (dotted) of the source. Four of the intensity contours are tangent to the caustic curves. The four mappings of the connecting characteristics (solid) are each tangent to the caustics. Right: the critical curves (dashed) of the original toy potential model and the image intensity contours (dotted), four of which are isophotal separatrices intersecting at the outer critical curve. The four connecting characteristics (solid) between the four images each cross the outer critical curve once.

quad has similar time delay extrema (two saddles within the critical curve and two minima outside the critical curve) to the SPLE1+D (isotropic) model of B1608+656.

We simplify the potential correction method by using the original source intensity distribution and the characteristic fields of the original potential (instead of reconstructing from the perturbed potential). In practice, we would have to use the reconstructed source (e.g., Wallington et al. 1996; Treu & Koopmans 2004; Warren & Dye 2003; Dye & Warren 2005; Brewer & Lewis 2006, chapter 4) and the characteristic fields of the perturbed potential. This would involve simultaneously determining the source and lens potential distributions and investigating the partial degeneracy between them, which is beyond the scope of this subsection. We use the simplifying assumptions on the source intensity and characteristic curves as the first step to testing the method of potential reconstruction via integration along characteristics. Only if the method works robustly in this simplified regime is the consideration of the more general problem relevant.

Figure 7.4 shows the characteristic field given by equation (7.8). The field has "attrac-

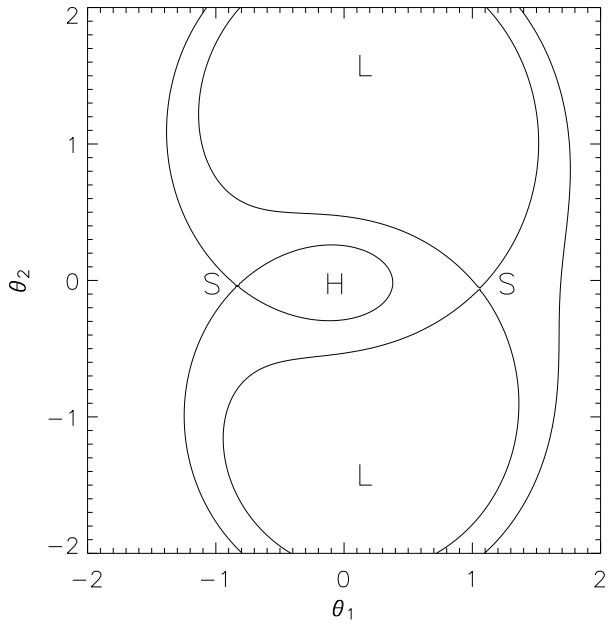

Figure 7.3: The time delay contour associated with the source nuclear position of the toy model. The image locations of the source nucleus (see figure 7.2 right-hand panel) are at time delay saddles (S), minima (L) or maxima (H).

tors" (where field lines come together) and "repellors" (where field lines curve away) at the image locations of the source nucleus. Using equation (2.7) and noting that the Jacobian matrix of $T(\vec{\theta}, \vec{\beta})$ with respect to $\vec{\theta}$ is equivalent to $\mathbf{A}$ in equation (2.8) up to a constant coefficient, one can show that the attractors (or repellors) are associated to time delay minima/maxima (or saddles) for a source distribution that has noncrossing intensity contours. A comparison between figure 7.3 and figure 7.4 confirms this fact.

We need to follow along the characteristics to correct for the potential perturbation given by equation (7.5). In figure 7.4, almost all of the characteristic curves end at one of the three attractors; but there are special characteristic curves that connect the attractors and repellors. These four *connecting characteristics* between the four images (excluding the central image), shown in the right-hand panel of figure 7.2 in solid lines, allow us to fix the potential offsets between the images and hence uniquely determine the potential up to a constant. The left-hand panel of figure 7.2 shows the mapping of these connecting characteristics onto the source plane (solid lines). As one may expect, the mapping of each of the connecting characteristics between an attractor and a repellor is a loop on the source

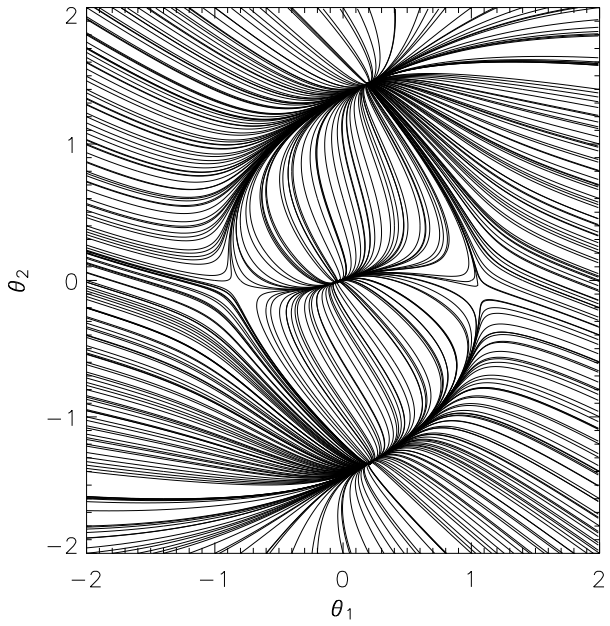

Figure 7.4: The characteristic fields of the toy potential model. The attractors are associated with images that are time delay minima/maxima and the repellors are associated with time delay saddles.

plane that is tangent to the astroid caustic curve due to the connecting characteristics intersecting the outer critical curve.

In addition to the characteristic curves, the intensity deficit is required for potential correction in equation (7.5). To get the intensity deficit defined in equation (7.1) for the pixels on the image plane, first we use the perturbed potential model, the lens equation (2.3), and the original source intensity distribution to get $I(\vec{\beta})$, then we subtract it from $I(\vec{\theta})$ obtained from the original potential. Figure 7.5 shows the initial intensity deficit and the initial potential perturbation ($\delta\psi(\vec{\theta})$ in equation (7.2)) before the perturbative and iterative potential correction, in the top left-hand and bottom left-hand panels, respectively. We use plots of $\delta\psi(\vec{\theta})$ to check that the perturbation approaches zero after corrections.

In each potential reconstruction iteration, we use the current perturbed potential model to obtain the intensity deficit ($\delta I(\vec{\theta})$) and the source intensity gradient ($\left|\frac{\partial I(\vec{\beta})}{\partial \vec{\beta}}\right|$) at every pixel on the image plane; we then use equation (7.5) to correct the perturbed potential by integrating along the characteristic curves of the original potential model. Two iterations are performed and the resulting intensity deficit and potential perturbation after each

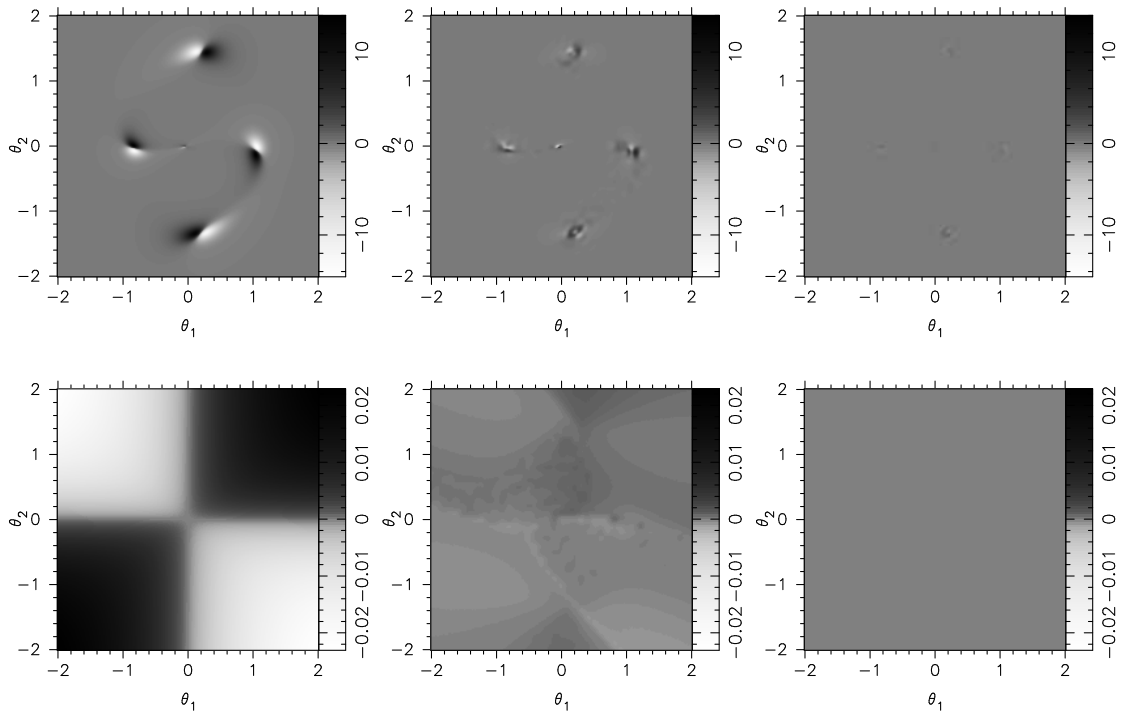

Figure 7.5: Top row, left to right: the intensity deficit before potential correction, after 1 iteration and after 2 iterations of potential correction. The maximum initial intensity deficit (top left-hand panel) is 14 near the image positions (the peak nuclear source intensity is 100). Bottom row, left to right: potential perturbation before correction, after 1 iteration and after 2 iterations of correction. The initial potential perturbation magnitude (bottom left-hand panel) is on average around 0.5% of the original potential. Since the potential is determined up to an arbitrary constant, the potential perturbation is plotted with respect to the mean to enhance small scale features. The plotting scales of the middle and right-hand panels (after corrections) are the same as the left-hand panels (before corrections) for comparison.

iteration are shown in figure 7.5. The middle and right-hand panels show the intensity deficit (potential perturbation) in the top (bottom) after 1 and 2 iterations, respectively. The middle and right-hand panels are plotted on the same scales as that in the left-hand panels. Comparing the right-hand panels to the left-hand panels, the intensity deficit and potential perturbation converge to zero after two iterations (apart from numerical error), signifying that the method of potential reconstruction along characteristics works in theory with perfect data.

A possible limitation to this method is that the intensity deficit needs to be zero at the image locations; otherwise, according to equation (7.5), the integrand diverges at the image locations, which are the end points of integration. For the example above, we are saved from this divergence by discretizing the image plane and thus only reaching the image points within some tolerance, but never ending at the image (divergent) points. The potential correction is most significant near the image points for any nonzero intensity deficit in the region. Therefore, integrating along the characteristics may place limitations on the magnitude of potential perturbation that we can correct, which we discuss in the following paragraph.

This method of potential reconstruction works only for small potential perturbations like the example we considered where the perturbation magnitude is on average (over the image grid) 0.5% of the original potential. By increasing the rotation of the original potential distribution to get the perturbed potential (that is, increasing the perturbation), we require more iterations for convergence, as expected. When the rotation of the original potential gets to $\sim$4.5 degrees, which corresponds to an average potential perturbation magnitude of $\sim$1.5%, the method ceases to converge. Therefore, the method of potential correction by integrating equation (7.5) along characteristics works in theory with perfect data with a small ($\lesssim$1%) potential model error. Therefore, this method is not, in practice, useful. In section 7.3.2, a more robust algorithm for potential correction based on equation (7.4) will be presented.

The example toy model considered provides a practical insight into the theory of potential reconstruction. In reality, we do not have useful data everywhere due to the presence of noise; for an extended source, we can observe emission in an Einstein ring connecting the four images. Based on the analysis of this section, the Einstein ring must be large enough to enclose the connecting characteristics in order to obtain proper potential offsets between

the images. This condition must hold for any potential reconstruction algorithm based on equation (7.4).

7.3.2 Potential Reconstruction Using Matrices

In this section, we investigate an alternative method of solving equation (7.4) for the perturbation $\delta\psi(\vec{\theta})$. Instead of integrating along the characteristics of the differential equation, we cast equation (7.4) into a matrix equation and invert the linear system. We also lift the assumptions on the source intensity distribution that were imposed in section 7.3.1 and solve for the source intensity given the lens potential using the method in section 4.1. The use of matrix equations for potential reconstruction was also studied by Koopmans (2005). The work we present here is similar to that in Koopmans (2005) but differs from Koopmans (2005) in numerical details and our use of Bayesian analysis. To recap the potential reconstruction method, for a given initial lens potential, we reconstruct the source intensity distribution based on section 4.1 to obtain the source intensity gradient, we solve equation (7.4) for the perturbative correction $\delta\psi(\vec{\theta})$, and we re-iterate using the corrected potential.

To write equation (7.4) in a matrix form, we discretize the lens potential on a rectangular grid of $N_{\rm p}$ pixels (which is in general smaller than the number of data pixels $N_{\rm d}$) and denote the potential perturbation by $\delta\psi_i$ where $i = 1, \ldots, N_{\rm p}$. The intensity deficit on the image grid is $\delta I_j = d_j - \mathsf{f}_{ji} s_i$ where $j = 1, \ldots, N_{\rm d}$ (using the notation from section 4.1, $\boldsymbol{d}$, $\mathbf{f}$ and $\boldsymbol{s}$ are the data vector, the blurred lensing operator, and the source intensity vector, respectively). Equation (7.4) now becomes

$$\boldsymbol{\delta I} = \mathbf{t}\boldsymbol{\delta\psi} + \boldsymbol{n}, \tag{7.10}$$

where $\mathbf{t}$ is a $N_{\rm d} \times N_{\rm p}$ matrix which incorporates the PSF, the source intensity gradient, and the gradient operator that acts on $\boldsymbol{\delta\psi}$ (see appendix C for the explicit form of $\mathbf{t}$), and $\boldsymbol{n}$ is the noise in the data. The above equation is equivalent to

$$\boldsymbol{d} = \mathbf{f}\boldsymbol{s} + \mathbf{t}\boldsymbol{\delta\psi} + \boldsymbol{n}. \tag{7.11}$$

Equation (7.11) is in the same form as equation (3.1), provided we have already solved for the source intensity distribution. Therefore, we can apply the same Bayesian regularized

inversion method in chapter 3 to solve for the most probable $\boldsymbol{\delta\psi}$ given the inverted source intensity ($\boldsymbol{s}$) and the lens potential model (encoded in mapping matrix $\mathbf{f}$), both of which appear implicitly in the matrix $\mathbf{t}$. In particular, equations (3.2), (3.3), (3.4), (3.5), (3.8), (3.9), (3.10), (3.13), (3.19), and (3.20) are directly applicable as long as $\boldsymbol{d}$ is replaced by $\boldsymbol{\delta I}$, $N_{\rm s}$ is replaced by $N_{\rm p}$, $\mathbf{f}$ is replaced by $\mathbf{t}$, and $\boldsymbol{s}$ is replaced by $\boldsymbol{\delta\psi}$ (except in $\boldsymbol{\delta I}$). We include the jerk form of regularization (third-order derivative, with an explicit expression for the regularizing function in appendix A) in addition to the zeroth, gradient and curvature forms since the lens potential should in general be smooth, being the *integral* of the surface mass density. We denote the regularization constant as μ (instead of λ that is used in the source intensity reconstruction); we distinguish the forms of regularization for the potential ($\mathbf{g}_{\delta\psi}$) from those for the source intensity ($\mathbf{g}_{\rm S}$) using subscripts. These replacements and new notations give us expressions for the likelihood $P(\boldsymbol{d}|\boldsymbol{\delta\psi},\mathbf{t},\boldsymbol{s},\mathbf{f},\mathbf{g}_{\rm S},\lambda)$, prior $P(\boldsymbol{\delta\psi}|\mathbf{g}_{\delta\psi},\mu)$, posterior $P(\boldsymbol{\delta\psi}|\boldsymbol{d},\mathbf{t},\boldsymbol{s},\mathbf{f},\mathbf{g}_{\rm S},\lambda,\mathbf{g}_{\delta\psi},\mu)$, optimal regularization constant $\hat{\mu}$, evidence $P(\boldsymbol{d}|\mathbf{t},\boldsymbol{s},\mathbf{f},\mathbf{g}_{\rm S},\lambda,\mathbf{g}_{\delta\psi},\mu)$, and most probable solution $\boldsymbol{\delta\psi}_{\rm MP}$. Since these expressions are analogous to the ones in chapter 3, they will not be explicitly written here.

Solving for the potential perturbations is very similar to solving for the source intensity distribution (4.1) except for the following technical details:

1. In each iteration, the perturbative potential correction is obtained only in an annular region instead of the entire lens potential grid. The value of $N_{\rm p}$ is therefore the number of pixels within the annular reconstruction region. The reason is that source intensity gradients are needed to correct for the lens potential (see equation (7.4)). Since the extended source intensity distribution is usually only lensed into an Einstein ring, we only have information about source intensity gradients in this region and hence can only correct for the potential in an annulus. The determining factor for the size and shape of the annular region hinges on the choice for the source intensity grid because the annular region corresponds to the lensing of the source reconstruction region onto the image plane. The source region has been chosen to enclose the source intensity distribution with minimal number of source pixels (for computational efficiency) yet having sufficient resolution for modeling the source. Since source intensity gradients are only obtained on the chosen source grid, only the annular region on the image plane has source intensity gradient values. The annulus of potential corrections ob-

tained at each iteration is extrapolated for the next iteration. In addition, The forms of regularization matrix, as discussed in appendix A, are modified accordingly to take into account the nonrectangular reconstruction region (described in more detail in the third point below).

2. Since equation (7.11) is a perturbative equation in $\boldsymbol{\delta\psi}$, the inversion needs to be *overregularized* to enforce a small correction in each iteration. As the iterative correction proceeds and the potential gets closer to the true potential, overregularization becomes less important. Currently there is no objective way to set the overregularization factor. Empirically, we set the regularization constant, μ, at roughly the peak of the function $\mu E_{\delta\psi}$ (within a factor of 10), which corresponds to the value before which the prior overly dominates. The peak value remains approximately constant (within a factor of 10) for the multiple iterations of a given data set and model, so we use the value of μ from the zeroth iteration for all iterations.

3. The potential corrections are generally nonzero at the edge of the annular reconstruction region (whereas for the source reconstruction, the source grid is chosen such that it encloses the entire extended source intensity distribution with the edge pixels having nearly zero intensities). This calls for slightly different structures of regularization compared to those written in appendix A for source intensity reconstruction. The regularizations are still based on derivatives of $\boldsymbol{\delta\psi}$; however, no patching with lower derivatives should be used for the edge pixels because the zeroth-order regularization at the top/right edge will incorrectly enforce the $\boldsymbol{\delta\psi}$ values to zero in those areas. The absence of the lower derivative patches leads to a singular regularization matrix,[1] which is problematic for evaluating the Bayesian evidence for lens potential correction. To circumvent this, we will use the patched regularization matrix to get the order of magnitude of the "optimal" regularization constant μ, but use the unpatched regularization matrix in solving for $\boldsymbol{\delta\psi}$ values. Since the inversion for obtaining the $\boldsymbol{\delta\psi}$ values needs to be overregularized to keep the corrections small, we do not need an exact "optimal" regularization constant but only an approximate value. We have found the revised structure of regularization for potential corrections to work for

[1]Having a singular regularization matrix ($\mathbf{C}$) does not prohibit the $\boldsymbol{\delta\psi}$ inversion because the matrix for inversion ($\mathbf{A} = \mathbf{B} + \mu\mathbf{C}$, see section 3.1) is in general nonsingular.

various types of sources (with varying sizes, shapes, number of components, etc.).

In the source reconstruction steps of this this iterative scheme, we discover that overregularizing the source reconstruction in early iterations helps with the convergence, especially if the error in the starting potential is large. This is because initial potentials that are significantly perturbed from the true potential often lead to highly discontinuous source distributions, and overregularization would give a more regularized source intensity gradient for the potential correction. Unfortunately, we do not have an objective way of setting this overregularization factor for the source reconstruction. Currently, at each source reconstruction iteration, we set the overregularization factor such that the magnitude of the intensity deficit is at approximately the same level but with a smoother source intensity distribution for numerical derivatives. For initial regularization values of $\sim$10–100, this factor can be $\sim$1–1000, depending on the amount of initial potential perturbation. This scheme ensures that we do not overregularize when we are close to the true potential. Overregularizing in this case would lead to a significant increase in the intensity deficit, and would thus give a false signal that the potential is not close to the true potential. Based on simulated test runs, the recovery of the original potential depends on the amount of overregularization. With a large amount of initial potential perturbation, overregularization at the beginning iterations is crucial for convergence. We find that it is better to overregularize in excess than in deficit. Too much overregularization simply takes more iterations to converge, where as too little overregularization may not converge at all.

In the iterative process, there can be iterations when some source pixels are not mapped by that iteration's lens potential on the data grid. In such cases, we mask out these unmapped source pixels, and redefine the regularization matrix so that we patch the right-most and top-most pixels (pixels adjacent to the edge or adjacent to the unmapped source pixels) with lower derivatives just as we did for the edge pixels in appendix A. We also mask out any pixels that have no neighboring pixels in the reconstruction region so that we can compute numerical derivatives for all pixels inside the reconstruction region.

Due to the use of merely the isophotes of the lensed source intensity distribution (and no external information on the lens system), the potential correction we obtain at each iteration may be affected by the mass-sheet degeneracy. The description of the mass-sheet degeneracy was given in section 2.1.2, and here we review a few key points that are relevant

for the potential corrections. In essence, an arbitrary symmetric paraboloid, gradient sheet, and constant can be added to the potential without changing the predicted lensed image:

$$\psi_\nu(\vec{\theta}) = \frac{1-\nu}{2}|\vec{\theta}|^2 + \vec{a}\cdot\vec{\theta} + c + \nu\psi(\vec{\theta}), \tag{7.12}$$

where ν, $\vec{a}$, and c are constants. This is equation (2.12) with λ replaced by ν. The constants $\vec{a}$ and c have no physical effects on the lens systems as they merely change the origin on the source plane (which is unknowable) and change the zero-point of the potential (which is not observable). However, the parameter ν changes the mass profile of the lens systems and the relative time delay between the images ($\Delta T_\nu \sim \nu\Delta T$). Gravitational lensing alone cannot break the mass-sheet degeneracy (i.e., determine a unique value of ν); additional information, for examples, on the stellar dynamics of the lens galaxies and galaxy group environments, are needed to break the degeneracy. In the pixelated perturbative correction scheme, the reconstructed potential may drift away from the true potential due to the mass-sheet degeneracy. It would be ideal to make sure we remain "close" to the initial starting model because its mass sheet may have already been determined using, for example, stellar dynamics. To accomplish this, we set $\nu = 1$ and fix three points in the corrected potential after each iteration to the corresponding values of the initial potential. Setting $\nu = 1$ ensures that the size of the extended source intensity remains approximately the same, and the three fixed points allow us to solve for $\vec{a}$ and c in equation (7.12) to remove irrelevant gradient sheets and constants in the reconstructed potential. We choose the three points to be three of the four (top, left, right, and bottom) locations of the annular reconstruction region that are midway in thickness between the annular edges. The three points are usually chosen to be at places with lower surface brightness in the ring. This technique of "fixing" the mass-sheet degeneracy is demonstrated in the examples below using simulated data.

In addition to fixing the three points, we can use the relative time delay as constraints on the potential to keep it close to the initial model. Given the redshifts of the lens and the source, and the predicted H_0 from the initial model, we can transform the time delay constraints to Fermat potential constraints. The Fermat potential difference between images i and B (assume that image B is the first image to vary, which is the case for B1608+656) is

$$\phi_{iB} = \frac{1}{2}\left(\vec{\theta}_i - \vec{\beta}_i\right)^2 - \frac{1}{2}\left(\vec{\theta}_B - \vec{\beta}_B\right)^2 - (\psi_i - \psi_B), \tag{7.13}$$

where $i = A, C, D$ for a quadruply imaged system. Since the multiple lensed images come from the same source, we choose, arbitrarily, the source position of image A to be the position of all other images. Using the lens equation for $\vec{\beta}_A$, equation (7.13) becomes

$$\phi_{iB} = \frac{1}{2}\left(\vec{\theta}_i - \vec{\theta}_A\right)^2 - \frac{1}{2}\left(\vec{\theta}_B - \vec{\theta}_A\right)^2 + \left(\vec{\theta}_i - \vec{\theta}_B\right) \cdot \vec{\nabla}\psi_A - \psi_i + \psi_B. \tag{7.14}$$

Expanding ψ to first order using equation (7.2), substituting into equation (7.14), and including noise in the measurement, we get the following equation

$$(\phi_{iB})_{\rm data} = (\phi_{iB})_0 = \phi_{iB} - (\vec{\theta}_i - \vec{\theta}_B) \cdot \vec{\nabla}\delta\psi_A + \delta\psi_i - \delta\psi_B + n_{\phi_i}, \tag{7.15}$$

where $(\phi_{iB})_{\rm data}$ is the observed Fermat potential difference (that must equal to the Fermat potential difference using the true potential ψ_0 by definition) and n_{ϕ_i} is the noise in the measurement of Fermat potential differences (from the relative time delays). For $N_{\rm image}$ of multiple images, we have $N_{\rm image} - 1$ constraints equations in the form of (7.15) on the potential perturbations $\delta\psi$. Given the covariance matrix from the Fermat potential differences (derivable from the relative time delay covariance matrix), we can include the equation (7.15) into our system of equations for $\delta\psi$ (7.11) to solve for $\delta\psi$ in each iteration of potential correction. Enforcing these constraints (equation (7.15)) would keep us close to the H_0 value from the initial model, and any discrepancy in the predicted H_0 values from the different relative time delay pairs gives us an estimate on the error associated with the lens modeling (see chapter 8). We can quantify the discrepancy by evaluation $\chi^2_\phi \equiv [(\boldsymbol{\phi}_B)_{\rm data} - \boldsymbol{\phi}_B]^{\rm T} \mathbf{C}_{\boldsymbol{\phi}}^{-1} [(\boldsymbol{\phi}_B)_{\rm data} - (\boldsymbol{\phi}_B]$, where $\mathbf{C}_{\boldsymbol{\phi}}$ is the covariance matrix for the noise in the relative Fermat potential (time delay) measurements. We stress that this potential reconstruction method cannot on its own determine the value of the H_0 due to the mass-sheet degeneracy. What this method delivers is an accurate lens potential up to an unknown mass sheet (that can only be determined from external information such as stellar dynamics) by using all available information from the entire Einstein ring.

To summarize, the steps for the iterative and perturbative potential reconstruction scheme via matrices are: (i) reconstruct the source intensity distribution given the initial (or corrected) lens potential based on section 4.1. (ii) Compute the intensity deficit and the source intensity gradient. (iii) Solve equation (7.11) for the potential corrections $\boldsymbol{\delta\psi}$ in

the annulus of reconstruction (with or without the additional time delay constraints from equation (7.15)). (iv) Update the current potential using equation (7.2): $\boldsymbol{\psi}_{\text{next iteration}} = \boldsymbol{\psi}_{\text{current iteration}} - \boldsymbol{\delta\psi}$. (v) Transform the corrected potential $\boldsymbol{\psi}_{\text{next iteration}}$ via equation (7.12) so that $\nu = 1$ and the transformed corrected potential has the same values as the initial potential at the three fixed points. (vi) Extrapolate the transformed corrected potential for the next iteration. (vii) Interpolate the transformed corrected potential onto the resolution of the data grid for next iteration's source reconstruction. (viii) Repeat the process using the extrapolated and finely gridded reconstructed potential with the mass sheet fixed, and stop the process when the intensity deficit is negligible compared to the noise level.

7.3.3 Demonstration: Potential Perturbation due to a Dark-Mass Clump

Simulated Data

As in sections 4.2 and 4.3, we use SIE potentials to test the potential reconstruction method. SIEs are good because they are analytic models (e.g., Kormann et al. 1994) that can well describe quadruply imaged systems. For this demonstration, we let the lens be comprised of two SIEs at the same redshift $z_d = 0.3$: a main component and a perturber. The main lens has an one-dimensional velocity dispersion of 260 km s^{-1}, axis ratio of 0.75, and semimajor axis position angle of 45 degrees (from vertical in counterclockwise direction). The (arbitrary) origin of the coordinates is set such that the lens is centered at $(2.5'', 2.5'')$, the center of the $5'' \times 5''$ image. The perturbing SIE is centered at $(3.8'', 2.5'')$ with a velocity dispersion of 50 km s^{-1}, axis ratio of 0.60, and semimajor axis position angle of 70 degrees. The exact potential is the sum of these two SIEs. We model the source intensity as an elliptical distribution inside the caustics at $z_s = 3.0$ with an extended component (of peak intensity of 1.0 in arbitrary units) and a central point source (of intensity 3.0). This source is chosen such that the lensed image resembles B1608+656. We use 30×30 source pixels each of size $0.025''$, 100×100 image pixels each of size $0.05''$, and 25×25 potential pixels each of size $0.2''$. To obtain the simulated data, we map the source intensity distribution to the image plane using the exact lens potential and the lens equation, convolve the lensed image with the a Gaussian PSF whose FWHM $= 0.15''$ and add Gaussian noise of variance 0.042. Figure 7.6 shows the simulated source in the left-hand panel and the simulated

noisy data image in the right-hand panel. The Fermat potential difference between the images are listed in table 7.1. The images were labeled by A, B, C, D, and their locations are $(1.78'', 1.03'')$, $(3.88'', 3.63'')$, $(3.53'', 1.28'')$, and $(1.33'', 3.38'')$, respectively. We set the measurement error to be Gaussian with variance 0.008, which corresponds to 5% in the pair with the smallest Fermat potential difference.

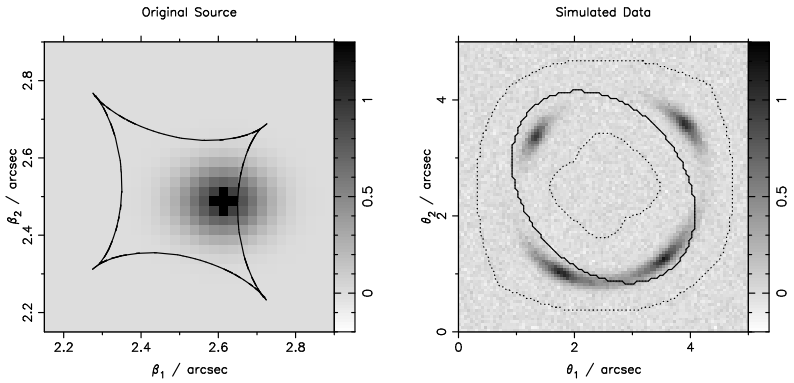

Figure 7.6: Demonstration of potential reconstruction: simulated data. The left-hand panel: The simulated source intensity distribution with an extended component (of peak intensity of 1.0 in arbitrary units) and a central point source (of intensity 3.0) on a 30×30 grid. The solid curves are the astroid caustics of the initial perturbed potential that consists of only the main SIE. The right-hand panel: The simulated image of the source intensity distribution on the left using the unperturbed potential consisting of two SIEs (after convolution with Gaussian PSF and addition of noise, as described in the text). The solid line is the critical curve of the initial perturbed potential, and the dotted lines mark the annular region where the source grid maps using the mapping matrix $\mathbf{f}$.

Table 7.1: The relative Fermat potential between the four images of the original potential and the reconstructed potential for a few selected iterations

	true values and adopted errors	initial potential	iteration=0	iteration=2	iteration=8
ϕ_{AB}	0.161 ± 0.008	0.049	0.187	0.171	0.166
ϕ_{CB}	0.270 ± 0.008	0.118	0.251	0.254	0.255
ϕ_{DB}	0.429 ± 0.008	0.421	0.521	0.467	0.444
χ^2_ϕ	–	553	145	29.1	7.06

Note. — The image positions are labeled by A, B, C, and D, and their values are $(1.78'', 1.03'')$, $(3.88'', 3.63'')$, $(3.53'', 1.28'')$, and $(1.33'', 3.38'')$, respectively.

Iterative and Perturbative Potential Corrections

We take the initial (perturbed) potential to be the main SIE component (a typical scenario where the perturbing SIE is faint/dark and is not incorporated in the initial model) but with the position angle changed from 45 to 40 degrees. Figure 7.7 shows the plot of the initial potential model (without the SIE perturber) in the left-hand panel, the potential perturbation in the middle panel, and the percentage error that the perturber constitutes (absolute valued) in the right-hand panel. In this plot, the initial potential has a constant gradient plane and offset added such that the top, left and bottom midpoints in the annulus are fixed to the true potential with zero potential perturbation (as described in the passage following equation (7.12)).

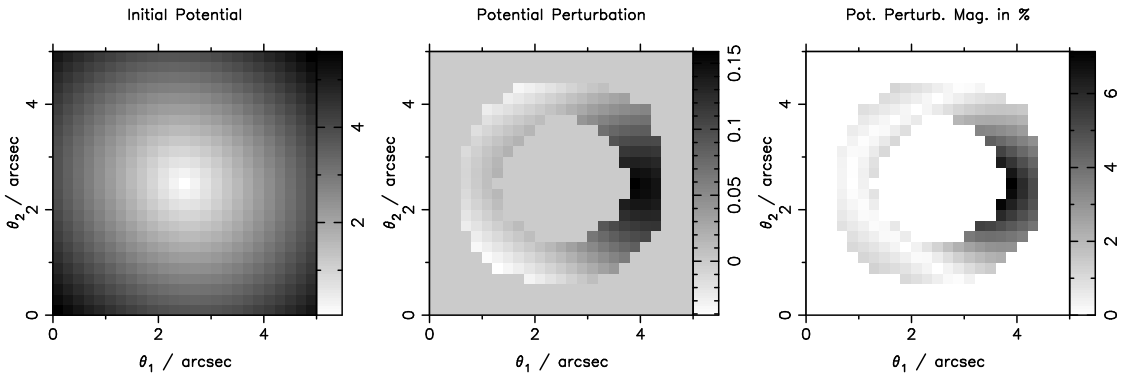

Figure 7.7: Demonstration of potential reconstruction: the potential model and perturbation. The left-hand panel: The initial perturbed SIE potential model. The middle panel: the potential perturbation due to the smaller SIE in the annular reconstruction region (which maps to the source grid). The right-hand panel: the magnitude of the potential perturbation in percentage.

We perform 9 iterations of the perturbative potential correction method outlined in this section. We impose the Fermat potential difference constraints in each iteration of the potential corrections. The iterations are labeled from 0 to 8. For each source reconstruction iteration, we assert the curvature type of regularization and use the source intensity reconstruction for the evaluation of the source intensity gradients that are needed for the potential correction. The source inversions are overregularized, especially in early iterations, and the overregularization factors (that is multiplied by the optimal regularization constant determined by maximizing the evidence) are listed in table 7.2. These values were

set to obtain a smooth source reconstruction (for evaluation of gradients) without causing significant increases in the intensity deficit. For each potential correction iteration, we try two forms of regularization (curvature and jerk) and pick the one that gives the highest evidence. Curvature and jerk regularizations will ensure that the potential reconstructions are smooth to second order for the evaluation of the surface mass density (which is half the Laplacian of the lens potential). We set the regularization constant for the potential reconstruction to be 10× the value of μ where $\mu E_{\delta\psi}$ peaks in iteration=0. The regularization value is $\sim 6 \times 10^6$ and is used for all subsequent iterations (since we find that the peak in $\mu E_{\delta\psi}$ changes little as the iterations proceeds). For comparison, the 'optimal' regularization constant is $\sim 5 \times 10^1$ at iteration=0; therefore, the potential reconstruction inversions are heavily overregularized to keep the corrections to first order. We show figures of source reconstructions and potential corrections for some, but not all, of the iterations. For clarity, we denote SI as a source reconstruction iteration and PI as a potential correction iteration.

Figure 7.8 shows the results of the source reconstruction and potential correction in iteration=0. For SI=0, we find that the source needs to be overregularized by a factor of 10^4 to get a smooth reconstruction (for the intensity gradient calculation) that is shown in the top middle panel. The reconstructed source does not resemble the original source and the intensity deficit (top right-hand panel) shows prominent arc features due to the presence of the potential perturbation. As a comparison, figure 7.9 shows the optimally regularized source reconstruction and its corresponding intensity deficit. The source in this case is extremely noisy due to the mismatch in the four copies of the mapped source based on the perturbed potential. Such a reconstruction, with bad numerical derivatives, leads to instabilities in the iterative potential reconstructions and thus justifies our overregularizing the source reconstruction. Using the source intensity gradients and the intensity deficit in the top panels in figure 7.8, we get the PI=0 results of $\boldsymbol{\delta\psi}$ in the bottom panels. We find the jerk regularization is preferred to the curvature regularization, with a higher evidence value at the peak of the $\mu E_{\delta\psi}$ (see table 7.2). The reconstructed $\boldsymbol{\delta\psi}$ in the bottom middle panel is of same structures as the exact $\boldsymbol{\delta\psi}$ in the bottom left-hand panel, though the magnitude is smaller due to the correction being a perturbative one. The potential perturbations here have the top, middle and bottom midpoints in the annulus fixed to zero (i.e., the perturbed potential have these three points fixed to the initial model) to remove the constant gradient and offset. For comparison, figure 7.10 shows the exact and the reconstructed potential per-

turbations without these three points fixed. Due to the presence of a constant gradient and offset, the reconstructed potential perturbation in the middle panel now does not resemble the exact potential perturbation in the left-hand panel. This illustrates the need for fixing the three points in the annulus, which we do in all iterations of $\boldsymbol{\delta\psi}$ corrections. A plot of the image residual after correction ($= \boldsymbol{\delta I} - \mathbf{t}\boldsymbol{\delta\psi}$) continues to show arc features though less prominent than in the top right-hand panel in figure 7.8. The same image residual plot with the true potential perturbation also shows similar arc features, which indicates that equation (7.4) is indeed a perturbative equation and thus justifies the overregularization in the potential correction step. Table 7.1 lists the predicted Fermat potential differences between the images of the initial and the corrected potential model. The corrected potential agrees better with the truth ($\chi^2_\phi = 145$) than the initial model ($\chi^2_\phi = 553$) but it does not yet agree within the errors with significant potential perturbation remaining.

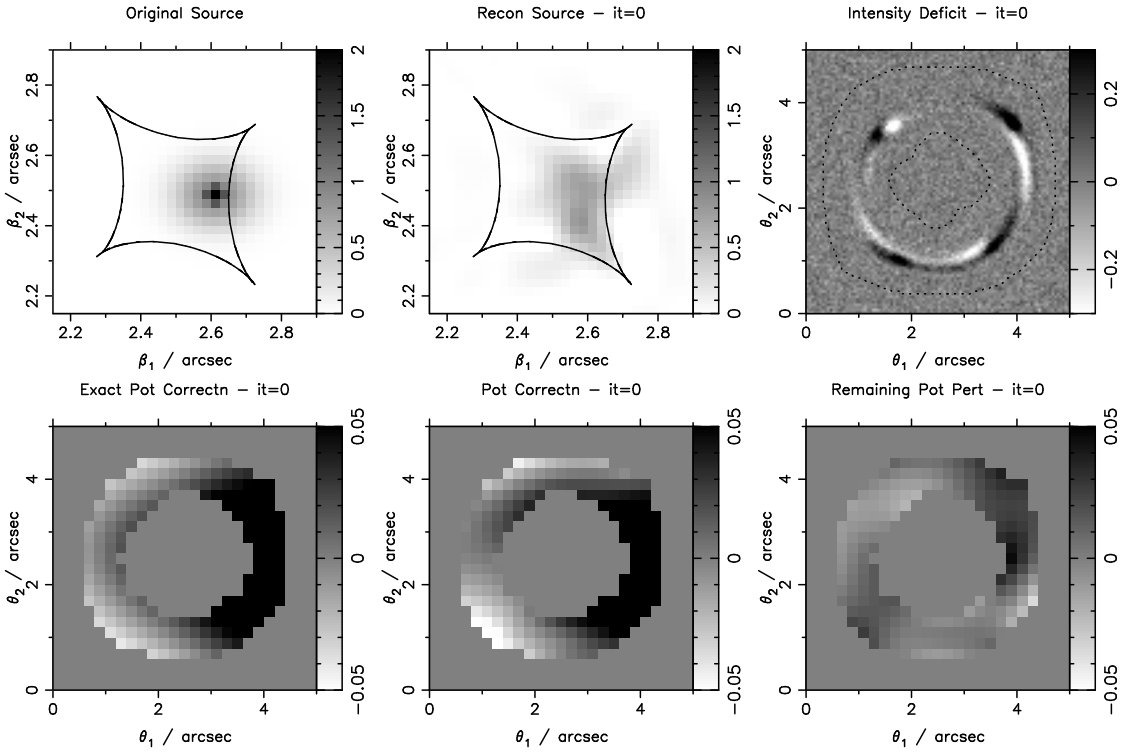

Figure 7.8: Demonstration of potential reconstruction: results of the iteration=0 of source intensity reconstruction (SI=0) and potential correction (PI=0). Top row: the left-hand panel shows the original source for comparison, the middle panel shows the reconstructed source intensity using curvature regularization that is overregularized by a factor of 10^4 to ensure a smooth resulting source for evalution of the gradients, and the right-hand panel shows the intensity deficit (difference between the simulated image and the predicted image from the reconstructed source in middle panel). The caustic curves in solid are those of the initial perturbed potential. Due to the presence of potential perturbation, the reconstructed source does not resemble the original source, but is localized due to overregularization. The prominent arc features are due to the potential perturbation. Bottom row: the left-hand panel shows the exact $\boldsymbol{\delta\psi}$ to be corrected, the middle panel shows the reconstructed $\boldsymbol{\delta\psi}$ using the source intensity gradients and intensity deficit from the top row, and the right-hand panel is the difference between the two. The potential perturbations have the top, left and bottom midpoints in the annulus fixed to the initial model. The reconstructed $\boldsymbol{\delta\psi}$ in the middle panel has similar form as the exact $\boldsymbol{\delta\psi}$; the magnitude of reconstruction is smaller due to overregularization to keep the corrections to first order.

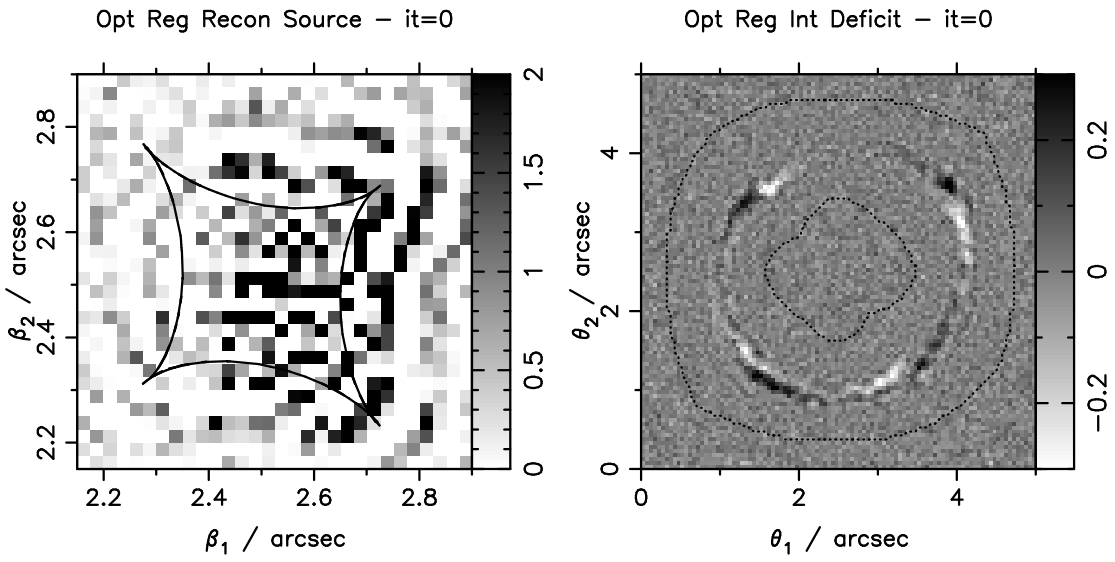

Figure 7.9: Demonstration of potential reconstruction: results of iteration=0 of optimally regularized source reconstruction (SI=0) using curvature regularization. Left-hand panel: the reconstructed source that is optimally regularized using curvature regularization. The source is very noisy due to the presence of the potential perturbation, and creates instabilities in the potential reconstruction technique. This demonstrates the need to overregularize the source inversions, especially in early iterations. Right-hand panel: the intensity deficit that results from the source in the left-hand panel.

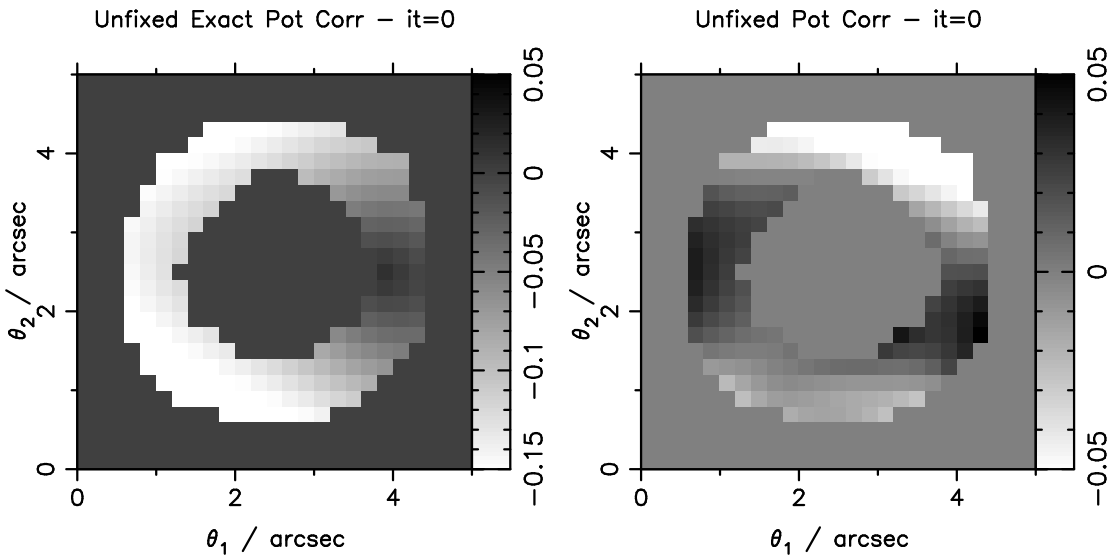

Figure 7.10: Demonstration of potential reconstruction: results of iteration=0 of potential correction (PI=0) without fixing three points to initial model. Left-hand panel: the exact potential perturbation to be corrected. Right-hand panel: the reconstructed potential perturbation without three points in the top, left and bottom parts of annulus fixed to zero. Due to the presence of a constant gradient and offset (which have no physical significance), the reconstructed potential perturbation does not resemble the true potential perturbation.

Table 7.2: Demonstration of potential reconstruction: regularization types and values for source intensity and potential reconstructions

Iteration	Reg. Type	Reg. Val	Overreg. factor	Evidence
0/SrRec	curv	0.049	10^4	–
0/PotRec	curv	6.1×10^6	10.	1.1×10^2
	jerk	6.1×10^6	10.	3.5×10^2
1/SrRec	curv	4.7	10.	–
1/PotRec	jerk	6.1×10^6	10.	–
2/SrRec	curv	15.	1.	–
2/PotRec	jerk	6.1×10^6	10.	–
3/SrRec	curv	17.	1.	–
3/PotRec	curv	6.1×10^6	10.	–
4/SrRec	curv	18.	1.	–
4/PotRec	curv	6.1×10^6	10.	–
5/SrRec	curv	19.	1.	–
5/PotRec	curv	6.1×10^6	10.	–
6/SrRec	curv	20.	1.	–
6/PotRec	curv	6.1×10^6	10.	–
7/SrRec	curv	21.	1.	–
7/PotRec	curv	6.1×10^6	10.	–
8/SrRec	curv	22.	1.	–
8/PotRec	curv	6.1×10^6	10.	–

Note. — The first column denotes the iteration number for either the source intensity inversion or potential correction. The second to fifth column shows the type of regularization used, the regularization value (from maximizing the evidence for source reconstruction and from peak of $\mu E_{\delta\psi}$ for potential correction), the overregularization factor, and the evidence when it is relevant for regularization comparison. For iteration=0, we show the evidence values for the two forms of regularization in potential reconstruction for comparison. For higher iterations, we only list the selected form of regularization and thus omit the evidence values. The regularization constants in the source intensity reconstructions increase with iterations, indicating that the prior is becoming more relevant as we correct the perturbed potential. With high amounts of potential perturbation in early iterations, the likelihood overwhelms the prior.

After two more iterations, we have the reconstructed source in the top middle panel better resembling the original source in the top left-hand panel of figure 7.11. Only a small trace of misfit is visible in the intensity deficit in the top right-hand panel, signaling that we are getting close to the true potential. The source intensity gradients and the intensity deficit allow us to compute the potential correction, shown in the bottom middle panel, using the jerk form of regularization. The bottom left-hand panel is the exact amount of perturbation left to be corrected before this iteration, and the bottom right-hand panel shows the amount of perturbation that remains after correction. The amount of potential perturbation remaining is closer to zero compared to figure 7.8, which is a sign that the iterative method is converging. Table 7.1 shows that the predicted relative Fermat potential between the images after iteration=2 are not yet agreeing with the true values within the errors, but are in better agreement than in iteration=0.

Figure 7.12 shows the results of iteration=8, the last iteration. The source is faithfully recovered in the top middle panel, resulting in negligible intensity deficit in the top right-hand panel. The centroid of the source is slightly shifted compared to the original (the top left-hand panel) because of our fixing the three points in the potential corrections. Constant gradients were added to the potential to keep the three points fixed to the initial potential, and a constant gradient corresponds to a translation in the source plane. Absolute position of the source is irrelevant as we can set the coordinates arbitrarily; it is only the relative positions on the source plane that matter. The source positions are shifted *relative* to the caustic curve because these caustic curves are the ones from the initial perturbed potential (they were not computed for the reconstructed potential due to the low resolution in the reconstructed potential grids). If we were to plot the caustic curve of the corrected potential, we would find no overall shift in the source with respect to the caustic curve. The bottom middle panel shows the potential correction, that is barely visible. At PI=8, the potential corrections are now very small with little intensity deficit left to correct. The bottom right-hand panel shows that most of the initial potential perturbations have been corrected, though there is still some left. This amount of remaining potential perturbation leads to image residuals that are smaller than the noise in the data (hence we see negligible intensity deficit in the top right-hand panel). We have thus reach the limit in the potential correction that is set by noise in the data. The better the data quality (in terms of signal to noise), the better we can reconstruct the potential! The predicted Fermat potential

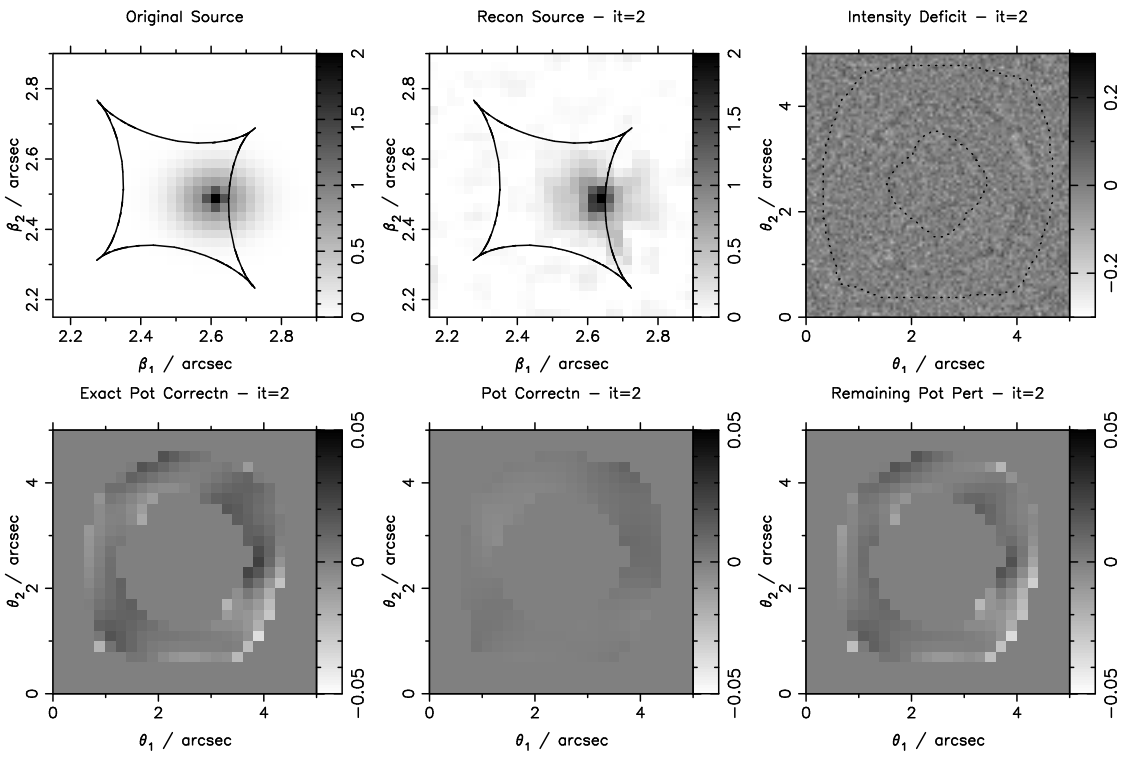

Figure 7.11: Demonstration of potential reconstruction: results of the iteration=2 of source intensity reconstruction (SI=2) and potential correction (PI=2). Top row: the left-hand panel shows the original source for comparison, the middle panel shows the reconstructed source intensity using curvature regularization that is optimally regularized, and the right-hand panel shows the intensity deficit (difference between the simulated image and the predicted image from the reconstructed source in middle panel). The caustic curves in solid are those of the initial perturbed potential. After three iterations of potential corrections, the reconstructed source now resembles the original and no overregularization is needed. There is still visible trace of arc features in the intensity deficit due to remaining potential perturbation. Bottom row: the left-hand panel shows the exact $\boldsymbol{\delta\psi}$ left to be corrected, the middle panel shows the reconstructed $\boldsymbol{\delta\psi}$ using the source intensity gradients and intensity deficit from the top row, and the right-hand panel is the difference between the two. The potential perturbations have the top, left and bottom midpoints in the annulus fixed to the initial model. The reconstructed $\boldsymbol{\delta\psi}$ in the middle panel is smaller in magnitude than in figure 7.8 as we get closer to the true potential.

differences from the corrected potential listed in table 7.1 shows that they agree with the true values within 2 σ uncertainties.

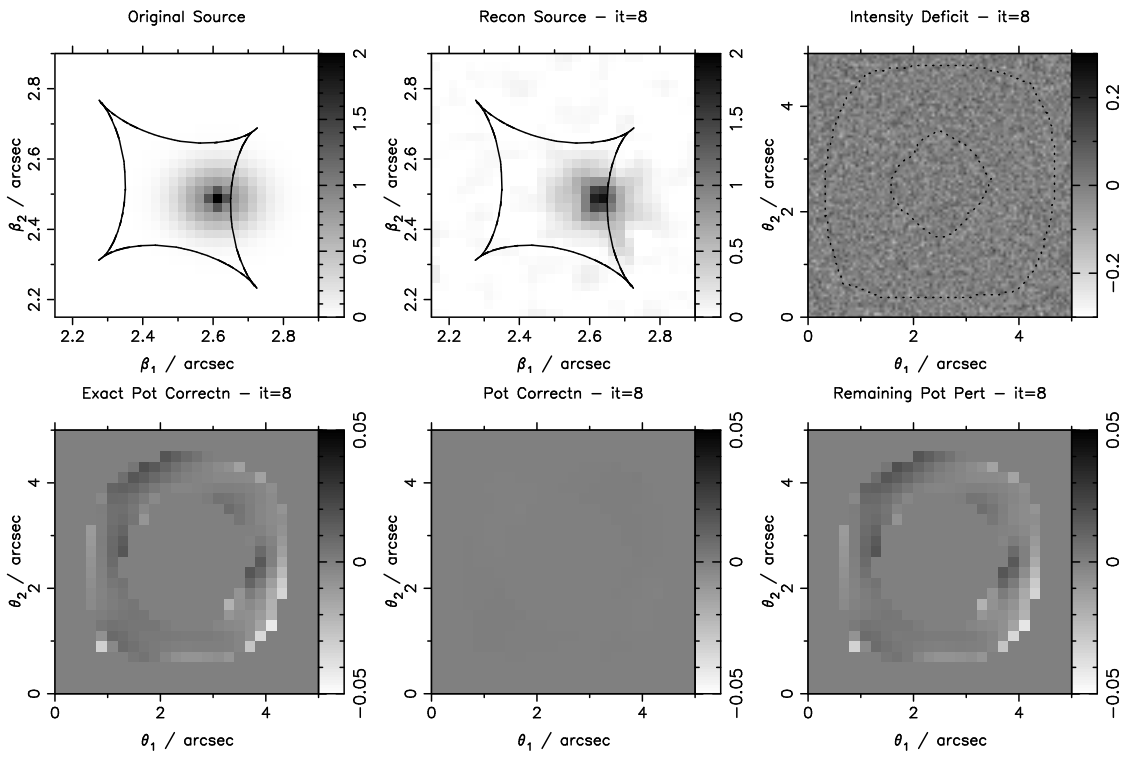

Figure 7.12: Demonstration of potential reconstruction: results of the iteration=8 of source intensity reconstruction (SI=8) and potential correction (PI=8). Top row: the left-hand panel shows the original source for comparison, the middle panel shows the reconstructed source intensity using curvature regularization that is optimally regularized, and the right-hand panel shows the intensity deficit (difference between the simulated image and the predicted image from the reconstructed source in middle panel). The caustic curves in solid are those of the initial perturbed potential. The source has been faithfully reconstructed that results in negligible intensity deficit. Bottom row: the left-hand panel shows the exact $\boldsymbol{\delta\psi}$ left to be corrected before this iteration, the middle panel shows the reconstructed $\boldsymbol{\delta\psi}$ using the source intensity gradients and intensity deficit from the top row, and the right-hand panel is the difference between the two. The potential perturbations have the top, left and bottom midpoints in the annulus fixed to the initial model. Due to the negligible intensity deficit, the reconstructed $\boldsymbol{\delta\psi}$ in the middle panel is barely visible. The remaining potential perturbation, now close to zero, cannot be fully corrected due to the noise in the data.

Discussion

This demonstration shows that the iterative and perturbative potential reconstruction method works in practice. Using simulated data, we find that potential perturbations of $\lesssim$5% are correctable, though the actual amount depends on the amount of overregular-

ization for both the source inversion and potential correction, and on the extendedness of the source intensity distribution. Based on our tests with simulated data, we find it better to overregularize too much than too little. Overregularizing too much will require more iterations to converge, whereas overregularizing too little often leads to no convergence at all. Regarding the size of the source intensity distribution, the more extended a source is, the better we can recover the potential. When the source is extended enough to be lensed into a closed ring, the true potential can be fully recovered (up to the limit set by the noise in the data) from potential corrections based on (7.11) without imposing constraints from the Fermat potential differences. When the source is extended to have about half of the Einstein ring, then the corrected potential without Fermat potential constraints faithfully reproduces the source with negligible intensity deficit, but the relative Fermat potentials may not be recovered due to a slight relative offset in the potential between the images. This is because the 'connecting characteristics' (see section 7.3.1) that fix the potential difference between the images are going through regions without much signal (light of the lensed source). In this case with a moderately extended source, imposing the relative Fermat potential constraints helps us to recover the potential difference between the images in addition to reconstructing the source with minimal image residual. In the case when the source is very compact, even the Fermat potential difference constraints (with errors of $\sim$5%) cannot help keep the potential between images fixed (in other words, the potential reconstruction based on the image intensities is overwhelming the constraints from the Fermat potential differences). Only with extremely accurately ($\lesssim$1% error) measured Fermat potential differences (time delays) can the lens potential be constrained at the images for these not-so-extended sources.

For sources that are small in extent, the potential correction also depends on the points we choose to fix to the initial potential model. Since an isolated image is generally more prone to having its potential be offset relative to the other images, we set two of the three fixed points in the gaps on both sides of the most isolated image, and one point near the connecting images.

In the demonstration, the PSF we used was a Gaussian with width $0.15''$. We find that for a given source size, a more extended PSF would lead to better potential corrections since the PSF would smear and thus connect the isolated image better to the other images. In addition, if we used a different PSF (e.g. of a different width) than the input that was used

to create the simulated data, we would be left with an intensity deficit that would not be correctable by the iterative potential reconstruction method. Therefore, an uncorrectable intensity deficit is a sign that our model of the system (other than the lens potential) is wrong.

The potential grid that we used was 25×25, which we find to be a good balance between the number of degrees of freedom and goodness of fit. An increased number of potential pixels would fit to the images residuals better, but would then be prone to having degenerate solutions. A decreased number of potential pixels would prevent us from correcting the intensity deficit. The Bayesian evidence from the source reconstruction in principle can be used to compare the different potential grids. In general, we find that a potential grid that is $\sim 4\times$ coarser than the image grid works well.

With the potential corrections reconstructed in annular regions only a few pixels (~ 4) thick, the Laplacians of the potentials are dominated by numerical noise. Therefore, the surface mass density perturbations are generally not well reconstructed. This is especially true for iterations > 0 since the potential has been extrapolated for future iterations, and extrapolation such as those minimizing the curvature often leads to discontinuous first derivatives. Nonetheless, for cases where the source is very extended (so that the annular reconstruction region has more pixels in width) the surface mass density from the potential correction in iteration=0 can give us a hint of the surface mass density of the perturber since the potential correction in iteration=0 generally has the highest magnitude of all iterations. This can be useful for detecting substructure around galaxy lenses.

In the next subsection, we apply the iterative potential reconstruction method that has been shown to work on simulated data to the gravitational lens B1608+656.

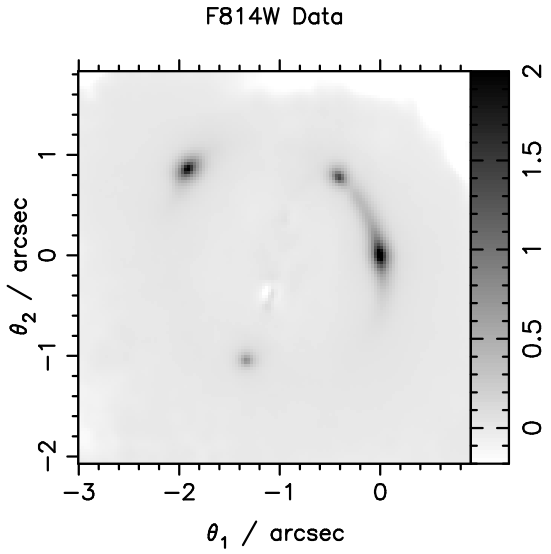

Figure 7.13: Lens galaxy subtracted ACS F814W image based on the PSF, dust and lens galaxies' light of Model 5 in table 6.4 in chapter 6.

7.3.4 Pixelated Lens Potential of B1608+656

ACS Data

In order to apply the pixelated potential reconstruction method to B1608+656, we need to include the effects of dust and lens galaxies' light. Using the same notation as in chapter 6, we write the PSF blurring as the $\mathbf{B}$ matrix, dust extinction as the $\mathbf{K}$ matrix, and lens galaxies' light as the $\boldsymbol{g}$ vector. Equation (7.11) is applicable provided we replace $\boldsymbol{d}$ with $\boldsymbol{d} - \mathbf{B} \cdot \mathbf{K} \cdot \boldsymbol{g}$, $\mathbf{f}$ with $\mathbf{B} \cdot \mathbf{K} \cdot \mathbf{L}$, and include $\mathbf{K}$ into $\mathbf{t}$ (see appendix C for this inclusion). Therefore, given a PSF, a dust, and a lens galaxies' light model, we can iteratively correct for the potential in B1608+656 based on the machinery we developed in previous sections.

For the potential reconstruction, we use a 130×130 cutout of the drizzled ACS/F814W image with pixel size $0.03''$ shown in figure 6.1. For the PSF, dust and lens galaxies' light, we use those of Model 5 in table 6.4 in chapter 6. This model has the highest Bayesian evidence among Models 1 through 8 where there is no mixing in the PSF and dust models. Figure 7.13 shows the galaxy subtracted F814W image ($= \boldsymbol{d} - \mathbf{B} \cdot \mathbf{K} \cdot \boldsymbol{g}$).

Iterative Potential Corrections for B1608+656

For the initial lens potential model, we use the SPLE1+D (isotropic) model in Koopmans et al. (2003b). Given these models and the drizzled image, we perform 16 iterations (labeled as 0 to 15) of pixelated potential corrections on B1608+656. For each iteration, we first reconstruct the source intensity on a 32×32 grid with pixel sizes of $0.022''$. The source region is chosen so that it maps to a completely joined annulus on the image plane (so that we can determine the relative potential difference between images). The PSF is reduced to a 15×15 matrix to keep the inversion matrices sparse (and computation time low). As in the demonstration in the previous section, we use only the (unweighted) curvature type of regularization for the source reconstruction to reduce computation time. The source inversions are overregularized in the early iterations to ensure a smooth resulting source for taking gradients. Table 7.3 lists the overregularizing factors. With the resulting source intensity gradients and intensity deficits from source reconstruction, we perform the pixelate potential corrections on a potential grid of 30×30 pixels. We try both the curvature and jerk forms of regularization for each potential correction iteration, and pick the one with the higher evidence value. To keep the corrections linear, the potential corrections are also overregularized with the regularization constant (μ) set at 10 times the value where $\sim \mu E_{\delta\psi}$ peaks. The corrected potential has the midpoints in the left, bottom and right parts of the annular reconstruction region fixed to the initial potential model. Table 7.3 lists the preferred form of regularization in each iteration. Fermat potential differences between the images are also added to the image data set during the potential correction. These Fermat potential values are obtained from scaling the measured relative time delays by the factor $\frac{D_{\rm s}D_{\rm d}(1+z_d)}{cD_{\rm ds}}$ (see equation (2.7)) and using the predicted $H_0 = 76$ km s^{-1} Mpc^{-1} from the SPLE1+D (isotropic) model (Koopmans et al. 2003b). Table 7.4 lists the measured Fermat potential differences between the images.

Recall that lensing alone cannot determine the Hubble constant due to the mass-sheet degeneracy (details in section 2.1.2). Therefore, we attempt to recover a corrected potential on a grid of pixels (kept close to the initial model with the values at three points in the annular reconstruction region fixed to the initial SPLE1+D (isotropic) model) that at the same time fits the Fermat potential difference based on the input $H_0 = 76$ km s^{-1} Mpc^{-1}. At the last iteration of potential reconstruction, any misfit between the predicted and

Table 7.3: Regularization types and values for source intensity and potential reconstruction of B1608+656

Iteration	Reg. Type	Reg. Val	Overreg. factor
0/SrRec	curv	0.082	1000.
1/SrRec	curv	0.214	1000.
2/SrRec	curv	0.308	1000.
3/SrRec	curv	0.325	100.
4/SrRec	curv	0.331	100.
5/SrRec	curv	0.323	100.
6/SrRec	curv	0.321	10.
7/SrRec	curv	0.332	10.
8/SrRec	curv	0.348	1.
9/SrRec	curv	0.356	1.
10/SrRec	curv	0.389	1.
11/SrRec	curv	0.402	1.
12/SrRec	curv	0.408	1.
13/SrRec	curv	0.418	1.
14/SrRec	curv	0.401	1.
15/SrRec	curv	0.426	1.
0-15/PotRec	curv	1.9×10^8	10.

Note. — The first column denotes the iteration number for either the source intensity inversion or potential correction. The second to fourth column shows the type of regularization used, the regularization value (from maximizing the evidence for source reconstruction and from peak of $\mu E_{\delta\psi}$ for potential correction), and the overregularization factor. For potential reconstructions, curvature regularization is preferred to jerk regularization for all iterations and we use the same overregularization factors in all iterations. The regularization constants in the source intensity reconstructions on average increase with iterations, indicating that the prior is becoming more relevant as we correct the perturbed potential. With high amounts of potential perturbation in early iterations, the likelihood overwhelms the prior.

Table 7.4: Relative Fermat potentials for B1608+656

	measured Fermat potential	predicted Fermat pot
ϕ_{AB}	0.238 ± 0.011	0.244
ϕ_{CB}	0.272 ± 0.011	0.276
ϕ_{DB}	0.582 ± 0.011	0.576
χ^2_ϕ	–	0.67

Note. — The measured relative Fermat potential is derived from the measured relative time delays (Fassnacht et al. 2002), and the predicted relative Fermat potential is obtained from the reconstructed pixelated potential of B1608+656. The predicted relative Fermat potential agrees with the measured values within the errors. The range of H_0 values from the three relative Fermat potential provides an estimate of the error on the recovered input $H_0 = 76$ km s^{-1} Mpc^{-1}. This is discussed in detail in chapter 8.

measured Fermat potential difference gives an estimate of the error in the potential due to PSF, dust and lens galaxies' light models. This is the dominant source of error since the statistical error on $\boldsymbol{\delta\psi}$ is very small due to the extreme overregularization that is applied to keep corrections small (recall in section 4, overregularization drives the 1 σ error to zero). At the end of the day, the reconstructed potential can have arbitrary additions of symmetric paraboloids to obtain any value of H_0. This degeneracy in H_0 is broken only when we provide external information such as the velocity dispersion of the lens, which will limit the amount of mass sheet (symmetric paraboloids in the potential) that we can add.

Figure 7.14 shows the results of iteration=0 of source and potential reconstruction. The top left-hand panel shows the reconstructed source that has been overregularized by a factor of 1000. The caustics are those of the initial SPLE1+D (isotropic) model. The source is localized and compact, a sign that the initial SPLE1+D (isotropic) potential we started from is close to the true model. The intensity deficit on the top right-hand panel shows significant image residuals that are to be corrected, especially near the cores of the images. The annular region marks the region of data that we use for source reconstruction. The edges of the image residual have patches of high values due to the noisy dust map that has artificially high values (amplitudes) in regions where the signal-to-noise ratios in the images are low. Since these patches of the dust map lie mostly outside the annular region (the data used for source and potential reconstruction), we can safely disregard them. Using the gradient from the regularized source and the intensity deficit, the bottom left-hand panel

shows the iteration=0 potential reconstruction and the bottom right-hand plot shows the fraction of the accumulated potential corrections relative to the initial model.

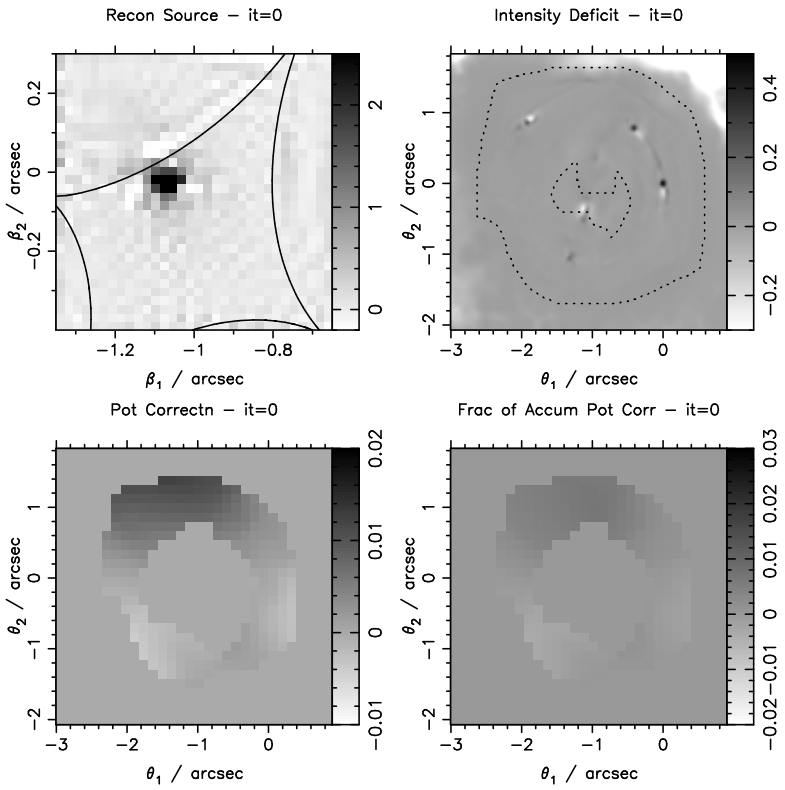

Figure 7.14: Results of iteration=0 of pixelated potential reconstruction of B1608+656. Top row: the left-hand panel shows the curvature regularized source reconstruction that is overregularized by the factor listed in table 7.3, and the right-hand panel shows the resulting intensity deficit based on the inverted source and the iteration=0 (initial) potential model. Bottom row: the left-hand panel shows the potential corrections on an annulus using curvature form of regularization and the regularization constant listed in table 7.3, and the right-hand panel shows the accumulated potential corrections relative to the initial potential model. The source is localized, an indication that we are close to the initial model, but not at the true potential model because significant intensity deficits are present.

Figure 7.15 shows the result of iteration=2 of source and potential reconstruction. With the same overregularization factor as in iteration=0, the source reconstruction now looks smoother as the potential has been corrected. The image residual has decreased compared to the iteration=0 case. The potential correction is not as large as we iteratively corrects.

Figure 7.16 shows the result of iteration=3 of source and potential reconstruction. The source is now overregularized by a factor of 100, which is a factor of 10 smaller than in

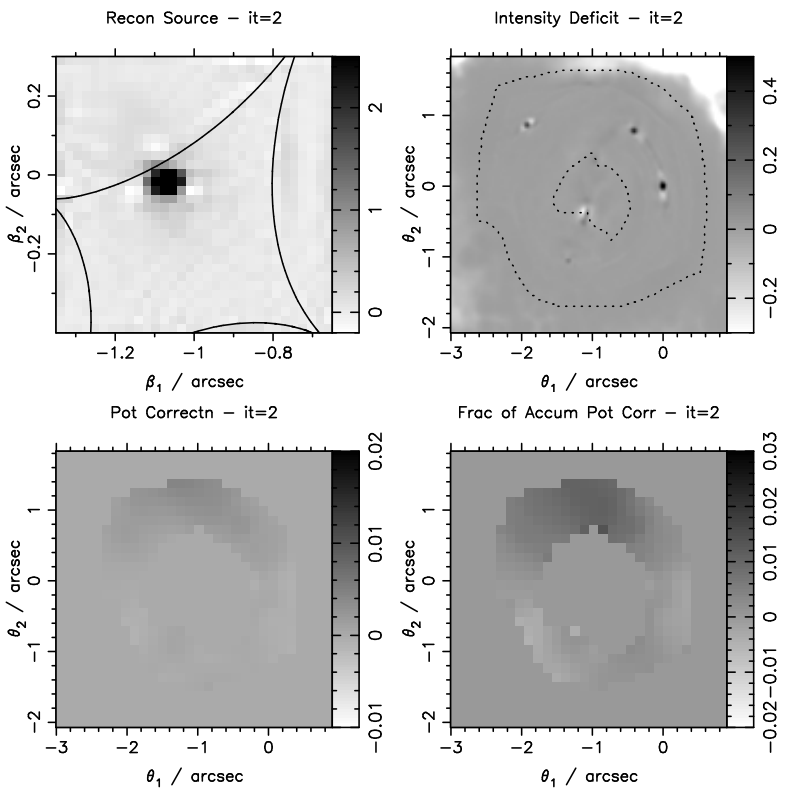

Figure 7.15: Results of iteration=2 of pixelated potential reconstruction of B1608+656. The panels are plotted in the same manner and on the same scales as in figure 7.14 for comparison. Compared to the source reconstruction in iteration=0, the source reconstruction with the same overregularization is now smoother with two iterations of potential corrections. The intensity deficit has also decreased compared to iteration=0.

iteration=2. Therefore, we see an increase in the background noise in the source reconstruction. However, the intensity deficit exhibits a significant drop in magnitude compared to iteration=2.

In the iterations from 3 to 15, the potential corrections are small and therefore the source reconstruction and image residual only change very gradually from one iteration to another. Figure 7.17 shows the results of iteration=15 (the last iteration) of source and potential reconstruction. The reconstructed source in the top left-hand panel has more background noise than iteration=3 because the source is optimally regularized instead of overregularized. Nonetheless, the source is still localized even without overregularization, which is a good indication that the reconstructed potential is close to the true potential

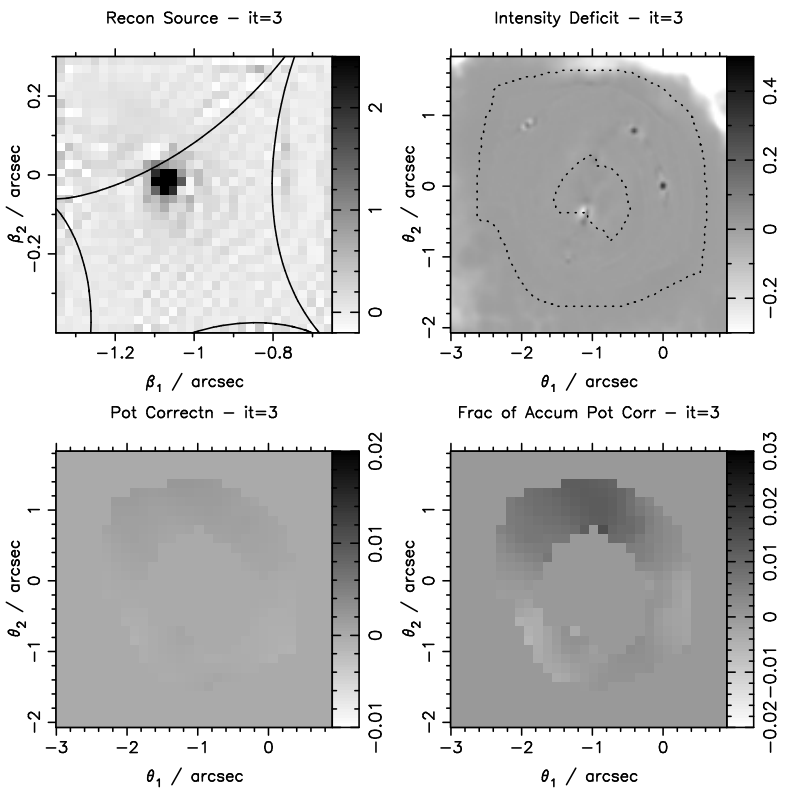

Figure 7.16: Results of iteration=3 of pixelated potential reconstruction of B1608+656. The panels are plotted in the same manner and on the same scales as in figure 7.14 for comparison. Compared to the source reconstruction in iteration=2, the source reconstruction with the same overregularization is now slightly noisier with less overregularization. The intensity deficit is decreased more from iteration=2 to 3 than from 0 to 2 with the smaller amount of overregularization.

(up to the mass-sheet degeneracy). The reconstruction is not at the true potential because the top right-hand panel shows remaining intensity deficit. Further iterations of potential corrections do not seem to correct away these image residuals. This may be due to inherent imperfect PSF, dust, and lens galaxies' light models. Since the PSF is time varying, and the intensities of the point sources do not generally match due to the time delays and variability, we do not expect the PSF, dust and lens galaxies' light models to describe the system perfectly. The remaining residual can also be due to the limited resolution on the source grid near the core of the source or the undersampling of the PSF. Nonetheless, despite these limitations in the modeling, we have significantly reduced the intensity deficit after 16 iterations as is seen in Figures 7.14 and 7.17. In quantitative terms, the reduced

χ^2, as given by $\chi^2/(N_{\text{pix in annulus}} - \gamma)$ (where $N_{\text{pix in annulus}}$ is the number of data pixels in a fixed annulus that encloses the ring and γ is an estimate of the number of "good" parameters; see earlier sections 3.2.1 and 4.2.3 and table 4.1), decreased by ∼75% from iteration=0 to iteration=15. Specifically $\chi^2/(N_{\text{pix in annulus}} - \gamma)$ decreased from 20.3 to 4.5. Since the intensity deficit scales with the potential correction in equation (7.11) and we expect the source to be roughly constant (as it looks localized already), we expect that the accumulated potential corrections even with the perfect PSF, dust, and lens galaxies' light will be $\lesssim$1.5× the amount obtained at iteration=15 in figure 7.17. With the accumulated potential correction in the bottom right-hand panel in figure 7.17 showing corrections of the order of ∼2%, we expect at most ∼3% correction of the initial SPLE1+D (isotropic) lens potential. The difference in the predicted and the measured relative Fermat potentials between images would only decrease (down to the noise level) with perfect modeling.

The potential correction in the bottom left-hand panel in figure 7.17 shows minimal correction at iteration=15, which is expected for late iterations. Table 7.4 lists the predicted relative Fermat potential. The resulting χ^2_ϕ is small, so we have faithfully recovered the initial $H_0 = 76$ km s^{-1} Mpc^{-1} within the errors of the time delays. In fact, we have recovered the initial H_0 within the range set by the best time delay error (from Δt_{DB}). We attribute this to the high quality ACS data that allow us to correct the potential with a precision that is set by the lowest error in all relative time delay measurements. A detailed error estimate on the recovered H_0 due to the PSF, dust, lens galaxies' light, and lens potential model is presented in the next chapter.

In summary, the pixelated potential correction scheme was successfully applied to B1608 +656 leading to potential corrections of ∼2%. The predicted time delays (from Fermat potentials) match the measured time delays within the uncertainties, reproducing the input Hubble constant of 76 km s^{-1} Mpc^{-1}. The resulting source is localized, and the image residual has been significantly reduced, leaving only small amounts of residual at the AGN image positions.

This completes the dissection of the gravitational lens B1608+656. The image residual is not fully eliminated possibly due to imperfect PSF, dust, lens galaxies' light modeling, variability in the point source intensities (which leads to the images having different intensities due to time delays), finite source resolution, and/or undersampled PSF. In the following chapter, we give an estimate of the error on H_0 associated with the modeling.

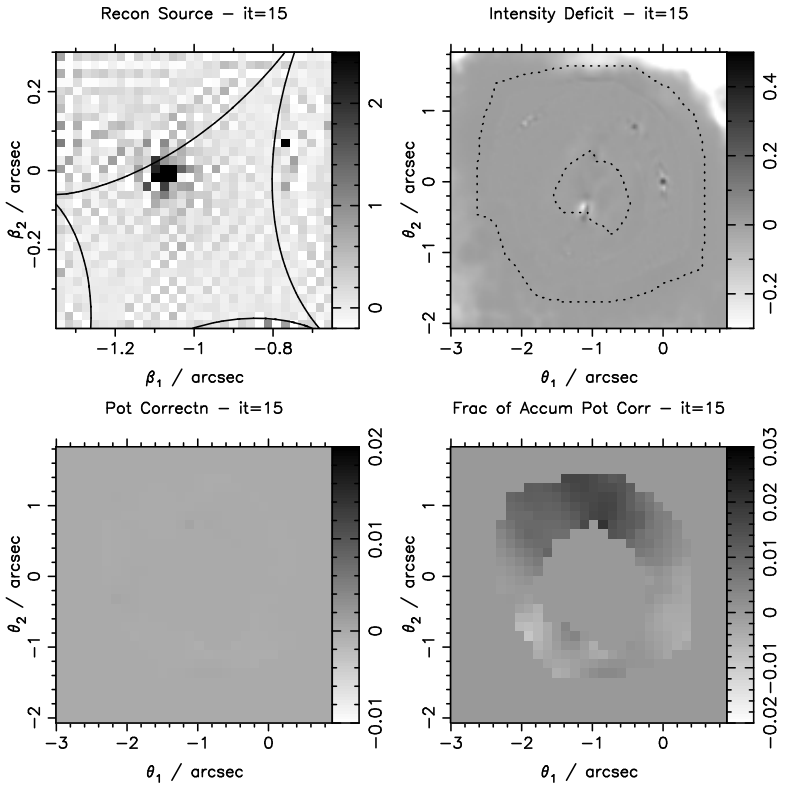

Figure 7.17: Results of iteration=15 of pixelated potential reconstruction of B1608+656. The panels are in the same pattern as in figure 7.14 and are plotted in the same scales for comparison. The reconstructed source is now optimally regularized. The intensity deficit has been reduced by a factor of ∼75% in χ^2 after 15 iterations of correction, which is visible in the top right-hand panel compared to that in figure 7.14. Residuals remain due to imperfect PSF, dust, lens galaxies' light modeling, and/or limited source grid resolution. The potential correction is barely visible after many iterations. The accumulated potential corrections are on the order of ∼2%.

Chapter 8

The Global Solution and Its Implication for the Hubble Constant

In the previous chapter, we successfully applied the pixelated potential reconstruction method to correct the lens potential of B1608+656. The resulting source intensity distribution was found to be localized, and the overall potential correction was ∼2%. However, there remained visible image residuals that could not be fully removed even though the magnitude of the residuals had decreased by ∼75% after potential corrections. These remaining residuals could be due to imperfect PSF, dust, lens galaxies' light modeling, limited source grid resolution or undersampled PSF. In section 8.1, we quantify the errors associated with these effects by considering a sample of PSFs, dust models, and lens galaxies' light models. The objective is to set a rational statistical uncertainty on H_0 associated with lens modeling. Even with perfect lens modeling, mass-sheet degeneracy (introduced in section 2.1.2) that is inherent to gravitational lensing prevents us from determining a unique value of the Hubble constant. In section 8.2, we describe ways to break the mass-sheet degeneracy and place limits on the presence of any mass sheets in B1608+656. Based on the results, we discuss the uncertainties on the Hubble constant from B1608+656.

8.1 Error Analysis

In the pixelated potential reconstruction of B1608+656 (section 7.3.4), we use the three relative Fermat potentials as part of our data to constrain the potential corrections in each

iteration. The values of the relative Fermat potential were derived using the measured relative time delays (Fassnacht et al. 2002) and the H_0 value of 76 km s^{-1} Mpc^{-1} from the initial SPLE1+D (isotropic) lens potential model (Koopmans et al. 2003b). After the iterative potential reconstruction, deviations of three resulting H_0 values from the input value of 76 indicate the amount of error in the lens potential associated with the PSF, dust, and lens galaxies' light modelings. The statistical error in the potential due to the noise in the data is small due to the overregularization (which suppresses the noise) and is thus negligible compared to the error associated with imperfect PSF, dust and lens galaxies' light models.

We now give an overview on our approach for estimating the error on H_0 due to modeling. The key point is that we cannot estimate the error on the potential correction (which relates to the error on H_0) from the method outlined in section 7.3.2 because of the iterative and overregularized nature of the method. One possible procedure to estimate the error on the potential correction would be to (i) generate via Monte Carlo simulations mock data sets that share the same noise properties as the data image, (ii) obtain the potential correction using the iterative scheme in the previous chapter for each mock data set, and (iii) determine the error on the reconstructed potential based on the range obtained from the mock data sets in step (ii). However, this is beyond the scope of this thesis and we defer it to future work. In this work, in order to get approximate yet robust estimates of the error on H_0, we simply investigate how the resulting predicted H_0 values depend on the PSF, dust and lens galaxies' light models by considering a representative sample of models. We expect that poor PSF, dust and lens galaxies' light models will not allow us to recover the input H_0 value (76 km s^{-1} Mpc^{-1}), whereas good models will allow us to recover the input H_0 value. We therefore need a method for ranking the models, and as in previous chapters, we use the Bayesian evidence from source reconstruction as our objective and quantitative measure of the goodness of models. Assuming all models are equally probable a priori, the evidence value of a model indicates the relative probability of the model given the data (as discussed in section 3.2.2). Therefore, good models will have higher evidence values than poor models. Recall the Bayesian evidence incorporates Occam's Razor and thus penalizes overly complex models: one can think of evidence maximization as being equivalent to minimizing the image residuals (i.e., finding a good model that fits to the data) without fitting to the noise in the data (i.e., keeping the model simple). Since the source reconstruction

uses only the observed image data and not the time delay data, the Bayesian evidence from source reconstruction gives us an unbiased measure of the goodness of the models that is independent of the resulting H_0 values from the models. We therefore use the Bayesian evidence from source reconstruction to weight the error in H_0 associated with each model (as given by the standard deviation from input H_0) so as to get an approximate uncertainty on H_0 due to modeling. In the following paragraphs, we explain in detail the sample of models we use, the pixelated potential reconstruction and the final source intensity reconstruction for model comparison.

For a representative sample of PSF, dust and lens galaxies' light, we use the ones listed in table 6.4. These models contain various dust maps and lens galaxies' light profiles based on the four PSF models: drizzled PSF, closest star in the field, brightest star in the field, and second brightest star in the field. Recall the dust map can be obtained from 2 bands (ACS only) or from 3 bands (ACS and NICMOS) for each PSF model. The lens galaxies' light were obtained by fitting Sersic profiles with integral indices to dust corrected F814W images. Table 6.4 contains the PSF and dust map information. We exclude Model 1 because we have shown in chapter 6 that it is similar to Model 2 due to the lens model having weaker dependence on the lens galaxies light than on the PSF and dust models. Model 5 is the one we selected as our optimal model for potential reconstruction in the previous chapter. For the remaining models in table 6.4 (Models 2–4 and 6–10) , we perform 16 iterations of source intensity and potential corrections using the SPLE1+D (isotropic) as the initial potential model. The source inversions are overregularized by the same factors as those listed in right-most column in table 7.3. The amount of overregularization for the potential reconstruction differs slightly between the models in table 6.4, but the resulting (overregularized) regularization constants are all within a factor of 10 from the empirically determined values given by the peak of $\mu E_{\delta\psi}$. The overregularization constants are adjusted slightly to ensure corrections are smooth (as lens potentials ought to be). The relative Fermat potentials, which are based on the measured time delays and the input $H_0 = 76$ km s^{-1} Mpc^{-1} from SPLE1+D (isotropic) model, are also included in the data. Table 8.1 summarizes the results of the predicted relative Fermat potentials from the corrected lens potentials. Using the measured relative Fermat potential listed in table 7.4, we also compute the χ^2_ϕ of the Fermat potential.

To rank the models listed in table 8.1, we first mark an annular region on the image

plane that roughly corresponds to rectangular regions on the source planes for the various corrected lens potentials, and use this same annular region (same data set) for reconstructing the source intensity for each of the corrected lens potentials. We fix the source region to have 32×32 pixels, which leads to pixel sizes that are on average 0.03". The PSFs are reduced to a 15×15 grid for the source inversion. We weighted the regularizations, but find the resulting source intensities and image residuals appear to be nearly identical to that of the unweighted regularized inversion (the $E_{\rm D}$ values are the same within $\sim$0.5%). However, the log evidence values for the weighted are are generally $\sim10^3$ higher than the unweighted one, due to the scaled regularization matrix $\mathbf{C}$ being larger in magnitude (with many source intensity pixels having absolute values less than 1), which gives higher $\det\mathbf{C}$ and thus higher log evidence in equation (3.19). Therefore, we quote the results of the weighted regularized inversions for the source intensities. Table 8.1 lists the resulting Bayesian evidence values from the source inversion for the various corrected lens potential. Having kept the data region the same, we can compare the different models (PSF, dust, lens galaxies light, resulting corrected lens potential) using the Bayesian evidence. We emphasize that these evidence values are based solely on the source reconstruction using the observed ACS F814W data and do not include the χ^2_ϕ from the Fermat potentials (time delays).

Assuming all models in table 6.4 to be equally probable a prior, we can use the value of the evidence directly to compare the models (recall sections 3.2.2 and 6.1). These are given in table 8.1. We see that Model 5 is preferred to all other models by a significant margin. For example, Model 5 is a factor of e^{1800} more probable than Model 3 (the second-best model) based on the ACS data. As mentioned in the previous chapter, Model 5 leads to a χ^2_ϕ from the relative Fermat potentials that deviates from the measured values in amounts smaller than that allowed by the uncertainty in the time delay measurements. This is due to the superb quality of the ACS data that enables us to recover the lens potential to a high precision. The top two models (5 and 3) both lead to small χ^2_ϕ values. On the other hand, Models 4, 6, and 8 have high χ^2_ϕ values. In other words, during the iterative pixelated potential correction, the potential has strayed while trying to minimize the image residual, and thus leads to a large deviation between the predicted relative Fermat potentials and the measured values. Based on the log evidence values from source inversion, high χ^2_ϕ values only occur when the model is bad. The three models (4, 6, and 8) with the highest χ^2_ϕ values are also the ones with the lowest log evidence values. In getting an error on the

recovered H_0 value from this sample, these poor models should be down weighted.

Table 8.2 lists in columns 2–4 the resulting three predicted H_0 values from the three Fermat potential differences in table 8.1 for each of the models. In column 5, the standard deviation of the three H_0 value from the input value of 76 km s^{-1} Mpc^{-1} is computed and listed. A perfect set of models (PSF, dust, lens galaxies' light) with no noise in the data would give us a standard deviation of zero. Therefore, these standard deviation values provide an estimate for the uncertainty associated with PSF, dust, lens galaxies light modeling, and noise in the data. Since the Bayesian evidence values rank the models, we weight the standard deviations in column 5 by the normalized evidence values to obtain the error estimate on H_0. With the huge disparity in the log evidence values between the models (on the order of $10^3 - 10^4$), the error on H_0 is essentially given by that of Model 5, which is ± 1.3 km s^{-1} Mpc^{-1}. This small amount of error may seem striking, but we point out that even the next best model (3) gives an error of $\sim$1 km s^{-1} Mpc^{-1} even though it is e^{1800} less probable than Model 5. In some sense, it is reassuring that the best models for the ACS data also reproduce the input $H_0 = 76$ km s^{-1} Mpc^{-1} remarkably well. The error on H_0 from these two models are consistent with the errors in the time delay measurements listed in table 5.1. Effectively, the error on H_0 is determined by the image pair with the smallest uncertainty in the relative time delays (images D and B) because the extended nature of the source allows the potential offset (hence time delays) between the images to be recovered during the pixelated potential reconstruction procedure even with solely the data from the observed image.

Notice that recovering the input H_0 is not always possible; some of the bad models (with low evidence values) such as 8 cannot reproduce the input H_0 as the iterative potential correction proceeds to reduce the intensity deficit. This analysis does not preclude the existence of a better PSF, dust and lens galaxies' light model that fits to the ACS data with a higher Bayesian evidence. However, given the standard deviations of the two best Models (5 and 3) that we have, we might expect the standard deviation in the recovered H_0 from the input value of 76 km s^{-1} Mpc^{-1} to be no more than $\sim$1.5 km s^{-1} Mpc^{-1} (limited by error on time delay measurement) for this hypothetical better model. Therefore, we adopt a conservative modeling error (due to noise in the observations and modeling of PSF, dust, lens galaxies' light, and lens potential) on the input H_0 to be 2 km s^{-1} Mpc^{-1}. With even better lensing observations, the modeling error could be reduced; therefore, we refer to the

Table 8.1: The predicted Fermat potential difference and the log evidence of the source reconstruction using the corrected lens potential (with 16 iterations) based on the various PSF, dust and lens galaxy light models listed in table 6.4

Model No.	PSF	dust map	ϕ_{AB}	ϕ_{CB}	ϕ_{DB}	χ^2_ϕ	log evidence
2	drz	drz/3-band	0.2485	0.2837	0.5704	2.93	-1.35×10^3
3	C	C/3-band	0.2392	0.2741	0.5749	0.42	1.46×10^4
4	C	C/2-band	0.2067	0.2412	0.5469	24.69	-9.69×10^3
5	B1	B1/3-band	0.2435	0.2762	0.5757	0.67	1.64×10^4
6	B1	B1/2-band	0.2061	0.2382	0.5488	25.43	-5.86×10^3
7	B2	B2/3-band	0.2252	0.2585	0.5726	3.40	-4.26×10^3
8	B2	B2/2-band	0.1925	0.2249	0.5511	40.91	-1.67×10^4
9	C	B1/3-band	0.2281	0.2611	0.5628	4.57	3.89×10^3
10	B1	C/2-band	0.2403	0.2682	0.5681	1.65	-1.79×10^3

Note. — For the reader's convenience, we list the PSF and dust model corresponding to each model. In the PSF column, "drz"≡drizzled Tiny Tim, "C"≡closest star, "B1"≡bright star #1, and "B2"≡bright star #2. In the dust map column, "2-band" represents the dust map obtained from just the two ACS bands, and "3-band" represents the dust map obtained from the two ACS and the one NICMOS band. The lens galaxies' light are Sersic profiles with integral indices between 1 and 4 that fit the dust-corrected image (not listed here; see table 6.4). In all cases, weighted zeroth-order regularization is preferred (based on the log evidence value) to unweighted zeroth order, weighted and unweighted gradient, and weighted and unweighted curvature regularization. The corresponding evidence value is listed, which we can use to compare different models since the data region is the same for all inversions. Model 5 is the best model; based on the log evidence values, Model 5 provides a PSF, dust, lens galaxy light, and corrected lens potential that is $\sim e^{1800}$ times more probably than Model 3, the second best model. The χ^2_ϕ values are obtained using the measured relative Fermat potential listed in table 7.4. The models with low evidence values (based purely on source inversion and does not include the misfit in the time delay) are also the ones with large values of χ^2_ϕ.

Table 8.2: The range of H_0 values for various PSF, dust and lens galaxies' light models

Model No.	H_0^{AB}	H_0^{CB}	H_0^{DB}	σ_{H_0}	log evidence
2	79.4	79.3	74.5	2.8	-1.35×10^3
3	76.4	76.6	75.1	0.7	1.46×10^4
4	66.0	67.4	71.4	8.1	-9.69×10^3
5	77.8	77.2	75.2	1.3	1.64×10^4
6	65.8	66.6	71.7	8.4	-5.86×10^3
7	71.9	72.2	74.8	3.3	-4.26×10^3
8	61.5	62.8	72.0	11.6	-1.67×10^4
9	72.8	73.0	73.5	2.9	3.89×10^3
10	76.7	74.9	74.2	1.3	-1.79×10^3

Note. — Columns 2 to 4 are the recovered values of H_0 (in units of km s^{-1} Mpc^{-1}) of the Models in table 6.4 for all three image pairs based on the predicted relative Fermat potential listed in table 8.1. For each model, the standard deviation of the recovered H_0 values from the input $H_0 = 76$ km s^{-1} Mpc^{-1} is computed and listed in column 5. The Bayesian log evidence from the source inversions are repeated from table 6.4. These log evidence values are based only the image data and are independent of the time delay measurements. Weighting the standard deviation by the evidence values (recall that the evidence value indicates how probable the model is given the data, assuming flat priors on the models), the error associated with imperfect PSF, dust, lens galaxy light, and corrected lens potential is dominated by Model 5, which gives 1.3 km s^{-1} Mpc^{-1}

modeling error as the statistical error.

The analysis in this section quantifies the statistical error associated with the PSF, dust, lens galaxies' light and lens potential modeling. It does not include the error due to the mass-sheet degeneracy (discussed in section 2.1.2), which could raise or lower the value of H_0 without changing the lensing observables. We refer to this type of error that can only be reduced by making additional assumptions or nonlensing observations as systematic. In the following section, we estimate the amount of systematic error associated with the mass-sheet degeneracy.

8.2 Hubble Constant from B1608+656

In order to break the mass-sheet degeneracy in B1608+656 and restrict the range of permissible H_0, we need to get an estimate of the total external convergence, κ_c, at the lens system. There are two approaches: (i) using stellar dynamics of the lens and (ii) modeling

the galaxy groups associated with the lens. We describe each of these in turn.

8.2.1 Constraints from the Stellar Velocity Dispersion of B1608+656

Stellar dynamics can be used jointly with lensing to break the mass-sheet degeneracy by providing an estimate of the enclosed mass at a radius smaller than the radius of the Einstein ring (e.g., Grogin & Narayan 1996a,b; Tonry & Franx 1999; Koopmans & Treu 2002; Treu & Koopmans 2002; Barnabè & Koopmans 2007). Any mass sheet associated with the lens halo (e.g., the galaxy group at the lens redshift) is taken into account by the dynamical model. Since the initial SPLE1+D (isotropic) parametric model (Koopmans et al. 2003b) includes dynamical information, it has already included any internal mass sheet. In this section, we describe how the measured velocity dispersion of 247 ± 35 km s^{-1} of the primary lens galaxy G1 in B1608+656 can limit the amount of *external* mass sheet (due to groups along the line of sight, large scale structure, etc.). We mention that the presence of G2 complicates stellar dynamics; however, since G1 seems very weakly disturbed, we expect the effect of G2 on G1's velocity dispersion to be small. The key questions are how much external mass sheet we could add before the measured velocity dispersion constraint is violated and how the added mass sheet affects H_0. An external mass sheet would lower the mass of the lens (see equation (2.11)) and thus lower the velocity dispersion. In other words, a lens model that is based solely on lensing data and that does not take into account the mass sheet would predict too high a value for the velocity dispersion due to the extra mass from the mass sheet. The uncertainty on the measured velocity dispersion thus limits the amount of mass sheet we could add. If there is an unknown mass sheet, then a joint lensing and dynamics modeling would tend to lower the radial slope of the lens profile to lower the predicted velocity dispersion to better match the measured velocity dispersion. This would lower the measured value of H_0, and thus counteract the raising of the measured value of H_0 due to the unknown mass sheet. Therefore, by including information from the velocity dispersion, the effect of the external mass sheet on H_0 is reduced.

We can quantify the effect of the external mass sheet on H_0 by considering a few scaling relations. Let σ be the stellar velocity dispersion, γ be the slope in the density profile of G1, M be the mass of the lens, and κ_c be the convergence of the external mass sheet. Using

these notations, we have:

1. $\frac{\mathrm{d}\sigma}{\sigma} \sim 1.5\frac{\mathrm{d}\gamma}{\gamma}$. This is an empirical relation that is obtained by running dynamical models of B1608+656. It relates the fractional change in the velocity dispersion to a fractional change in the density slope of G1.

2. $\frac{\mathrm{dM}}{M} = 2\frac{\mathrm{d}\sigma}{\sigma}$. This is from the fact that the best mass model of B1608+656 is effectively isothermal (excluding any mass sheet) even without stellar dynamics constraints (see table 4 in (Koopmans et al. 2003b), so $M \propto \sigma^2$ from the Virial Theorem.

3. $\kappa_c = -\frac{\mathrm{dM}}{M}$. This is derived from equation (2.11), where adding κ_c $(= 1 - \lambda)$ scales the mass distribution down by $(1 - \kappa_c)$.

4. $\frac{\mathrm{d}\gamma}{\gamma} = 0.5\frac{\mathrm{dH_0}}{H_0}$. This is based on (Wucknitz 2002), but rewritten in our notation.

Combining these relations, we obtain that $\frac{\mathrm{dH_0}}{H_0} \sim -\frac{2}{3}\kappa_c$. In other words, by adding an unknown external mass sheet κ_c, the value of H_0 is lowered using constraints from stellar dynamics. However, *not* having taken the external mass sheet into account raises H_0 by $\frac{\mathrm{dH_0}}{H_0} = +\kappa_c$ (as explained in section 2.1.2). Adding these two effects, we have $\frac{\mathrm{dH_0}}{H_0} \sim \frac{1}{3}\kappa_c$. Therefore, having dynamical information reduces the effect of an unknown mass sheet on H_0 by a factor of 3.

Given the measured velocity dispersion of 247 ± 35 km s^{-1}, we have $\frac{\mathrm{d}\sigma}{\sigma} \sim 0.14$ which implies that the external mass sheet could be at most 0.28. With $\kappa_c < 0.28$, then $\frac{\mathrm{dH_0}}{H_0} < \frac{1}{3} = 0.09$ which corresponds to a maximal uncertainty on H_0 of $\sim$ 7km s^{-1} Mpc^{-1}. This limit holds for any mass sheet, either due to the galaxy groups, galaxy clusters, or the large scale structure along the line of sight. Based on the low group velocity dispersion of B1608+656 (Fassnacht et al. 2006), small external shear, agreement of dynamical and lensing slopes, the actual external mass sheet should be $\ll 0.28$. Furthermore, the fact that lensing constraints alone gives a density slope of 2.0 that almost perfectly predicts the observed velocity dispersion (within the errors) (Koopmans et al. 2003b) suggests the effects of mass-sheet degeneracy to be relatively minimal. Nonetheless, ± 7 km s^{-1} Mpc^{-1} is our conservative estimate of the error associated with unknown mass sheet based on the measured velocity dispersion. Note that the quoted error is symmetric about $H_0 =$ 76 km s^{-1} Mpc^{-1} from modeling due to the error in the velocity dispersion being symmetric.

However, based on group studies of B1608+656 (Fassnacht et al. 2006), we expect that value of H_0 from modeling to be biased high. This is discussed in the next section.

8.2.2 Group Effects on B1608+656

As mentioned in chapter 5, Fassnacht et al. (2006) conducted a spectroscopic survey, discovering that B1608+656 lies in a group, and that there are three additional groups along the line of sight. Each of these groups contain ∼10 members. The group at the lens redshift seems to have a low mass with a velocity dispersion of 150 ± 60 km s^{-1}. Following Keeton & Zabludoff (2004), Fassnacht et al. (2006) used two approaches to estimate the external convergences due to groups. The first approach assumes that the group can be modeled as a single smooth mass distribution, and the second approach assumes that the masses are associated with individual galaxy group members with no common halo. The realistic mass distribution for galaxies group should be somewhere between these two extremes, so the two approaches should provide a reasonable range for the external convergences. Depending on the method used, Fassnacht et al. (2006) estimated that each of the groups provides an external convergence of $\kappa_c \sim 0.005 - 0.060$ (which are listed in Table 2 in their paper). Based on the estimated values of κ_c from the three groups along the line of sight and the fact that the B1608+656 appears to be an overdense line of sight (C. D. Fassnacht et. al., 2007, in preparation), the external convergence along the line of sight is $\kappa_c = 0.05 \pm 0.05$. The error on κ_c is the systematic error due to the mass-sheet degeneracy. Using equation (2.15), we get the external convergence corrected H_0 to be $H_0 = 72 \pm 2$ (stat.) ± 4 (syst.). The value obtained is consistent with the constraints from the measured stellar velocity dispersion.

Based on the analysis discussed above, it is evident the statistical (modeling) error is significantly less than the systematic error due to mass-sheet degeneracy (environment). This is good news in the sense that the systematic error could be beaten down by understanding the mass structures along the line of sight or getting a better stellar velocity dispersion measurement. The latter is certainly possible in the near future; in fact, there are already plans for obtaining a more accurate measurement of the stellar velocity dispersion of G1. Optimistically, we could obtain a velocity dispersion measurement as accurate as 8 per cent, which translates to ± 4 km s^{-1} Mpc^{-1} on H_0. In conclusion, emphasis should

now be directed to a thorough study of the matter distribution along the line of sight to B1608+656 to get a more accurate measurement of H_0 to a few percent level from this system. The small statistical error bar (± 2 km s^{-1} Mpc^{-1}) that we are able to achieve with the high quality ACS data shows that gravitational lensing is indeed a competitive approach for measuring H_0 to high precision.

Chapter 9

Beyond B1608+656

In this thesis, we have developed special gravitational lens modeling techniques based on Bayesian analysis for treating the complex B1608+656 lens system. These methods are general, and can be applied to other lens systems. In this chapter, we describe two aspects of lensing that can be tackled using the tools developed in this thesis. We begin by giving a brief discussion of future time delay lenses. We then describe the concept of using gravitational lenses as cosmic telescopes, with an emphasis on a specific gravitational lens, the Cosmic Eye.

9.1 Future Time Delay Lenses

In this thesis, we have shown that an accurate measurement of H_0 is achievable using gravitational lenses with extended sources that have accurately measured time delays and good quality imaging. The dominant source of error lies in our incomplete knowledge of the structure of mass along the line of sight to B1608+656. One way to reduce this systematic error is to average over many lens systems along different lines of sight, thus obtaining H_0 statistically. This is the approach taken by, for example, Oguri (2007), who investigated the dependence of H_0 on the image configuration that is characterized solely by the asymmetry and opening angle of the image pair. Using 16 published time delays, Oguri (2007) obtained $H_0 = 68 \pm 6$ (stat.) ± 8 (syst.) km s^{-1} Mpc^{-1}. We argue that a detailed analysis of multiple lens systems in a similar fashion as this thesis allows one to reduce significantly the errors. However, the sample of well-measured time delay gravitational lenses is small. In fact, there are only $\sim$20 lens systems with time delay measurements, and of these, B1608+656 remains

as the only lens system where the three independent time delays have been measured with accuracies of a few percent. Furthermore, only a few of the lens systems have extended sources (most are quasars), which are, as we have shown, important for providing additional constraints on the lens potential. Nonetheless, this is changing thanks to ongoing projects like GLENDEMA,[1] COSMOGRAIL,[2] and other independent efforts to measure the time delays in gravitational lenses. Future ground-based surveys such as the Large Synoptic Survey Telescope (LSST) and Panoramic Survey Telescope and Rapid Response System (Pan-STARRS) and space-based surveys like the Supernova/Acceleration Probe (SNAP) will also drastically increase the number of time delay gravitational lenses. For example, LSST, which will scan across all observable sky with a cadence of ∼7–10 days for 10 years, will find ∼20,000 gravitational lens systems. We expect a few percent of these to have measurable time varying components. With the long baseline of 10 years, the time delays from LSST will be of comparable quality to that of B1608+656, i.e., accuracies of a few percent, though we mention that microlensing can be problematic in the optical wavelength (e.g., Morgan et al. 2006; Dobler et al. 2007). The imaging quality from LSST will be seeing limited and therefore follow-ups (from, for examples, *HST*/*JWST* (James Webb Space Telescope) or ground-based telescopes with adaptive optics) will be needed to obtain high resolution images for lens modeling. On the other hand, SNAP, with its cadence of ∼3 days on a smaller patch of sky for 3 years, will be able to deliver slightly better time delay measurements than LSST with immediate space-based image quality. Both LSST and SNAP expect to detect a few hundred lensed supernovae (P. Marshall, private communications). Due to the drastic variation in brightness of the lensed galaxy containing the supernova, both SNAP and LSST will be able to measure the time delay between the multiple images to accuracies of a few percent. Two nice things about lensed supernova instead of lensed time-varying AGNs are (1) after the supernova stage, the lensed extended source can be modeled more easily without the point source, and (2) type Ia supernovae are standard candles, which provides a measure of the *absolute* brightness, thus breaking the mass-sheet degeneracy. With hundreds of lensed quasars and supernovae from these surveys, the future of using time delay lenses for cosmography is bright.

[1] Gravitational LENses and DArk MAtter project

[2] the COSmological MOnitoring of GRAvItational Lenses

9.2 Cosmic Eye

With their magnifying nature, gravitational lenses can be used as natural "cosmic" telescopes to study distant objects. One example is the highly magnified (×30) Lyman break galaxy (LBG) LBG J213512.73010143 (Smail et al. 2007), also known as the Cosmic Eye, at $z \sim 3.07$. It was discovered serendipitously in the Snapshot program GO#10491 (PI: H. Ebeling) that targeted the cluster MACS J2135.2-0102 lying approximately $75''$ southward of the LBG. Figure 9.1 shows an image of the object, which looks like an eye due to the high magnitude of shear as a result of the nearby cluster, and hence the nickname Cosmic Eye. The study of the physical properties of LBG is important for understanding cosmic reionization since the dominant ionizing background at $z \gtrsim 3$ is thought to be the Lyman continuum radiation from star-forming galaxies (Bolton et al. 2005, 2006). The key parameter for determining the ionizing emissivity of galaxies is the escape fraction of Lyman-continuum photons, $f_{\rm esc}$. The high magnification allows one to resolve the galaxy at sub-kpc scales (that is not otherwise possible with current observational technologies). By relating the local $f_{\rm esc}$ to physical parameters derived from stellar population modeling (such as star-formation rate, age, and reddening), one can obtain new insights into the production of these ionizing photons. In order to study the LBG's physical properties, one needs an accurate source intensity reconstruction. Recently Dye et al. (2007) have modeled the lens using a baryonic Sersic component nested within a dark matter halo. However, significant image residuals remain, which the authors suggest could possibly be reduced with small modifications to the parametrization of the lens model. Based on the appearance of the highly extended lensed image (with visible connecting isophotes between the images), the Cosmic Eye is an ideal lens system for applying the pixelated potential reconstruction method. This is the next lens system that we will tackle. The pixelated potential reconstruction method is effectively the "adaptive optics" for cosmic telescopes.

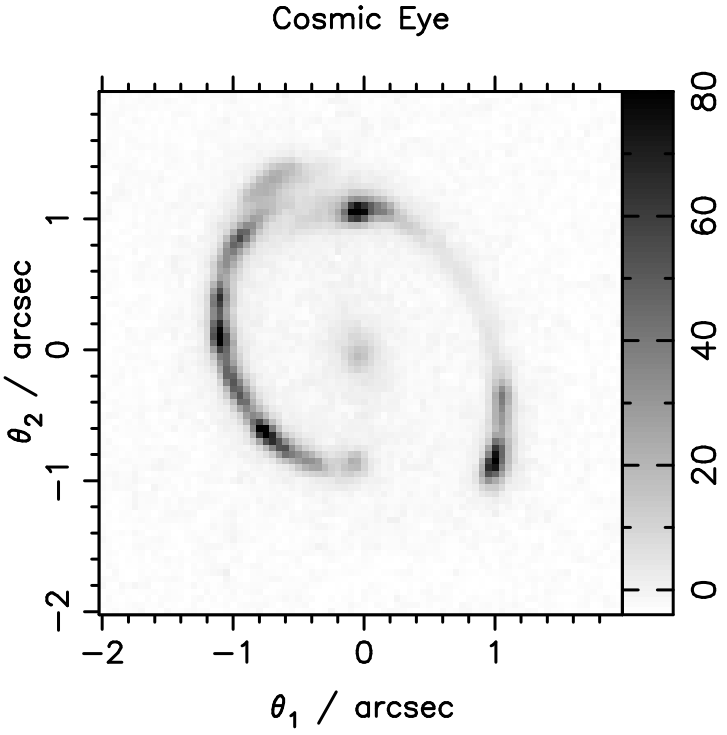

Figure 9.1: *HST* snapshot image of Cosmic Eye (LBG J213512.73010143). North is at an angle of 107.4° measured counterclockwise from the positive θ_2 axis.

We have illustrated how the work of this thesis is useful for other studies in lensing. In fact, the methods we developed are applicable to other fields since linear inversion problems appear ubiquitously in astrophysics. One example is reverberation mapping in active galactic nuclei (AGNs) (e.g., Blandford & McKee 1982; Peterson 2006) for determining the mass of the supermassive black holes at the center of AGNs. We encourage the readers to apply these methods to their favorite linear inversion problem!

Appendix A

Forms of Regularization

In this appendix, we discuss the forms of regularization that are used in chapter 4 for the source intensity reconstruction. The generalization of these forms of regularization for the potential corrections is discussed in chapter 7.

We consider the three most common quadratic functional forms of the regularization found in the local literature: "zeroth-order," "gradient," and "curvature" (Press et al. 1992, §18.4 and §18.5). Recall that quadratic forms are required for the inversion problems encountered in this thesis to be linear. For clarity reasons, we use explicit index and summation notation instead of vector and matrix notation for the expression of the regularizing function $E_{\rm S}(\boldsymbol{s})$.

Zeroth-order regularization is the simplest case. The functional form is

$$E_{\rm S}(\boldsymbol{s}) = \frac{1}{2}\sum_{i=1}^{N_{\rm s}} s_i^2, \tag{A.1}$$

and its Hessian is the identity operator $\mathsf{C} = \mathsf{I}$. This form of regularization tries to minimize the intensity at every source pixel as a way to smooth the source intensity distribution. It introduces no correlation between the reconstruction pixel values.

To discuss gradient and curvature forms of regularization, we label the pixels by their x and y locations (i.e., have two labels (i_1, i_2) for each pixel location instead of only one label (i) as in section 4.1) since the mathematical structure and nomenclature of the two forms of regularization are clearer with the two-dimensional labeling. Let s_{i_1,i_2} be the source intensity at pixel (i_1, i_2), where i_1 and i_2 range from $i_1 = 1, \ldots, N_{1\rm s}$ and $i_2 = 1, \ldots, N_{2\rm s}$. The total number of source pixels is thus $N_{\rm s} = N_{1\rm s}N_{2\rm s}$. It is not difficult to translate the

labeling of pixels on a rectangular grid from two dimensions to one dimension for vector analysis. For example, one way is to let $i = i_1 + (i_2 - 1)N_{2\mathrm{s}}$.

A form of gradient regularization is

$$\begin{aligned} E_{\mathrm{S}}(\boldsymbol{s}) &= \frac{1}{2}\sum_{i_1=1}^{N_{1\mathrm{s}}-1}\sum_{i_2=1}^{N_{2\mathrm{s}}}\left[s_{i_1,i_2} - s_{i_1+1,i_2}\right]^2 \\ &\quad + \frac{1}{2}\sum_{i_1=1}^{N_{1\mathrm{s}}}\sum_{i_2=1}^{N_{2\mathrm{s}}-1}\left[s_{i_1,i_2} - s_{i_1,i_2+1}\right]^2 \\ &\quad + \frac{1}{2}\sum_{i_1=1}^{N_{1\mathrm{s}}} s_{i_1,N_{2\mathrm{s}}}^2 + \frac{1}{2}\sum_{i_2=1}^{N_{2\mathrm{s}}} s_{N_{1\mathrm{s}},i_2}^2. \end{aligned} \tag{A.2}$$

The first two terms are proportional to the gradient values of the pixels, so this form of regularization tries to minimize the difference in the intensity between adjacent pixels. The last two terms can be viewed as gradient terms if we assume that the source intensities outside the grid are zeros. Although the nonsingularity of the Hessian of E_{S} is not required for equation (3.13) since equation (A.2) is of the form $E_{\mathrm{S}}(\boldsymbol{s}) = \frac{1}{2}\boldsymbol{s}^{\mathrm{T}}\mathbf{C}\boldsymbol{s}$, these last two terms ensure that the Hessian of E_{S} is nonsingular and lead to $\boldsymbol{s}_{\mathrm{reg}} = \mathbf{0}$. The nonsingularity of the Hessian of E_{S} (i.e., $\det\mathbf{C} \neq 0$) is crucial to the model comparison process described in section 3.2.2 that requires the evaluation of the log evidence in equation (3.19).

A form of curvature regularization is

$$\begin{aligned} E_{\mathrm{S}}(\boldsymbol{s}) &= \frac{1}{2}\sum_{i_1=1}^{N_{1\mathrm{s}}-2}\sum_{i_2=1}^{N_{2\mathrm{s}}}\left[s_{i_1,i_2} - 2s_{i_1+1,i_2} + s_{i_1+2,i_2}\right]^2 \\ &\quad + \frac{1}{2}\sum_{i_1=1}^{N_{1\mathrm{s}}}\sum_{i_2=1}^{N_{2\mathrm{s}}-2}\left[s_{i_1,i_2} - 2s_{i_1,i_2+1} + s_{i_1,i_2+2}\right]^2 \\ &\quad + \frac{1}{2}\sum_{i_1=1}^{N_{1\mathrm{s}}}\left[s_{i_1,N_{2\mathrm{s}}-1} - s_{i_1,N_{2\mathrm{s}}}\right]^2 \\ &\quad + \frac{1}{2}\sum_{i_2=1}^{N_{2\mathrm{s}}}\left[s_{N_{1\mathrm{s}}-1,i_2} - s_{N_{1\mathrm{s}},i_2}\right]^2 \\ &\quad + \frac{1}{2}\sum_{i_1=1}^{N_{1\mathrm{s}}} s_{i_1,N_{2\mathrm{s}}}^2 + \frac{1}{2}\sum_{i_2=1}^{N_{2\mathrm{s}}} s_{N_{1\mathrm{s}},i_2}^2. \end{aligned} \tag{A.3}$$

The first two terms measure the second derivatives (curvature) in the x and y directions of the pixels. The remaining terms are added to enforce our a priori preference toward a blank

image with nonsingular Hessian (important for the model ranking) that gives $\boldsymbol{s}_{\rm reg} = \mathbf{0}$. In essence, the majority of the source pixels have curvature regularization, but two sides of the bordering pixels that do not have neighboring pixels for the construction of curvature terms have gradient and zeroth-order terms instead.

It is not difficult to verify that all three forms of regularization have $\boldsymbol{s}_{\rm reg} = \mathbf{0}$ in the expansion in equation (3.12). Therefore, equation (3.13) for the most probable solution is applicable, as asserted in section 4.1.

None of the three forms of regularization impose the source intensity to be positive. In fact, equations (A.1) to (A.3) suggest that the source intensities are equally likely to be positive or negative based on only the prior.

In principle, one can continue the process and construct regularizations of higher derivatives. For example, the next order of derivative after curvature is jerk, and a form for the jerk form of regularization is

$$\begin{aligned} E_{\rm S}(\boldsymbol{s}) \;=\; & \frac{1}{2}\sum_{i_1=1}^{N_{1\rm s}-3}\sum_{i_2=1}^{N_{2\rm s}}\left[s_{i_1,i_2} - 3s_{i_1+1,i_2} + 3s_{i_1+2,i_2} - s_{i_1+3,i_2}\right]^2 \\ & + \frac{1}{2}\sum_{i_1=1}^{N_{1\rm s}}\sum_{i_2=1}^{N_{2\rm s}-3}\left[s_{i_1,i_2} - 3s_{i_1,i_2+1} + 3s_{i_1,i_2+2} - s_{i_1,i_2+3}\right]^2 \\ & + \frac{1}{2}\sum_{i_1=1}^{N_{1\rm s}}\left[s_{i_1,N_{2\rm s}-2} - 2s_{i_1,N_{2\rm s}-1} + s_{i_1,N_{2\rm s}}\right]^2 \\ & + \frac{1}{2}\sum_{i_2=1}^{N_{2\rm s}}\left[s_{N_{1\rm s}-2,i_2} - 2s_{N_{1\rm s}-1,i_2} + s_{N_{1\rm s},i_2}\right]^2 \\ & + \frac{1}{2}\sum_{i_1=1}^{N_{1\rm s}}\left[s_{i_1,N_{2\rm s}-1} - s_{i_1,N_{2\rm s}}\right]^2 \\ & + \frac{1}{2}\sum_{i_2=1}^{N_{2\rm s}}\left[s_{N_{1\rm s}-1,i_2} - s_{N_{1\rm s},i_2}\right]^2 \\ & + \frac{1}{2}\sum_{i_1=1}^{N_{1\rm s}} s_{i_1,N_{2\rm s}}^2 + \frac{1}{2}\sum_{i_2=1}^{N_{2\rm s}} s_{N_{1\rm s},i_2}^2. \end{aligned} \tag{A.4}$$

This form of regularization is not used for source intensity reconstruction, but is generalized (see chapter 7) for potential corrections. Regularizations with higher derivatives usually imply smoother source reconstructions, as the correlations introduced by the gradient operator extend over larger distances. Depending on the nature of the source, regularizations

of higher derivatives may not necessarily be preferred over those of lower derivatives: astronomical sources tend to be fairly compact. Therefore, we restrict ourselves to the three lowest derivative forms of the regularization for the source inversion problem.

Appendix B

Explanation of the Source Covariance Matrix in Bayesian Analysis

Notation

Expressed in terms of matrix and vector multiplications, recall equation (3.1) for the image intensity vector is

$$\boldsymbol{d} = \mathbf{f}\boldsymbol{s} + \boldsymbol{n}, \tag{B.1}$$

where $\mathbf{f}$ is the lensing (response) matrix, $\boldsymbol{s}$ is the source intensity vector and $\boldsymbol{n}$ is the noise vector. Recall equation (3.3) is

$$E_{\mathrm{D}}(\boldsymbol{s}) = \frac{1}{2}(\mathbf{f}\boldsymbol{s} - \boldsymbol{d})^{\mathrm{T}}\mathbf{C}_{\mathrm{D}}^{-1}(\mathbf{f}\boldsymbol{s} - \boldsymbol{d}), \tag{B.2}$$

where $\mathbf{C}_{\mathrm{D}} = \langle \boldsymbol{n}\boldsymbol{n}^{\mathrm{T}} \rangle$ is the image noise covariance matrix. We write the prior exponent as

$$\lambda E_{\mathrm{S}}(\boldsymbol{s}) = \frac{1}{2}\boldsymbol{s}^{\mathrm{T}}\mathbf{S}^{-1}\boldsymbol{s}, \tag{B.3}$$

where, for simplicity, we have set $\boldsymbol{s}_{\mathrm{reg}} = \mathbf{0}$ and $E_{\mathrm{S}}(\mathbf{0}) = 0$ (valid for the regularization schemes considered in appendix A), and $\mathbf{S} = \langle \boldsymbol{s}\boldsymbol{s}^{\mathrm{T}} \rangle$ is the a priori source covariance matrix. Comparing to equation (3.12), $\mathbf{S} = (\lambda\mathbf{C})^{-1}$. Combining equations (B.2) and (B.3), the

exponent of the posterior is

$$\begin{aligned} M(\boldsymbol{s}) &= E_{\rm D}(\boldsymbol{s}) + \lambda E_{\rm S}(\boldsymbol{s}) \\ &= \frac{1}{2}(\mathbf{f}\boldsymbol{s} - \boldsymbol{d})^{\rm T}\mathbf{C}_{\rm D}^{-1}(\mathbf{f}\boldsymbol{s} - \boldsymbol{d}) + \frac{1}{2}\boldsymbol{s}^{\rm T}\mathbf{S}^{-1}\boldsymbol{s}. \end{aligned} \tag{B.4}$$

Most Likely Estimate

The most likely estimate, $\boldsymbol{s}_{\rm ML}$, is given by $\nabla E_{\rm D}(\boldsymbol{s}_{\rm ML}) = \mathbf{0}$, which gives

$$\mathbf{f}^{\rm T}\mathbf{C}_{\rm D}^{-1}(\mathbf{f}\boldsymbol{s}_{\rm ML} - \boldsymbol{d}) = \mathbf{0}. \tag{B.5}$$

Rearranging the previous equation, we obtain

$$\boldsymbol{s}_{\rm ML} = (\mathbf{f}^{\rm T}\mathbf{C}_{\rm D}^{-1}\mathbf{f})^{-1}\mathbf{f}^{\rm T}\mathbf{C}_{\rm D}^{-1}\boldsymbol{d}. \tag{B.6}$$

Differentiating $E_{\rm D}(\boldsymbol{s})$ again gives the Hessian

$$\mathbf{B} \equiv \nabla\nabla E_{\rm D}(\boldsymbol{s}) = \mathbf{f}^{\rm T}\mathbf{C}_{\rm D}^{-1}\mathbf{f}. \tag{B.7}$$

This in turn allows us to write

$$\boldsymbol{s}_{\rm ML} = \mathbf{B}^{-1}\mathbf{f}^{\rm T}\mathbf{C}_{\rm D}^{-1}\boldsymbol{d}, \tag{B.8}$$

which is equation (3.8).

By construction, $\mathbf{C}_{\rm D}$, $\mathbf{S}$, and $\mathbf{B}$ are symmetric matrices.

Error on Most Likely Estimate

Let us assume that the true source intensity is $\boldsymbol{s}_*$ (i.e., the actual true source intensity for the particular image we are considering). Now consider the expectation value of $\boldsymbol{s}_{\rm ML}$ over realizations of the noise $\boldsymbol{n}$:

$$\langle \boldsymbol{s}_{\rm ML} \rangle = \mathbf{B}^{-1}\mathbf{f}^{\rm T}\mathbf{C}_{\rm D}^{-1}\langle \mathbf{f}\boldsymbol{s}_* + \boldsymbol{n} \rangle = \mathbf{B}^{-1}\mathbf{f}^{\rm T}\mathbf{C}_{\rm D}^{-1}\mathbf{f}\boldsymbol{s}_* = \boldsymbol{s}_*, \tag{B.9}$$

where we have used $\langle \boldsymbol{n} \rangle = \mathbf{0}$ and angle brackets denote averages over noise realizations. Thus, we see that $\boldsymbol{s}_{\rm ML}$ is an *unbiased* estimator of $\boldsymbol{s}_*$.

Now consider the covariance of $\boldsymbol{s}_{\rm ML}$. Since $\langle \boldsymbol{s}_{\rm ML} \rangle = \boldsymbol{s}_*$, the covariance is given by

$$\begin{aligned} \langle (\boldsymbol{s}_{\rm ML} - \boldsymbol{s}_*)(\boldsymbol{s}_{\rm ML} - \boldsymbol{s}_*)^{\rm T} \rangle &= \langle \boldsymbol{s}_{\rm ML} \boldsymbol{s}_{\rm ML}^{\rm T} \rangle + \boldsymbol{s}_* \boldsymbol{s}_*^{\rm T} \\ &\quad - \boldsymbol{s}_* \langle \boldsymbol{s}_{\rm ML}^{\rm T} \rangle - \langle \boldsymbol{s}_{\rm ML} \rangle \boldsymbol{s}_*^{\rm T} \\ &= \langle \boldsymbol{s}_{\rm ML} \boldsymbol{s}_{\rm ML}^{\rm T} \rangle - \mathbf{S}_*, \end{aligned} \tag{B.10}$$

where $\mathbf{S}_* = \boldsymbol{s}_* \boldsymbol{s}_*^{\rm T}$ is the covariance matrix of the true signal and, once again, angle brackets denote averages over noise realizations. The term $\langle \boldsymbol{s}_{\rm ML} \boldsymbol{s}_{\rm ML}^{\rm T} \rangle$ above is given by

$$\begin{aligned} \langle \boldsymbol{s}_{\rm ML} \boldsymbol{s}_{\rm ML}^{\rm T} \rangle &= \mathbf{B}^{-1} \mathbf{f}^{\rm T} \mathbf{C}_{\rm D}^{-1} \langle \boldsymbol{d}\boldsymbol{d}^{\rm T} \rangle \mathbf{C}_{\rm D}^{-1} \mathbf{f} \mathbf{B}^{-1} \\ &= \mathbf{B}^{-1} \mathbf{f}^{\rm T} \mathbf{C}_{\rm D}^{-1} \langle (\mathbf{f}\boldsymbol{s}_* + \boldsymbol{n})(\mathbf{f}\boldsymbol{s}_* + \boldsymbol{n})^{\rm T} \rangle \mathbf{C}_{\rm D}^{-1} \mathbf{f} \mathbf{B}^{-1} \\ &= \mathbf{B}^{-1} \mathbf{f}^{\rm T} \mathbf{C}_{\rm D}^{-1} (\mathbf{f} \boldsymbol{s}_* \boldsymbol{s}_*^{\rm T} \mathbf{f}^{\rm T} + \mathbf{C}_{\rm D}) \mathbf{C}_{\rm D}^{-1} \mathbf{f} \mathbf{B}^{-1} \\ &= \mathbf{B}^{-1} \mathbf{B} \mathbf{S}_* \mathbf{B} \mathbf{B}^{-1} + \mathbf{B}^{-1} \mathbf{B} \mathbf{B}^{-1} \\ &= \mathbf{S}_* + \mathbf{B}^{-1}. \end{aligned} \tag{B.11}$$

Inserting equation (B.11) in (B.10), the covariance of $\boldsymbol{s}_{\rm ML}$ is given simply by

$$\langle (\boldsymbol{s}_{\rm ML} - \boldsymbol{s}_*)(\boldsymbol{s}_{\rm ML} - \boldsymbol{s}_*)^{\rm T} \rangle = \mathbf{B}^{-1}, \tag{B.12}$$

which agrees with equation (4.1) since $\mathbf{A} = \mathbf{B}$ for the most likely solution (with $\lambda = 0$).

Most Probable Estimate

The most probable estimate, $\boldsymbol{s}_{\rm MP}$, is given by $\nabla M(\boldsymbol{s}_{\rm MP}) = \mathbf{0}$, which gives

$$\mathbf{f}^{\rm T} \mathbf{C}_{\rm D}^{-1} (\mathbf{f} \boldsymbol{s}_{\rm MP} - \boldsymbol{d}) + \mathbf{S}^{-1} \boldsymbol{s}_{\rm MP} = \mathbf{0}. \tag{B.13}$$

Rearranging, we get

$$\boldsymbol{s}_{\rm MP} = (\mathbf{S}^{-1} + \mathbf{f}^{\rm T} \mathbf{C}_{\rm D}^{-1} \mathbf{f})^{-1} \mathbf{f}^{\rm T} \mathbf{C}_{\rm D}^{-1} \boldsymbol{d}. \tag{B.14}$$

Differentiating $M(\boldsymbol{s})$ again gives the Hessian

$$\mathbf{A} \equiv \nabla\nabla M(\boldsymbol{s}) = \mathbf{S}^{-1} + \mathbf{f}^{\mathrm{T}}\mathbf{C}_{\mathrm{D}}^{-1}\mathbf{f} = \mathbf{S}^{-1} + \mathbf{B}, \tag{B.15}$$

which, in turn, allows us to write

$$\boldsymbol{s}_{\mathrm{MP}} = \mathbf{A}^{-1}\mathbf{f}^{\mathrm{T}}\mathbf{C}_{\mathrm{D}}^{-1}\boldsymbol{d} = \mathbf{A}^{-1}\mathbf{B}\mathbf{B}^{-1}\mathbf{f}^{\mathrm{T}}\mathbf{C}_{\mathrm{D}}^{-1}\boldsymbol{d} = \mathbf{A}^{-1}\mathbf{B}\boldsymbol{s}_{\mathrm{ML}}, \tag{B.16}$$

which agrees with equation (3.13).

The Hessian A is symmetric by construction.

Error on Most Probable Estimate

Let us again assume that the true source intensity is $\boldsymbol{s}_*$. Using equations (B.16) and (B.9), the expectation value of $\boldsymbol{s}_{\mathrm{MP}}$ over realizations of the noise $\boldsymbol{n}$ is

$$\langle \boldsymbol{s}_{\mathrm{MP}} \rangle = \mathbf{A}^{-1}\mathbf{B}\langle \boldsymbol{s}_{\mathrm{ML}} \rangle = \mathbf{A}^{-1}\mathbf{B}\boldsymbol{s}_*, \tag{B.17}$$

where angle brackets denote averages over noise realizations. Thus, we see that $\boldsymbol{s}_{\mathrm{MP}}$ is a *biased* estimator (in general) of $\boldsymbol{s}_*$. We must therefore be careful when considering errors.

First consider the covariance of $\boldsymbol{s}_{\mathrm{MP}}$, which is given by

$$\langle (\boldsymbol{s}_{\mathrm{MP}} - \langle \boldsymbol{s}_{\mathrm{MP}} \rangle)(\boldsymbol{s}_{\mathrm{MP}} - \langle \boldsymbol{s}_{\mathrm{MP}} \rangle)^{\mathrm{T}} \rangle \;\; = \;\; \mathbf{A}^{-1}\mathbf{B}\mathbf{A}^{-1}, \tag{B.18}$$

where we have used equations (B.16), (B.17) and (B.11). Remembering that $\mathbf{A} = \mathbf{S}^{-1} + \mathbf{B}$, we have $\mathbf{B} = \mathbf{A} - \mathbf{S}^{-1}$, so the final result is

$$\langle (\boldsymbol{s}_{\mathrm{MP}} - \langle \boldsymbol{s}_{\mathrm{MP}} \rangle)(\boldsymbol{s}_{\mathrm{MP}} - \langle \boldsymbol{s}_{\mathrm{MP}} \rangle)^{\mathrm{T}} \rangle = \mathbf{A}^{-1} - \mathbf{A}^{-1}\mathbf{S}^{-1}\mathbf{A}^{-1}, \tag{B.19}$$

which is equivalent to equation (17) in Warren & Dye (2003).

We verified equation (B.19) by a Monte Carlo simulation of 1000 noise realizations of the source brightness distribution described in section 4.2.1. The noise realizations differ only in the values of the random seed used to generate random noise in the simulated data. We used curvature regularization (see appendix A) with a fixed (and nearly optimal) value of

the regularization constant λ for each of the 1000 source inversions. The standard deviation of $\boldsymbol{s}_{\rm MP}$ calculated from the 1000 inverted source distributions agrees with the 1-σ error from equation (B.19).

Equation (B.19) gives the error from the *reconstructed source* $\boldsymbol{s}_{\rm MP}$. Since $\boldsymbol{s}_{\rm MP}$ is a biased estimator of $\boldsymbol{s}_*$, what we really want to know is not the covariance above, but the quantity $\langle(\boldsymbol{s}_{\rm MP}-\boldsymbol{s}_*)(\boldsymbol{s}_{\rm MP}-\boldsymbol{s}_*)^{\rm T}\rangle$, which gives us the distribution of errors from the *true source*. This is given by

$$\begin{aligned}\langle(\boldsymbol{s}_{\rm MP}-\boldsymbol{s}_*)(\boldsymbol{s}_{\rm MP}-\boldsymbol{s}_*)^{\rm T}\rangle &= \mathbf{A}^{-1}\mathbf{B}\mathbf{S}_*\mathbf{B}\mathbf{A}^{-1}+\mathbf{A}^{-1}\mathbf{B}\mathbf{A}^{-1}\\ &\quad +\mathbf{S}_*-\mathbf{S}_*\mathbf{B}\mathbf{A}^{-1}\\ &\quad -\mathbf{A}^{-1}\mathbf{B}\mathbf{S}_*, \end{aligned} \tag{B.20}$$

where we have again used equations (B.16), (B.17) and (B.11). Substituting $\mathbf{B}=\mathbf{A}-\mathbf{S}^{-1}$ gives, after simplifying,

$$\begin{aligned}\langle(\boldsymbol{s}_{\rm MP}-\boldsymbol{s}_*)(\boldsymbol{s}_{\rm MP}-\boldsymbol{s}_*)^{\rm T}\rangle &= \mathbf{A}^{-1}+\mathbf{A}^{-1}\mathbf{S}^{-1}\\ &\quad (\mathbf{S}_*\mathbf{S}^{-1}-\mathbf{I})\mathbf{A}^{-1}. \end{aligned} \tag{B.21}$$

In reality, we do not know $\mathbf{S}_*$ (as this would require knowing the true source intensity $\boldsymbol{s}_*$). However, by averaging over source brightness distributions (denoted by a bar), we have $\overline{\mathbf{S}_*}=\mathbf{S}$. This is the manifestation of our explicit assumption that all source intensity distributions are drawn from the prior probability density defined by equation (3.4). Thus,

$$\overline{\langle(\boldsymbol{s}_{\rm MP}-\boldsymbol{s}_*)(\boldsymbol{s}_{\rm MP}-\boldsymbol{s}_*)^{\rm T}\rangle}=\mathbf{A}^{-1}, \tag{B.22}$$

which is the inverse of $\nabla\nabla M(\boldsymbol{s})$. In words, the covariance matrix describing the uncertainties in the inverted source intensity is given by the width of the approximated Gaussian posterior in equation (3.7), which is $\mathbf{A}^{-1}$. The covariance matrix of $\boldsymbol{s}_{\rm MP}$ in equation (B.19) in general underestimates the error relative to the true source image because it does not incorporate the bias in the reconstructed source.

Appendix C

The Matrix Operator in Potential Reconstruction

A comparison of the potential correction equation (7.4) to its matrix form in equation (7.10) shows that the matrix operator $\mathbf{t}$ needs to include the PSF blurring, the reconstructed source intensity gradient, and the gradient operator that acts on the potential perturbations $\boldsymbol{\delta\psi}$. We will consider each of these in the reverse order.

Before discussing the gradient operator, we need to define the region in which the gradient operator acts. Recall the potential corrections are obtained on an annular region that encloses the Einstein ring of the lensed source. This annular region was obtained by tracing all the potential pixels back to the source plane (via the lens equation (2.3)) and seeing which ones land on the finite source region of reconstruction. Only these potential pixels that trace back to the finite source region will have values of the source intensity gradient for potential correction via equation (7.4). These pixels tend to mark an annular region. We therefore need to find the gradient operator on this annular region for $\delta\psi$.

To construct the gradient operator, we use finite differencing to obtain numerical derivatives. For simplicity, first consider a $M \times N$ rectangular grid with x_1 and x_2 as axes and (i, j) as pixel indices. In this case, the partial derivatives of a function $f_{i,j}$ defined on the

grid are:

$$\begin{aligned}
\frac{\partial f_{i,j}}{\partial x_1} &= \begin{cases} \frac{1}{2\Delta x_1}(-3f_{1,j} + 4f_{2,j} - f_{3,j}) & \text{if } i = 1, \\ \frac{1}{2\Delta x_1}(f_{i+1,j} - f_{i-1,j}) & \text{if } i = 2, \ldots, M-1, \\ \frac{1}{2\Delta x_1}(f_{M-2,j} - 4f_{M-1,j} + 3f_{M,j}) & \text{if } i = M, \end{cases} \\
\frac{\partial f_{i,j}}{\partial x_2} &= \begin{cases} \frac{1}{2\Delta x_2}(-3f_{i,1} + 4f_{i,2} - f_{i,3}) & \text{if } j = 1, \\ \frac{1}{2\Delta x_2}(f_{i,j+1} - f_{i,j-1}) & \text{if } j = 2, \ldots, N-1, \\ \frac{1}{2\Delta x_2}(f_{i,N-2} - 4f_{i,N-1} + 3f_{i,N}) & \text{if } j = N, \end{cases}
\end{aligned} \tag{C.1}$$

where Δx_1 and Δx_2 are the pixel sizes in x_1 and x_2 directions. For the annular region of potential corrections, we only need to elaborate slightly on equation (C.1). The edge pixels of the annulus are treated as though they are like the edge pixels of the rectangular grid (so that the $i = 1$, $i = M$, $j = 1$ or $j = N$ expressions are used) when the edge pixels are adjacent to at least two other pixels in the annulus in the direction of which the numerical derivative is taken. If an edge pixel of the annulus is only adjacent to one other pixel in the direction of which the numerical derivative is taken, then we construct the gradient by taking the difference between the two and dividing by the pixel size. For example, if $f_{i,j}$ is at the edge, and only $f_{i+1,j}$ is also in the annulus (which will have to be an edge pixel if $f_{i+2,j}$ is not in the annulus), then the numerical derivatives in the x_1 direction for both $f_{i,j}$ and $f_{i+1,j}$ are

$$\frac{\partial f_{i,j}}{\partial x_1} = \frac{f_{i+1,j} - f_{i,j}}{\Delta x_1}. \tag{C.2}$$

Similar equation applies to the x_2 direction. If an edge pixel in the annulus is "exposed" in the sense that in one of the directions x_1 or x_2, it has no adjacent pixels in the annulus, then this pixel is removed from the annular region of reconstruction as no numerical derivative can be formed. Following the above prescription, we can obtain the values $(\frac{\partial f_{i,j}}{\partial x_1}, \frac{\partial f_{i,j}}{\partial x_2})$ of all the (i, j) pixels in the annulus in terms values of the function in the annulus f_{kl}. Factoring out the f_{kl} values, we obtain the gradient operator defined as two matrices: $\mathbf{D}_1$ for $\frac{\partial}{\partial x_1}$ and $\mathbf{D}_2$ for $\frac{\partial}{\partial x_2}$.

To conform to the data grid (since the intensity deficit and image covariance matrix is defined on the data grid), we use bilinear interpolation. We overlay the data grid on the coarser grid, and for every data pixel that lies inside the annular region on the coarse grid, we bilinear interpolate to get, effectively, gradient operators on the data grid. This gives us an

$N_{\rm d} \times N_{\rm p}$ matrix $\mathbf{G}$ where each row (corresponding to a data pixel that lies within the annulus) has four non-zero values that correspond to the coefficients of bilinearly interpolating among the four coarse potential pixels surrounding this data pixel. Associated with each data pixel are the source intensity gradient values ($\frac{\partial I}{\partial \beta_1}$ and $\frac{\partial I}{\partial \beta_2}$) that were obtained by mapping the data pixel back to the source plane using the lens equation, and interpolate on the reconstructed source intensity gradient on the source grid. We define matrices $\mathbf{G}_1$ and $\mathbf{G}_2$ as the matrix $\mathbf{G}$ weighted by the source intensity gradient components $\frac{\partial I}{\partial \beta_1}$ and $\frac{\partial I}{\partial \beta_2}$, respectively. By definition, $\mathbf{G}_1$ and $\mathbf{G}_2$ and also $N_{\rm d} \times N_{\rm p}$.

Lastly, we represent the PSF as a blurring matrix (operator) $\mathbf{B}$ that is of dimensions $N_{\rm d} \times N_{\rm d}$ (see, e.g., chapter 6 and section 4.1; Treu & Koopmans (2004)). Note that this matrix $\mathbf{B}$ is different from the matrix in chapter 3 that is the Hessian of the $E_{\rm D}$.

Combining all the pieces together, the matrix operator $\mathbf{t}$ is

$$\mathbf{t} = \mathbf{B} \cdot \mathbf{G}_1 \cdot \mathbf{D}_1 + \mathbf{B} \cdot \mathbf{G}_2 \cdot \mathbf{D}_2, \tag{C.3}$$

which is of dimensions $N_{\rm d} \times N_{\rm p}$.

For the gravitational lens system B1608+656, we need to also include the effects of dust extinction, which we express as a diagonal matrix $\mathbf{K}$. Tracing back along the light rays, we encounter the dust immediately after the PSF blurring (for the light from the lensed source). Therefore we include it in equation (C.3) after $\mathbf{B}$ to get the following expression for matrix operator $\mathbf{t}$ that includes dust:

$$\mathbf{t} = \mathbf{B} \cdot \mathbf{K} \cdot \mathbf{G}_1 \cdot \mathbf{D}_1 + \mathbf{B} \cdot \mathbf{K} \cdot \mathbf{G}_2 \cdot \mathbf{D}_2. \tag{C.4}$$

Bibliography

Barnabè M., Koopmans L. V. E., 2007, ArXiv Astrophysics e-prints

Behr A., 1951, Astronomische Nachrichten, 279, 97

Birkinshaw M., 1999, Phys.Rep., 310, 97

Blandford R., Narayan R., 1986, ApJ, 310, 568

Blandford R., Surpi G., Kundić T., 2001, in ASP Conf. Ser. 237: Gravitational Lensing: Recent Progress and Future Goals, Brainerd T. G., Kochanek C. S., eds., San Francisco: Astron. Soc. Pac., p. 65

Blandford R. D., McKee C. F., 1982, ApJ, 255, 419

Bolton J. S., Haehnelt M. G., Viel M., Carswell R. F., 2006, MNRAS, 366, 1378

Bolton J. S., Haehnelt M. G., Viel M., Springel V., 2005, MNRAS, 357, 1178

Bonamente M., Joy M. K., LaRoque S. J., Carlstrom J. E., Reese E. D., Dawson K. S., 2006, ApJ, 647, 25

Bottinelli L., Gouguenheim L., Paturel G., Teerikorpi P., 1991, A&A, 252, 550

Bradač M., Schneider P., Lombardi M., Steinmetz M., Koopmans L. V. E., Navarro J. F., 2004, A&A, 423, 797

Bradač M., Schneider P., Steinmetz M., Lombardi M., King L. J., Porcas R., 2002, A&A, 388, 373

Brewer B. J., Lewis G. F., 2006, ApJ, 637, 608

Bridle S. L., Hobson M. P., Lasenby A. N., Saunders R., 1998, MNRAS, 299, 895

Cardelli J. A., Clayton G. C., Mathis J. S., 1989, ApJ, 345, 245

Casertano S., de Mello D., Dickinson M., Ferguson H. C., Fruchter A. S., Gonzalez-Lopezlira R. A., Heyer I., Hook R. N., Levay Z., Lucas R. A., Mack J., Makidon R. B., Mutchler M., Smith T. E., Stiavelli M., Wiggs M. S., Williams R. E., 2000, AJ, 120, 2747

Ciardullo R., Feldmeier J. J., Jacoby G. H., Kuzio de Naray R., Laychak M. B., Durrell P. R., 2002, ApJ, 577, 31

Da Costa G. S., Armandroff T. E., 1990, AJ, 100, 162

Dai X., Kochanek C. S., 2005, ApJ, 625, 633

Dale D. A., Giovanelli R., Haynes M. P., Campusano L. E., Hardy E., 1999, AJ, 118, 1489

Djorgovski S., Davis M., 1987, ApJ, 313, 59

Dobler G., Keeton C. R., Wambsganss J., 2007, MNRAS, 377, 977

Dodelson S., 2003, Modern Cosmology. Academic Press

Dressler A., Gunn J. E., 1983, ApJ, 270, 7

Dressler A., Lynden-Bell D., Burstein D., Davies R. L., Faber S. M., Terlevich R., Wegner G., 1987, ApJ, 313, 42

Dye S., Smail I., Swinbank A. M., Ebeling H., Edge A. C., 2007, ArXiv e-prints, 705

Dye S., Warren S. J., 2005, ApJ, 623, 31

Eisenstein D. J., Zehavi I., Hogg D. W., Scoccimarro R., Blanton M. R., Nichol R. C., Scranton R., Seo H.-J., Tegmark M., Zheng Z., Anderson S. F., Annis J., Bahcall N., Brinkmann J., Burles S., Castander F. J., Connolly A., Csabai I., Doi M., Fukugita M., Frieman J. A., Glazebrook K., Gunn J. E., Hendry J. S., Hennessy G., Ivezić Z., Kent S., Knapp G. R., Lin H., Loh Y.-S., Lupton R. H., Margon B., McKay T. A., Meiksin A., Munn J. A., Pope A., Richmond M. W., Schlegel D., Schneider D. P., Shimasaku K., Stoughton C., Strauss M. A., SubbaRao M., Szalay A. S., Szapudi I., Tucker D. L., Yanny B., York D. G., 2005, ApJ, 633, 560

Faber S. M., Jackson R. E., 1976, ApJ, 204, 668

Fassnacht C. D., Gal R. R., Lubin L. M., McKean J. P., Squires G. K., Readhead A. C. S., 2006, ApJ, 642, 30

Fassnacht C. D., Pearson T. J., Readhead A. C. S., Browne I. W. A., Koopmans L. V. E., Myers S. T., Wilkinson P. N., 1999, ApJ, 527, 498

Fassnacht C. D., Womble D. S., Neugebauer G., Browne I. W. A., Readhead A. C. S., Matthews K., Pearson T. J., 1996, ApJ, 460, L103+

Fassnacht C. D., Xanthopoulos E., Koopmans L. V. E., Rusin D., 2002, ApJ, 581, 823

Federspiel M., 1999, PhD thesis, Univ. of Basel

Ford H. C., Jenner D. C., 1978, in Bulletin of the American Astronomical Society, Vol. 10, Bulletin of the American Astronomical Society, pp. 665–+

Freedman W. L., Madore B. F., Gibson B. K., Ferrarese L., Kelson D. D., Sakai S., Mould J. R., Kennicutt Jr. R. C., Ford H. C., Graham J. A., Huchra J. P., Hughes S. M. G., Illingworth G. D., Macri L. M., Stetson P. B., 2001, ApJ, 553, 47

Freedman W. L., Turner M. S., 2003, Reviews of Modern Physics, 75, 1433

Fruchter A., Hook R. N., 1997, in Presented at the Society of Photo-Optical Instrumentation Engineers (SPIE) Conference, Vol. 3164, Proc. SPIE Vol. 3164, p. 120-125, Applications of Digital Image Processing XX, Andrew G. Tescher; Ed., Tescher A. G., ed., pp. 120–125

Giovanelli R., Haynes M. P., Herter T., Vogt N. P., Wegner G., Salzer J. J., da Costa L. N., Freudling W., 1997, AJ, 113, 22

Grogin N. A., Narayan R., 1996a, ApJ, 464, 92

—, 1996b, ApJ, 473, 570

Gull S. F., Daniell G. J., 1978, Nature, 272, 686

Herrnstein J. R., Moran J. M., Greenhill L. J., Diamond P. J., Inoue M., Nakai N., Miyoshi M., Henkel C., Riess A., 1999, Nature, 400, 539

Hobson M. P., Bridle S. L., Lahav O., 2002, MNRAS, 335, 377

Hollis J. M., Dorband J. E., Yusef-Zadeh F., 1992, ApJ, 386, 293

Holmberg E., 1958, Meddelanden fran Lunds Astronomiska Observatorium Serie II, 136, 1

Hu W., 2005, in Astronomical Society of the Pacific Conference Series, Vol. 339, Observing Dark Energy, Wolff S. C., Lauer T. R., eds., pp. 215–+

Hubble E., 1929, Proceedings of the National Academy of Science, 15, 168

Jorgensen I., Franx M., Kjaergaard P., 1996, MNRAS, 280, 167

Karachentsev I. D., Makarov D. I., Sharina M. E., Dolphin A. E., Grebel E. K., Geisler D., Guhathakurta P., Hodge P. W., Karachentseva V. E., Sarajedini A., Seitzer P., 2003, A&A, 398, 479

Kavelaars J. J., Harris W. E., Hanes D. A., Hesser J. E., Pritchet C. J., 2000, ApJ, 533, 125

Keeton C. R., Zabludoff A. I., 2004, ApJ, 612, 660

Kochanek C., Schneider P., Wambsganss J., 2006, Gravitational Lensing: Strong, Weak and Micro. Springer

Koekemoer A. M., Fruchter A. S., Hook R. N., Hack W., 2002, in The 2002 HST Calibration Workshop : Hubble after the Installation of the ACS and the NICMOS Cooling System, Proceedings of a Workshop held at the Space Telescope Science Institute, Baltimore, Maryland, October 17 and 18, 2002. Edited by Santiago Arribas, Anton Koekemoer, and Brad Whitmore. Baltimore, MD: Space Telescope Science Institute, 2002., p.337, Arribas S., Koekemoer A., Whitmore B., eds., pp. 337–+

Koopmans L. V. E., 2005, MNRAS, 363, 1136

Koopmans L. V. E., Biggs A., Blandford R. D., Browne I. W. A., Jackson N. J., Mao S., Wilkinson P. N., de Bruyn A. G., Wambsganss J., 2003a, ApJ, 595, 712

Koopmans L. V. E., de Bruyn A. G., 2000, A&A, 358, 793

Koopmans L. V. E., Fassnacht C. D., 1999, ApJ, 527, 513

Koopmans L. V. E., Treu T., 2002, ApJ, 568, L5

Koopmans L. V. E., Treu T., Fassnacht C. D., Blandford R. D., Surpi G., 2003b, ApJ, 599, 70

Kormann R., Schneider P., Bartelmann M., 1994, A&A, 284, 285

Krist J. E., Hook R. N., 1997, in The 1997 HST Calibration Workshop with a New Generation of Instruments, p. 192, Casertano S., Jedrzejewski R., Keyes T., Stevens M., eds., pp. 192–+

Limousin M., Richard J., Jullo E., Kneib J. ., Fort B., Soucail G., Elíasdóttir A., Natarajan P., Ellis R. S., Smail I., Czoske O., Smith G. P., Hudelot P., Bardeau S., Ebeling H., Egami E., Knudsen K. K., 2006, ArXiv Astrophysics e-prints

Lo K. Y., 2005, ARA&A, 43, 625

MacKay D. J. C., 1992, Neural Computation, 4, 415

Macri L. M., Stanek K. Z., Bersier D., Greenhill L. J., Reid M. J., 2006, ApJ, 652, 1133

Mao S., Schneider P., 1998, MNRAS, 295, 587

Marshall P., 2006, MNRAS, 372, 1289

Marshall P. J., Hobson M. P., Gull S. F., Bridle S. L., 2002, MNRAS, 335, 1037

Mendez R. H., Kudritzki R. P., Ciardullo R., Jacoby G. H., 1993, A&A, 275, 534

Metcalf R. B., Madau P., 2001, ApJ, 563, 9

Minkowski R., 1962, in IAU Symposium, Vol. 15, Problems of Extra-Galactic Research, McVittie G. C., ed., pp. 112–+

Morgan C. W., Kochanek C. S., Morgan N. D., Falco E. E., 2006, ApJ, 647, 874

Myers S. T., Fassnacht C. D., Djorgovski S. G., Blandford R. D., Matthews K., Neugebauer G., Pearson T. J., Readhead A. C. S., Smith J. D., Thompson D. J., Womble D. S., Browne I. W. A., Wilkinson P. N., Nair S., Jackson N., Snellen I. A. G., Miley G. K., de Bruyn A. G., Schilizzi R. T., 1995, ApJ, 447, L5+

Oguri M., 2007, ApJ, 660, 1

Oke J. B., Cohen J. G., Carr M., Cromer J., Dingizian A., Harris F. H., Labrecque S., Lucinio R., Schaal W., Epps H., Miller J., 1995, PASP, 107, 375

Pei Y. C., 1992, ApJ, 395, 130

Peng C. Y., Ho L. C., Impey C. D., Rix H.-W., 2002, AJ, 124, 266

Peterson B., 2006, in Physics of Active Galactic Nuclei at All Scales, Alloin D., Johnson R., Lira P., eds., Vol. 693, Springer Lectures Notes in Physics Series, p. 77

Press W. H., Flannery B. P., Teukolsky S. A., Vetterling W. T., 1992, Numerical Recipes in Fortran 77. Cambridge: Cambridge Univ. Press

Refsdal S., 1964, MNRAS, 128, 307

Rhodes J. D., Massey R. J., Albert J., Collins N., Ellis R. S., Heymans C., Gardner J. P., Kneib J.-P., Koekemoer A., Leauthaud A., Mellier Y., Refregier A., Taylor J. E., Van Waerbeke L., 2007, ApJS, 172, 203

Riess A. G., Li W., Stetson P. B., Filippenko A. V., Jha S., Kirshner R. P., Challis P. M., Garnavich P. M., Chornock R., 2005, ApJ, 627, 579

Saha P., Coles J., Macciò A. V., Williams L. L. R., 2006, ApJ, 650, L17

Sakai S., Ferrarese L., Kennicutt Jr. R. C., Saha A., 2004, ApJ, 608, 42

Sambhus N., Gerhard O., Méndez R. H., 2006, AJ, 131, 837

Sandage A., 1962, in IAU Symposium, Vol. 15, Problems of Extra-Galactic Research, McVittie G. C., ed., pp. 359–+

—, 1999, ApJ, 527, 479

Sandage A., Hardy E., 1973, ApJ, 183, 743

Sandage A., Tammann G. A., 1975, ApJ, 197, 265

—, 2006, ARA&A, 44, 93

Sandage A., Tammann G. A., Reindl B., 2004, A&A, 424, 43

Sandage A., Tammann G. A., Saha A., Reindl B., Macchetto F. D., Panagia N., 2006, ApJ, 653, 843

Schechter P. L., Wambsganss J., 2002, ApJ, 580, 685

Schmidt R. W., Allen S. W., Fabian A. C., 2004, MNRAS, 352, 1413

Sérsic J. L., 1960, Zeitschrift fur Astrophysik, 50, 168

Sheinis A. I., Bolte M., Epps H. W., Kibrick R. I., Miller J. S., Radovan M. V., Bigelow B. C., Sutin B. M., 2002, PASP, 114, 851

Skilling J., 1989, Maximum Entropy and Bayesian Methods, Skilling J., ed. Dordrecht: Kluwer, p. 45

Smail I., Swinbank A. M., Richard J., Ebeling H., Kneib J.-P., Edge A. C., Stark D., Ellis R. S., Dye S., Smith G. P., Mullis C., 2007, ApJ, 654, L33

Snellen I. A. G., de Bruyn A. G., Schilizzi R. T., Miley G. K., Myers S. T., 1995, ApJ, 447, L9+

Surpi G., Blandford R. D., 2003, ApJ, 584, 100

Suyu S. H., Blandford R. D., 2006, MNRAS, 366, 39

Suyu S. H., Marshall P. J., Hobson M. P., Blandford R. D., 2006, MNRAS, 371, 983

Tammann G. A., 1993, in IAU Symposium, Vol. 155, Planetary Nebulae, Weinberger R., Acker A., eds., pp. 515–+

—, 2006, in Reviews in Modern Astronomy, Vol. 19, Reviews in Modern Astronomy, Roeser S., ed., pp. 1–+

Tammann G. A., Sandage A., 1999, in Astronomical Society of the Pacific Conference Series, Vol. 167, Harmonizing Cosmic Distance Scales in a Post-HIPPARCOS Era, Egret D., Heck A., eds., pp. 204–216

Tammann G. A., Sandage A., Reindl B., 2003, A&A, 404, 423

Tonry J. L., Franx M., 1999, ApJ, 515, 512

Treu T., Koopmans L. V. E., 2002, MNRAS, 337, L6

—, 2004, ApJ, 611, 739

Tully R. B., Fisher J. R., 1977, A&A, 54, 661

van den Bergh S., Pritchet C., Grillmair C., 1985, AJ, 90, 595

Wallington S., Kochanek C. S., Narayan R., 1996, ApJ, 465, 64

Warren S. J., Dye S., 2003, ApJ, 590, 673

Wayth R. B., Warren S. J., Lewis G. F., Hewett P. C., 2005, MNRAS, 360, 1333

Williams L. L. R., Saha P., 2000, AJ, 119, 439

Winn J. N., Rusin D., Kochanek C. S., 2004, Nature, 427, 613

Wucknitz O., 2002, MNRAS, 332, 951

York T., Jackson N., Browne I. W. A., Wucknitz O., Skelton J. E., 2005, MNRAS, 357, 124